Bruno Max de Souza Melo

Impurity solvers for the single impurity Anderson model: comparison and applications

Niterói

2019

Bruno Max de Souza Melo

Impurity solvers for the single impurity Anderson model: comparison and applications

Tese apresentada ao Curso de Pós-Graduação em Física da Universidade Federal Fluminense, como requisito parcial para obtenção do Título de Doutor em Física.

Orientador:
Prof. Dr. CAIO HENRIQUE LEWENKOPF

Universidade Federal Fluminense
Instituto de Física

Niterói

2019

Ficha catalográfica automática - SDC/BIF
Gerada com informações fornecidas pelo autor

M528i Melo, Bruno Max de Souza
Impurity solvers for the single impurity Anderson model: comparison and applications / Bruno Max de Souza Melo ; Caio Henrique Lewenkopf, orientador. Niterói, 2019.
109 f. : il.

Tese (doutorado)-Universidade Federal Fluminense, Niterói, 2019.

DOI: http://dx.doi.org/10.22409/PPGF.2019.d.11995338745

1. Modelo de Anderson. 2. Ponto quântico. 3. Efeito Kondo. 4. Modelo de Hubbard. 5. Produção intelectual. I. Lewenkopf, Caio Henrique, orientador. II. Universidade Federal Fluminense. Instituto de Física. III. Título.

CDD -

Bibliotecário responsável: Mario Henrique de Oliveira Castro - CRB7/6155

Acknowledgments

I would like to thank my advisor, Prof. Caio Lewenkopf. Caio is truly a great bible of the condensed matter and a great example for me of how to be a scientist. I would like to thank him for believe in my potential. For all the support after my decision to leave my job and become a graduate student. For introducing me to the condensed matter universe and its connection with the numerical simulations world, an extremely complex combination - complicated and challenging but irresistibly fascinating - and, for this very reason, perfectly capable of matching so much to my expectations and aspirations (the latter do not necessarily translate into having the proper background for facing such a stone wall, just to make it clear and not sound arrogant). I would like to acknowledge Caio for helping me in tough analytical derivations with his great insights and tricks in solving problems that several times seemed impossible to understand for me. I would like to thank him for his patience, kindness and comprehension with my limitations. For recognizing and praising my achievements. For his extremely valuable and useful suggestions for improving my writing style. I would like to thank him, above all, for his invaluable contribution to my development as a researcher.

I would like to express my gratitude to my colaborator in this work, professor Alexandre Reily Rocha, who is undoubtedly one of the greatest physicists of his generation and another great example of scientist with whom I had the great honor of working with. I would like to thank him for sharing his deep background on the most diverse subjects of physics and of the development universe with me. For his great help and attention given to me in times of technical difficulties. I thank him for his infinite patience with my most elementary questions, for his deep respect with my learning pace. For always trying to follow my reasoning while discussing by no means trivial subjects, always giving me the important feeling that my questions were precisely understood. For including me in his list of registered students to use the resources of the Santos Dumont supercomputer, something of fundamental importance for the development of my programming skills and for the progress of this thesis. And, finally, for always receiving me with great hospitality and kindness at his workplace at IFT-Unesp, something that certainly makes these visits one of the most memorable moments of this journey.

I would like to thank the professor Luis Gregorio Dias da Silva for providing the NRG results, for always treating me with great politeness and kindness, for the fruitful discussions and for his invaluable contribution to this thesis.

To my parents for having educated me for life.

I would like to thank my wife, Ianê Nogueira, the person who most supported me in this endeavor of leaving a comfort zone and follow my dreams. Honestly, I do not know whether I would have gotten here without her support. I would like to thank her for her infinite patience. For putting up with me during this very difficult and tense period. For always cheering me up in times of discouragement. For always telling me that everything will be all right. For making me happy. For praising me on everything I do. For being such an important part of my life, and, above all, for her infinite and unconditional love.

My deepest and most affectionate thanks to my wife's family Suzana, Werneck, Francisco, Manu, Isadora, Pedro and Tainá for welcoming me with open arms and providing me with unforgettable moments of great joy and for kindly showing interest in hearing me to speak about my research subject.

My special thanks to my group colleague Vladimir Miranda for the rich discussions about the Kondo effect, for the words of encouragement, and for kindly hearing me several times when I needed to vent.

I would like to specially acknowledge my group colleague Leandro Lima for always being available to answer my questions and for his invaluable contribution in developing my programming skills.

My special acknowledgement to my group colleague Daiara Faria for the words of encouragement, for the fruitful discussions on condensed matter and for her infinite kindness.

To the friends made during this journey for the valuable exchanges of ideas and moments of relaxation and laughter.

I would like to acknowledge the Nano-structured Systems group members of UFF for the welcome, for the rich discussions in the seminars and weekly meetings, and for the inestimable contributions to my learning of the different subjects of the condensed matter.

Finally, I would to thank CNPq for the financial support provided during my PhD.

Abstract

The single impurity Anderson model (SIAM) is one of the most recurrent model Hamiltonians in condensed matter physics, playing an important role in the description of systems where electron-electron interactions can not be neglected, such as strongly interacting quantum dots and doped metals with magnetic impurities. The numerical solution of this model also constitutes an essential step for obtaining the spectral quantities of the lattice many-body models like the Hubbard model and for obtaining a consistent theoretical description of a huge variety of strongly correlated materials, in the context of the Dynamical Mean Field Theory (DMFT) and its combination with electronic structure calculation methods like the density functional theory (DFT). The applicability of the Anderson model also extends to the very active field of molecular electronics, where a combination of DFT, DMFT and the non equilibrium Green's function formalism (NEGF) can be used in order to give a realistic description of the transport properties of molecular electronic devices taking into account the effect of strong correlations when they are present. In order to address such a variety of scenarios many impurity solvers were developed for the Anderson model. It is consensus that there is no universal method that provides reliable results for the model parameter space of experimental interest. The main methods found in the literature differs significantly on the computational cost involved in the numerical implementation and in the range of the model parameters where the used method is reliable. In this thesis we assess the reliability of some impurity solvers for the SIAM, namely, the equations of motion (EOM) method, the numerical renormalization group (NRG), the non-crossing approximation (NCA), and the one crossing approximation (OCA). First, we study the Green's function of a quantum dot using the aforementioned impurity solvers and then calculate the density of states as well as the zero bias conductance as a function of the temperature of the quantum dot in the wide band limit for a variety of scenarios . Our analysis is focused on the Coulomb blockade and the Kondo physics. We report that some standard approximations based on the EOM technique display a rather unexpected poor behaviour in the Coulomb blockade regime even at high temperatures. Next we study the Hubbard model applied to a hypercubic lattice and compute the density of states of the model using the DMFT combined with EOM, NCA, and OCA as impurity solvers paying particular attention to the physics of the Mott metal-insulator transition. By means of a contour plot we also present an evolution of the density of states as the local Coulomb interaction is increased comparing the main features of the transition displayed in each method. We discuss the applicability of each method based on our results and on the previous ones reported in the literature over the years.

Resumo

O modelo de impureza única de Anderson (SIAM) é um dos modelos mais recorrentes em física da matéria condensada, desempenhando um papel importante na descrição de sistemas onde as interações elétron-elétron não podem ser desprezadas, tais como pontos quânticos fortemente interagentes e metais dopados com impurezas magnéticas. A solução numérica deste modelo também constitui uma etapa essencial para obter as quantidades espectrais de modelos de rede de muitos corpos como o modelo de Hubbard e para obter uma descrição teórica consistente de uma enorme variedade de materiais fortemente correlacionados, no contexto da Teoria de Campo Médio Dinâmica (DMFT) e sua combinação com métodos de cálculo de estrutura eletrônica como a teoria do funcional da densidade (DFT). A aplicabilidade do modelo de Anderson se extende também ao campo muito ativo da eletrônica molecular, onde uma combinação de DFT, DMFT e o formalismo das funções de Green fora do equilíbrio (NEGF) pode ser usada para fornecer uma descrição realista das propriedades de transporte de dispositivos de eletrônica molecular levando em conta os efeitos de correlações fortes quando elas estão presentes. Para abordar tal variedade de cenários muitos métodos numéricos de solução foram desenvolvidos para o modelo de Anderson. É consenso que não existe nenhum método universal que forneça resultados confiáveis para o espaço de parâmetros do modelo de interesse experimental. Os principais métodos encontrados na literatura diferem significativamente quanto ao custo computacional envolvido na implementação numérica e na faixa de parâmetros do modelo onde o método usado é confiável. Nesta tese nós avaliamos a confiabilidade de alguns métodos numéricos de solução para o SIAM, a saber, o método das equações de movimento (EOM), o grupo de renormalização numérico (NRG), a aproximação de não cruzamento (NCA) e a aproximação de um cruzamento (OCA). Primeiro, nós estudamos função de Green de um ponto quântico usando os métodos supracitados e então calculamos a densidade de estados bem como a condutância à voltagem nula em função da temperatura do ponto quântico no limite de banda larga para uma variedade de cenários. Nossa análise é focada no regime do bloqueio de Coulomb e na física de Kondo. Nós relatamos que algumas aproximações padrão baseadas na técnica EOM exibem um comportamento pobre bastante inesperado no regime de bloqueio de Coulomb até mesmo em temperaturas altas. Em seguida, nós estudamos o modelo de Hubbard aplicado a uma rede hipercúbica e calculamos a densidade de estados do modelo usando a DMFT combinada com EOM, NCA e OCA como métodos para o problema de uma impureza prestando atenção particular à física da transição metal-isolante de Mott. Por meio de um gráfico de contornos nós também apresentamos uma evolução da densidade de estados a medida que a interação coulombiana é aumentada comparando os principais atributos da transição exibida em cada método. Nós discutimos a aplicabilidade de cada método baseada em nossos resultados e em resultados prévios relatados na literatura ao longo dos anos.

List of Figures

1 (a) Resistance as a function of the temperature of an alloy of Cu (host metal) and Fe (magnetic impurity). Note the minimum in the resistance as mentioned in the text. Note also that the value of the minimum depends on the concentration of the impurities. Extracted from Ref. [4]. (b) In a pure metal (blue line) the resistance saturates below a certain temperature (typically $10K$). In a superconductor (green line), the resistance vanishes below a critical temperature. In a metal containing magnetic impurities (red line) the resistance reaches a minimum and start increasing again. Extracted from Ref. [3]. . . . . p. 16

2 (a)Schematic energy diagram of the single impurity Anderson model. A single particle localized level with energy ε_0 is coupled to a continuum of states (indicated in the figure) representing the free electrons of the metal. In the situation depicted the impurity is occupied with one spin-up electron. Double occupancy is prohibited by the Coulomb energy U. (b) *Exchange process*: The spin-up electron may tunnel out of the impurity and occupy a conduction band state near the Fermi level leaving room for a bath electron with opposite spin to hop into the impurity site. (c) The result of this process is an effective change of the impurity spin. See discussion in the text. Adapted from Ref. [9]. . . . . p. 18

3 Single electron transistor. Metallic gates (white regions) on the surface of a semiconductor heterostructure containing a two dimensional electron gas (dark region). The upper and lower electrodes on the left and the electrode in the right are used to control the tunnel barriers between the island of electrons and the electron gas (at top and bottom). The middle terminal in the left is the gate electrode. The source and drain contacts (not shown) are at the top and bottom of the image, respectively. Extracted from Ref. [40] . . . . . p. 21

4 Zero bias conductance as function of the gate voltage for different values of temperature. The alternating pattern of peaks and valleys in the conductance is the hallmark of the Coulomb blockade. Extracted from Ref. [46]. . . . . p. 23

5 Schematic representation of the zero bias conductance of a quantum dot as a function of the gate voltage. The solid curve is for $T \ll T_K$, the dotted curve for $T \approx T_K$, and the dashed curve for $T > T_K$. For odd electron number in the dot the conductance increases as the temperature is lowered due to the Kondo effect reaching the quantum limit of conductance $2e^2/h$ for $T \ll T_K$. For even electron number in the dot the Kondo effect doesn't occur. The conductance decreases as the temperature is lowered due to a decrease of thermally excited transport through the dot. Extracted from Ref. [45]. . . . . p. 23

6 (a) Typical experimental set up encountered in molecular electronics: a magnetic organic molecule, [Co(tpy-SH)2]2+, coupled to the tips of nanocontacts. (b) The proper theoretical description of such devices need to take into account the realistic atomic and electronic structures of both the electrodes and the molecule. (c) Schematic representation of the energy diagram of the situation depicted. The molecular energy levels are broadened due to the hybridization with the electrodes. Figure 6a taken from Ref. [20]. Figure 6b extracted from Ref. [51] and Fig. 6c has been provided by Prof. Alexandre Reily Rocha (IFT-UNESP). . . p. 24

7 (a) Diagrammatic representation of the pseudoparticle self-energies. (b) Vertex corrections. The solid, wiggly, dashed, and curly lines corresponds to the pseudofermion, empty boson, conduction electron, and doubly occupied boson propagators, respectively. When the black and green vertices in (a) are replaced by the bare ones we obtain the diagrams of the non-crossing approximation. The one crossing approximation consists of including the vertices in the self-energy diagrams. Extracted from Ref. [62] p. 44

8 Density of states of the SIAM for the particle-hole symmetric case, $\varepsilon_0 = -U/2$, with $\Gamma = 0.1U$ and $T = 0.1U$ and $T/T_K \approx 1000$ obtained by different methods. . . . . p. 49

9 Density of states of the SIAM for $\varepsilon_0 = -0.26U \simeq -U/4$, with $\Gamma = 0.1U$ and $T = 0.1U$ obtained by different methods. . . . . p. 50

10 Density of states of the SIAM calculated within different approximation schemes for $\Gamma = 0.1U$, $T = 0.1U$, and $\varepsilon_0 = 0$. . . . . p. 50

11 Impurity density of states for $\Gamma = 0.02U$, $\varepsilon_0 = 0$ and $T = 0.1U$ near the Fermi level $\omega = 0$ obtained by different EOM schemes and also by the NCA. Here the estimated Kondo temperature is $T_K \sim 10^{-17}$ for $\varepsilon_0 = -U/2$. In the inset we show the density of states in a more extended range of energies. . . . . p. 51

12 Density of states in the particle-hole symmetric case, $\varepsilon_0 = -U/2$, for $\Gamma = 0.2U$, $T = 0.001U$. Here the estimated Kondo temperature is $T_K \approx 0.009U$. The inset shows a zoom of the region near the Fermi level $\omega = 0$. p. 52

13 Density of states obtained using the OCA method in the particle-hole symmetric case, $\varepsilon_0 = -U/2$, for $\Gamma = 0.2U$, $T = 0.0001U$. Here the Kondo temperature is $T_K \approx 0.009U$. Note that the height of the Kondo resonance is above the limit imposed by the Friedel sum rule, indicated by the dashed line. . . . . p. 53

14 SIAM density of states for $\Gamma = 0.2U$, $T = 0.001U$ and $\varepsilon_0 = -0.26U \simeq -U/4$ obtained from different approximation schemes. The inset shows a zoom of the region near the Fermi level $\omega = 0$. . . . . p. 54

15 Self-energy $\Sigma_1^r(\omega)$ in the EOM1 approximation for $\Gamma = 0.2U$, $T = 0.001U$, and $\varepsilon_0 = -0.26U$. . . . . p. 55

16 SIAM density of states obtained using EOM1 for $\Gamma = 0.2U$, $T = 0.001U$,and $\varepsilon_0 = -0.26U \approx -U/4$. The black line corresponds to the result shown in Fig. 14, while the red one is obtained by arbitrarily setting $\mathrm{Re}[\Sigma_1(\omega)] = 0$. . . . . p. 56

17 Real and imaginary parts of the function $P^r(\omega)$ as a function of the frequency ω for the EOM2 density of states of Fig. 14. . . . . p. 56

18 Real and imaginary parts of the function $Q^r(\omega)$ as a function of the frequency ω for the EOM2 density of states of Fig. 14. . . . . p. 57

19 Density of states of the SIAM in the EOM2 approximation and by imposing $P^r(\omega) = Q^r(\omega) = P^r(\omega_2) = Q^r(\omega_2) = 0$ for $\Gamma = 0.2U$, $T = 0.001U$, and $\varepsilon_0 = -2.6$ . . . . . p. 57

20 SIAM spectral function for $\Gamma = 0.2U$, $T = 0.001U$ and $\varepsilon_0 = 0$ obtained from different approximation schemes. The inset shows a zoom of the region near the Fermi level $\omega = 0$. . . . . p. 58

21 Condutance $\mathcal{G}$ as a function of the single particle energy ε_0 for $\mu = 0$, $\Gamma = 0.1U$, and different values of temperature (a) $T = 0.1U$, (b) $T = 0.01U$, (c) $T = 0.003U$, (d) $T = 0.001U$. . . . . p. 60

22 Conductance as a function of the impurity energy level for $\mu = 0$, and for different temperatures. (a)$T = 0.04U$, (b)$T = 0.003U$, (c)$T = 0.001U$, and (d) $T = 0.0004U$. The coupling strength here is $\Gamma = 0.2U$. . . . . p. 61

23 Conductance as a function of the impurity energy level for $\Gamma = 0.2U$,$T = 0.0001U$ calculated using OCA and NRG approaches. The Kondo plateau in the OCA method is above the quantum limit of conductance which is indicated by the blue dashed line. This unphysical feature is a consequence of the overestimation of the Kondo peak height whose correct value is obtained using the Friedel sum rule. . . . . p. 62

24 Conductance $\mathcal{G}$ as a function of the single-particle level energy ε_0/U for $\Gamma = 0.2U$. Note the increase of the NCA conductance for $\varepsilon_0 < -U$ and $\varepsilon_0 > 0$, when compared to the NRG result, as temperature decreases. . p. 63

25 Density of states of the SIAM for $\varepsilon_0 = -1.06U$, $\Gamma = 0.2U$, and different temperatures. Note that in the NCA result there is a resonance at the Fermi energy which does not appear in the NRG result (solid black line). The height of this resonance increases as the temperature decreases. . . p. 64

26 Conductance $\mathcal{G}$ in units of $2e^2/h$ as a function of the temperature T for (a) $\varepsilon_0 = -U/2$, (b) $\varepsilon_0 = -U/4$, (c)$\varepsilon_0 = 0$ corresponding respectively to the midvalley, a crossover, and the resonance peak configuration. Here $\Gamma = 0.2U$. . . . . p. 65

27 Conductance $\mathcal{G}$ in units of $2e^2/h$ as a function of the scaled temperature T/T_K for $\varepsilon_0 = -U/2$. Here $\Gamma = 0.2U$, $T_K^{\mathrm{OCA}} \approx 0.0028U$, $T_K^{\mathrm{NCA}} \approx 0.000097U$, and $T_K = 0.009U$[Haldane's expression]. . . . . p. 66

28 Summary of the performance of each impurity solver for the three temperature regions defined from the characteristic Kondo temperature of the quantum dot. . . . . p. 68

29 The DMFT maps the lattice problem (a) onto a single impurity problem coupled to an effective medium (b). The effect of the electronic correlations is contained in the self-energy Σ. Extracted from Ref. [26]. p. 74

30 Self-consistent cycle of DMFT. Extracted from Ref. [123]. . . . . p. 75

31 Bethe lattice with $\mathcal{Z} = 3$ and $K = 2$. Extracted from Ref. [125]. . . . . p. 76

32 Density of states ρ_σ as a function of the energy ω of the Hubbard model for $U = 0.4$ and $\beta = 7.2$ obtained using NCA and EOM as solvers. . . p. 79

33 Density of states of ρ_σ as a function of the energy ω of the Hubbard model for $U = 1$ and $\beta = 7.2$ obtained using NCA and EOM as solvers. p. 80

34 Density of states ρ_σ as a function of the energy ω of the Hubbard model for $U = 1.7$ and $\beta = 7.2$ obtained using OCA, NCA and EOM as solvers. p. 81

35 Density of states ρ_σ as a function of the energy ω of the Hubbard model for $U = 2.4$ and $\beta = 7.2$ obtained using OCA, NCA and EOM as solvers. p. 81

36 Density of states ρ_σ as a function of the energy ω of the Hubbard model for $U = 3.4$ and $\beta = 7.2$ obtained using OCA, NCA and EOM as solvers. p. 82

37 Contour plot of the OCA density of states as a function of U and ω for the half-filled Hubbard model (hypercubic lattice) and $\beta = 7.2$. . . . . p. 83

38 Contour plot of the NCA density of states as a function of U and ω for the half-filled Hubbard model (hypercubic lattice) and for $\beta = 7.2$. . . . p. 84

39 Contour plot of the EOM density of states as a function of U and ω for the half-filled Hubbard model (hypercubic lattice) and for $\beta = 7.2$. The dashed lines represent the curves $U(\omega) = \pm 2\omega$. The center of the two Hubbard bands approximately coincides with the points of these straight lines, indicating that the separation between the Hubbard bands is given by the interaction U. . . . . p. 85

40 Evolution of the density of states for the Hubbard model in a hypercubic lattice in the limit of infinite dimensions for different values of the interaction U and for $\beta = 1/T = 7.2$ obtained using (a) OCA, (b) NCA, and (c) EOM methods. . . . . p. 87

41 Summary of the performance of each impurity solver for the three main regions of the Mott transition: the metallic phase ($U < U_c$), close to the transition ($U \sim U_c$), and the insulating phase ($U > U_c$). . . . . p. 88

42 Density of states ρ_σ of the SIAM as a function of the energy ω for $U = 10$ (arbitrary units), $\Gamma = 0.02U$, $\varepsilon_0 = -U/2$, and $T = 0.1U$ obtained using the indicated EOM solvers. The main plot is a zoom near the region $\omega = \varepsilon_0$ and highlights the surprising discrepancy between the different approaches. The inset is a plot in a more extended energy region. . . . p. 96

Contents

1 Introduction p. 15

2 Anderson Model: a case study for different impurity solvers p. 27

2.1 Equations of motion method . . . . . p. 28

2.2 Slave boson methods: non crossing and one crossing approximations . . p. 38

3 Numerical analysis p. 47

3.1 Spectral functions and density of states . . . . . p. 48

3.2 Conductance . . . . . p. 59

4 Dynamical Mean Field Theory p. 69

4.1 The self-consistency condition . . . . . p. 72

4.2 Hubbard model for the Bethe and hypercubic lattices . . . . . p. 75

4.3 Successes and limitations of the DMFT . . . . . p. 77

5 DMFT - Results p. 78

6 Conclusions p. 89

Appendix A – EOM Green's functions in the particle-hole symmetric case p. 92

A.1 Proof of the equality $\Sigma_1(\omega) = \Sigma_0(\omega)$ . . . . . p. 93

A.2 Proof of the equality $\Sigma_3(\omega) = 2\Sigma_0(\omega)$ . . . . . p. 93

A.3 EOM Green's function at the particle-hole symmetric point . . . . . p. 94

Appendix B – Kramers Kroning relations for non uniform frequency meshes p. 97

References p. 99

1 Introduction

The Anderson impurity model was originally formulated to study non magnetic metals containing diluted magnetic impurities in 1961 by Phillip W. Anderson [1]. Nowadays it is one of the most important models in condensed matter physics playing an important role on the study of a huge variety of strongly correlated systems. Let us give a brief review on how this protagonism has been developed over the years.

Since the 1930s many experiments have shown that the presence of diluted magnetic impurities in non magnetic metals dramatically changes their physical properties, such as the magnetic susceptibility, the resistivity, the specific heat, etc. [2]. Figure 1a shows a representative result of such an experiment. One can see that as the temperature is lowered the resistance decreases until it reaches a minimum and then increases under further cooling. However, this behavior clearly differs from both a pure metal and a superconductor. For a pure metal the resistivity saturates at a constant value which depends essentially on the number of defects in the material. For a superconductor the resistivity vanishes below a critical temperature, see Fig. 1b [3].

It was only in 1964 that an explanation for this minimum in the resistivity was given in the seminal work of Jun Kondo [5]. In his theory the interaction between the spin of the magnetic impurity and the spins of the conduction electrons plays an essential role and is the key ingredient of the so-called s-d exchange or Kondo model [2,5], that assumes that the impurity has a local magnetic moment. Using perturbation theory in the spin interaction Kondo demonstrated that the impurity acts as an scattering center for the conduction electrons adding a logarithmic contribution to the resistivity of the material as a function of the temperature, namely,

$$\mathcal{R}(T) = \mathcal{R}_0 + aT^2 + bT^5 + c[1 - \rho(\varepsilon_F)J]\ln(T)\ . \tag{1.1}$$

Here $\mathcal{R}_0$ is the (temperature independent) resistivity due to the defects in the material, a is the coefficient of the electron-electron interaction contribution, b stems from electron-phonon interaction, c is a coefficient that depends on the concentration of impurities,

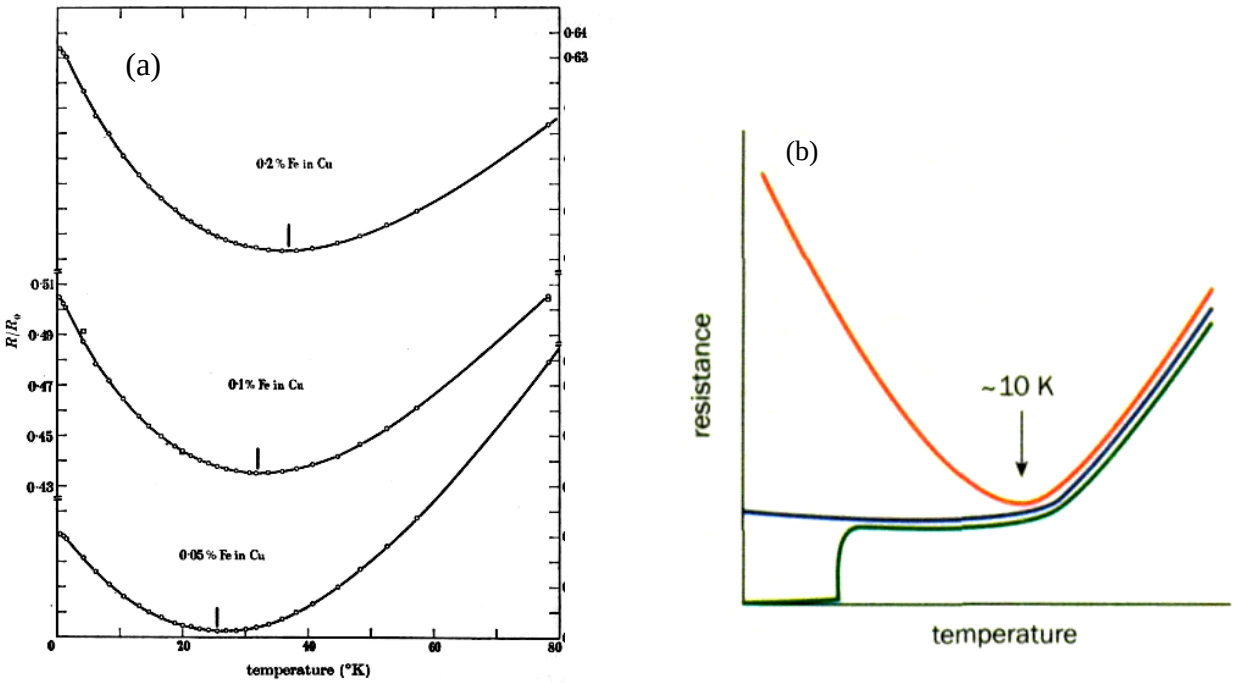

Figure 1: (a) Resistance as a function of the temperature of an alloy of Cu (host metal) and Fe (magnetic impurity). Note the minimum in the resistance as mentioned in the text. Note also that the value of the minimum depends on the concentration of the impurities. Extracted from Ref. [4]. (b) In a pure metal (blue line) the resistance saturates below a certain temperature (typically $10K$). In a superconductor (green line), the resistance vanishes below a critical temperature. In a metal containing magnetic impurities (red line) the resistance reaches a minimum and start increasing again. Extracted from Ref. [3].

$\rho(\varepsilon_F)$ is the density of states at the Fermi level, and J is the effective exchange coupling between the impurity spin and the conduction electrons spins.

The scattering occurs by means of the so-called *exchange processes* in which the unpaired impurity electron tunnels into a state near the Fermi level of the metal as shown in Fig. 2. Then a conduction electron can tunnel into the impurity to occupy the localized level. In this process the final spin state can be different from the initial one so that exchange process can effectively flip the spin of the impurity (see Fig. 2). In a dilute magnetic alloy, such events occurs all the time and taken together they give rise to the so-called *Kondo effect*. The Kondo effect is the underlying physical process behind the minimum of resistivity and its increasing below the minimum discussed above. It takes place when the temperature is near a characteristic temperature T_K of the system, called the Kondo temperature. The combined effect of many exchange processes produces a new resonance - usually called the *Kondo* or *Abrikosov-Suhl resonance* - in the energy spectrum of the material. Later, it has been shown that the width of this resonance is proportional to T_K establishing an important energy scale which determines all the low-temperature properties of the system [2]

The physical picture to justify the microscopic Hamiltonian model is the following: The "magnetic" character of an impurity depends on both the host metal and the presence of atoms with partially filled d or f shells. Although these orbitals are more localized than the s or p ones, in some combinations of host metal and impurity, the overlap between the conduction electrons wave functions and the localized d or f shell ones can be strong enough to produce a delocalization of the impurity electron states, hence destroying the magnetic moment, as recognized in the Ref. [6]. It was then realized the importance of understanding what were the conditions for the existence of a localized moment in a metal and what were the consequences of the interaction between a localized moment and the conduction electrons [2]. In this context, Anderson [1] proposed his famous model in order to explain the formation of the localized magnetic moments in a metal. The Hamiltonian of the Anderson model in its simplest version reads

$$H = \sum_{\mathbf{k}\sigma} \varepsilon_{\mathbf{k}} c^{\dagger}_{\mathbf{k}\sigma} c_{\mathbf{k}\sigma} + \sum_{\sigma} \varepsilon_0 f^{\dagger}_{\sigma} f_{\sigma} + U n_{\uparrow} n_{\downarrow} + \sum_{\mathbf{k}\sigma} \left(V_{\mathbf{k}} f^{\dagger}_{\sigma} c_{\mathbf{k}\sigma} + H.c. \right) , \tag{1.2}$$

which is usually called the *Single Impurity Anderson Model* (SIAM). The first term of the Hamiltonian corresponds to kinetic energy of the free electrons of the metal occupying states indexed by the momentum $\mathbf{k}$ and spin projection σ. The second and third terms refer to the impurity, which consists of a single localized level with energy ε_0, see Fig. 2. The impurity can be empty, occupied by one spin up electron, by one spin down electron or by two electrons with opposite spins. For double occupancy of the impurity the two electrons experience a Coulomb repulsion translated into the charging energy U in the third term. Finally, the last term is the hybridization Hamiltonian which allows for an electron to hop between the impurity and the conduction band states. In his work, Anderson described the crossover between a magnetic and non magnetic regimes by means of a self-consistent Hartree-Fock treatment of Eq. (1.2). He also computed the susceptibility and the specific heat of the model at the Hartree-Fock level. By going beyond the mean-field approximation the SIAM has been used to sucessfully describe Kondo physics [2, 7]. Schrieffer and Wolff later showed that both the SIAM and the s-d exchange models are equivalent to each other in the limit of weak hybridization between the impurity and the conduction electron states [8]. It should be emphasized that the Anderson model is more general in the sense that it allows for charge fluctuations in the impurity, unlike the Kondo model, which already assumes the existence of a magnetic moment at the impurity

At a first moment, the advances in the theory of the exchange model theory were a little ahead of the theoretical developments concerning the Anderson model [2]. Due to its

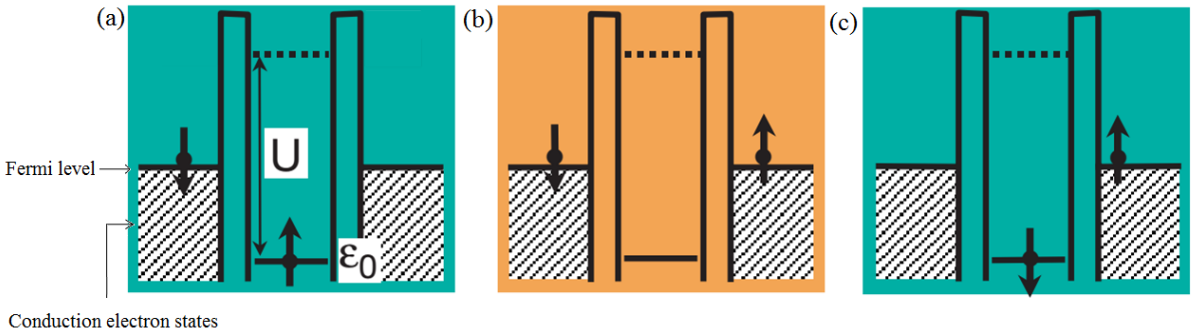

Figure 2: (a)Schematic energy diagram of the single impurity Anderson model. A single particle localized level with energy ε_0 is coupled to a continuum of states (indicated in the figure) representing the free electrons of the metal. In the situation depicted the impurity is occupied with one spin-up electron. Double occupancy is prohibited by the Coulomb energy U. (b) *Exchange process*: The spin-up electron may tunnel out of the impurity and occupy a conduction band state near the Fermi level leaving room for a bath electron with opposite spin to hop into the impurity site. (c) The result of this process is an effective change of the impurity spin. See discussion in the text. Adapted from Ref. [9].

capability to describe charge fluctuations, the interest in the Anderson model surpassed the *s-d* model in view of the mixed valence problem [2, 10, 11].

Despite the great success of the Kondo perturbative approach to correctly describe the behavior of the resistivity around T_K, it fails dramatically as $T \to 0$ predicting an infinite resistivity. This inconsistency was only fully solved after the seminal work of Wilson [12, 13]. Based on the Anderson "scaling" ideas, Wilson developed the numerical renormalization group (NRG), a powerful non-perturbative method which showed that for $T \ll T_K$ all physical quantities of a dilute magnetic alloy have a simple power law behavior [2]. Wilson's work also showed that as $T \to 0$ the coupling between the impurity and the conduction electrons increases indefinitely which leads to a complete compensation of the impurity magnetic moment by the conduction electrons [2]. In other words, the local magnetic moment is entirely screened by the spins of the electrons in the metal and the ground state of the impurity is a singlet one [3]. Later a perturbation theory in U developed by Yosida and Yamada for the Anderson model also confirmed the Wilson results [14–16].

Although great progresses has been made and a deep understanding of the Kondo effect has already been reached, the interest in the problem did not diminish. From the experimental side, realizations of Kondo physics in quantum dots [17,18] and in molecular electronics [19,20] rekindled the attention to the effect. On the theoretical side the Kondo effect became an attractive platform to study and develop numerical and analytical tech-

niques which have proved to be very useful in a variety of many-body problems [3]. In several contexts, the Kondo effect provides important clues to understand strongly correlated systems like heavy-fermion compounds and high temperature superconductors [3,7].

In this scenario, many impurity solvers were developed. An important step to be taken at that time was to find solutions for the degenerate versions of the *s*-*d* and Anderson models which are more realistic for magnetic impurities in the sense that they include the orbital degeneracy of the *d* and *f* electrons. In the 80's an exact solution for both *s*-*d* and Anderson models using the Bethe ansatz was found [21–24]. The results covered both the degenerate and non-degenerate versions of these models. These theoretical developments were timely because at that time experiments on dilute and concentrated alloys containing rare-earth elements such as Ce and Yb had shown Kondo-like anomalies over a wide concentration range [7]. The Bethe ansatz have been applied to the degenerate *s*-*d* and Anderson models, more appropriate for these systems since for Ce, $N_{\rm deg} = 6$ and Yb, $N_{\rm deg} = 8$, and the theoretical results compare very well with such experiments.

Other types of experiments such as photoemission spectra and neutron scattering, demand the knowledge of the dynamic response functions of the systems, something the Bethe ansatz results could not provide [7, 25]. In this context many techniques were developed based on treating $1/N_{\rm deg}$ as a small parameter such as slave boson mean field calculations, the non-crossing approximation, variational approaches, etc. [7].

The problem of a magnetic impurity embedded in a non-magnetic metal has proved to be a very challenging problem for the physicists since the 30's. But an even more challenging problem was to understand the properties of a whole crystal lattice containing transition elements and rare-earth atoms, namely, transition metals and their oxides, Kondo lattices, heavy fermion systems. In transition metal oxides, for example, the usual band theory predicts that some of these compounds should be metallic. However, many experiments showed that they behave as an insulator [26]. In fact, they belong to a different class of insulators known as Mott insulators in which the electron-electron interaction plays a crucial role [27–29]. Hence, in order to understand these materials it is necessary to go beyond the tradicional band theory since it neglects the effects of the electron-electron interaction. The basic approach to study these materials consists of using model Hamiltonians containing only the relevant degrees of freedom to explain a determined phenomena. In this context the Hubbard model, the periodic Anderson model and the Kondo lattice model were proposed and became standard models to address lattice many-body problems [30–32]. However, the task of finding solutions for these models has

proven to be a very difficult one. Some progress has been made, for instance, Ref. [33] has found a solution for the one-dimensional Hubbard model. Nevertheless the properties of the model in higher dimensions remained a great theoretical challenge.

In the late 80's and early 90's, scientists have found that it was possible to map a lattice many-body problem into an effective single impurity problem, which can be addressed using the Anderson model [30]. This map is exact in the limit of infinite dimensions and is an approximation for finite dimensions. These findings gave rise to the so-called Dynamical Mean Field Theory (DMFT) in which the solution of the single impurity Anderson model plays a crucial role. The DMFT allowed for great progresses in the understanding of the properties of the lattice many-body models hence reaching a wide variety of strongly correlated systems [30]. Nowadays the combination of DMFT with electronic structure methods like the local density aproximation (LDA) of the density function theory (DFT) [34, 35], the so-called LDA+DMFT method, allows for the study of strongly correlated materials in a more reallistic way taking into account the details of the particular electronic structure of each system [36, 37].

In view of the DMFT and LDA+DMFT approaches to strongly correlated systems the search for other methods for solving the single impurity Anderson model are of interest since DMFT requires the whole single particle excitation spectrum of the system [30]. Unfortunately, there is no single impurity solver that can provide reliable results for all the energies of the spectrum. For example, the numerical renormalization group of Wilson is most suitable to describe the low-energy excitations and must be combined with other methods that can provide an accurate description of the high energy features of the spectrum [30, 38]. Bethe ansatz results have little use in DMFT since it assumes a constant density of states for the effective bath of conduction electrons [30]. Perturbation theory in U gives good results but the accuracy of these results is restricted to the symmetric Anderson model [30]. Furthermore, in many contexts, the Coulomb interaction is usually one of the larger energy scales of the problem and expansion in U is not convenient. In this scenario, impurity solvers like the Quantum Monte Carlo (QMC), the exact diagonalization, the slave boson mean-field theory, the non-crossing and one-crossing approximations, the equations of motion and other methods which can yield explicit expressions for the impurity Green's functions at all energies have gained great attention despite the fact that all of them suffer from limitations in some parameter range [30].

Back to the Kondo effect, as mentioned before, the interest in this phenomenon was particularly revived from the late 80's in view of the new experimental set ups made

possible thanks to the fabrication of quantum dots (QD) and single electron transistors (SET) [17,39]. Quantum dots and single electron transistors are small islands of a conductive material where electrons can be confined as shown in Fig. 3. The confined "droplet" of electrons is coupled to an electron gas by quantum mechanical tunneling junctions. In a QD the commom set up consists of connecting the island to two electron reservoirs usually denoted as "source" and "drain" leads [17]. In a SET the "droplet" is also connected to a third electrode usually called the gate electrode [17]. In general, one is concerned with the transport properties of a QD or a SET. When a voltage $V_{\rm sd}$ is applied between the source and drain contacts a current can flow through the island. The transport properties can be studied by measuring the current or the conductance as a function of the voltage $V_{\rm sd}$ or the gate voltage V_g.

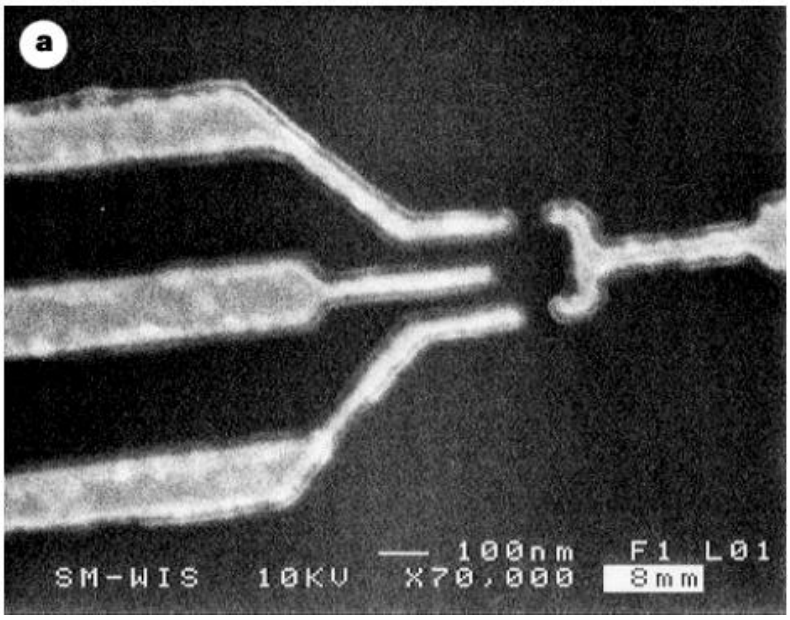

Figure 3: Single electron transistor. Metallic gates (white regions) on the surface of a semiconductor heterostructure containing a two dimensional electron gas (dark region). The upper and lower electrodes on the left and the electrode in the right are used to control the tunnel barriers between the island of electrons and the electron gas (at top and bottom). The middle terminal in the left is the gate electrode. The source and drain contacts (not shown) are at the top and bottom of the image, respectively. Extracted from Ref. [40]

.

Due to the confinement of the electrons, the single particle energy levels of both QD and SET form a discrete spectrum, with typical spacing $\Delta\epsilon$, similarly to what happens in an atom. Due to this analogy these devices are often called artificial atoms [40]. By means of the gate terminal capacitively coupled to the SET one can tune the position of these energy levels with respect to the Fermi level of the leads. If V_g is tuned such that an

energy level of the SET coincides with the Fermi level of the leads, then electrons can hop into and out of the island. In other words the charge in the SET can fluctuate between N and $N+1$ electrons. In this way, a current can flow in the circuit which translates into a peak in the zero bias conductance of the SET as shown in Fig. 4. As V_g is varied the conductance exhibits a sequence of equally spaced peaks as shown in Fig. 4.

Every time an energy level of the SET is lowered below the Fermi energy of the leads, the number of electrons in the droplet is increased by one. Hence the number of electrons in the island can be controlled by the gate voltage. Moreover the addition of an electron will increase the energy stored in the island since the energy of $N+1$ electrons is greater than the energy of N electrons in the SET due to both the Coulomb repulsion and the occupation of new single particle levels in the dot. However, in a SET the level spacing $\Delta\epsilon$ between the single particle energy levels is generally much smaller than the Coulomb interaction, that is, $\Delta\epsilon \ll U$ [17]. This means that the addition of the next electron to the SET costs an extra energy due to essentially the Coulomb repulsion. Hence, there is no current flow unless the Coulomb charging energy U is provided by increasing the gate voltage. This corresponds to the valleys between the peaks in Fig. 4. This phenomenon in which the conductance of a SET exhibit a pattern of peaks and valleys is usually called the *Coulomb blockade* [41–44]. As the temperature is decreased, the peaks become sharper and higher due to the sharpening of the Fermi distribution [40] and hence the valleys become deeper and larger due to a decrease of thermally excited transport through the island [45].

In contrast, for small quantum dots the conductance in some valleys can increase as the temperature is lowered [47]. When the number of confined electrons is odd, there is at least one unpaired electron inside the "droplet" or Coulomb island and the total spin of the dot has a minimum value of $S = 1/2$. In this case, the quantum dot plays an analogous role of a magnetic impurity embedded in a non-magnetic metal as discussed above. As such, one may also observe the Kondo effect in quantum dots [9, 40, 47, 48]. In a bulk metal containing magnetic impurities the scattering of the conduction electrons in the Kondo regime leads to an increase in the resistivity. In a quantum dot one observes an opposite effect. Since the island is the only path an electron can travel from the source to drain, the Kondo resonance favors the current. Hence, in quantum dots the Kondo effect produces an increase in the conductance in the valley region between the Coulomb blockade peaks, see Fig. 5. For $T \ll T_K$ the conductance reaches its quantum limit of $2e^2/h$ leading to the formation of a plateau (the Kondo plateau) in the $G \times V_g$ curve [49], Fig. 5.

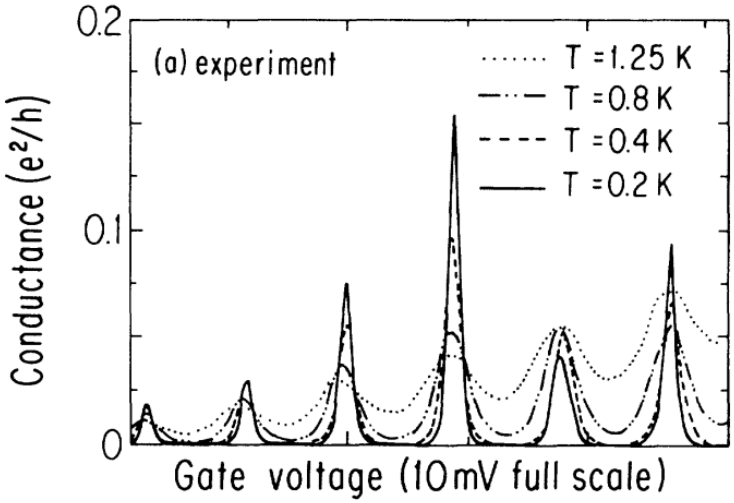

Figure 4: Zero bias conductance as function of the gate voltage for different values of temperature. The alternating pattern of peaks and valleys in the conductance is the hallmark of the Coulomb blockade. Extracted from Ref. [46].

Actually, one of the main new features of gated quantum dots is the possibility of studying the Kondo effect in a controllable manner. Indeed, as shown in Fig. 3, by means of several electrodes it is possible to adjust the size, shape and interactions inside the island as well as the tunnel barries coupling the quantum dot to the conduction electrons [3]. This gives unprecedent control over the parameters involved in the Kondo

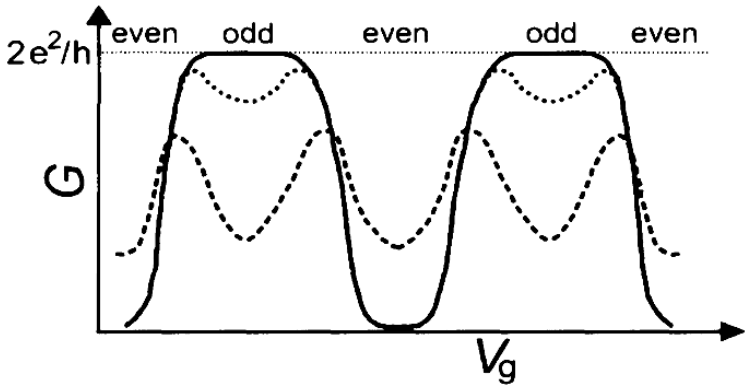

Figure 5: Schematic representation of the zero bias conductance of a quantum dot as a function of the gate voltage. The solid curve is for $T \ll T_K$, the dotted curve for $T \approx T_K$, and the dashed curve for $T > T_K$. For odd electron number in the dot the conductance increases as the temperature is lowered due to the Kondo effect reaching the quantum limit of conductance $2e^2/h$ for $T \ll T_K$. For even electron number in the dot the Kondo effect doesn't occur. The conductance decreases as the temperature is lowered due to a decrease of thermally excited transport through the dot. Extracted from Ref. [45].

effect something that is not possible in the case of a dilute magnetic alloy.

The interest in quantum dots is not restricted to the study of the effects of strong correlations in a basic science perspective. Actually it has been viewed in electronics as a promising alternative to silicon based technologies, for instance, in the fabrication of ultra-densely integrated electronic circuits [17]. In these devices, the extreme miniaturization in the scale of tens of nanometers poses serious limitations to the conventional field effect transistors (FET's) since problems with heat dissipation, vanishing bulk properties, undesirable quantum tunneling effects, etc. become hard and costly to handle [17].

Like quantum dots, molecular electronic devices also have received great attention from the nanoscience research community [19, 20, 50]. In Fig. 6 we show the typical experimental set up of such devices, a molecule connected to metallic nanocontacts [20,51]. The advantages of using molecules include - but are not limited to - the relative low cost to design, build and replicate them in comparison with nanostructures built from bulk solids [17]. Those are features highly desirable for industrial-scale production of ultra-dense nanoelectronic computers [17].

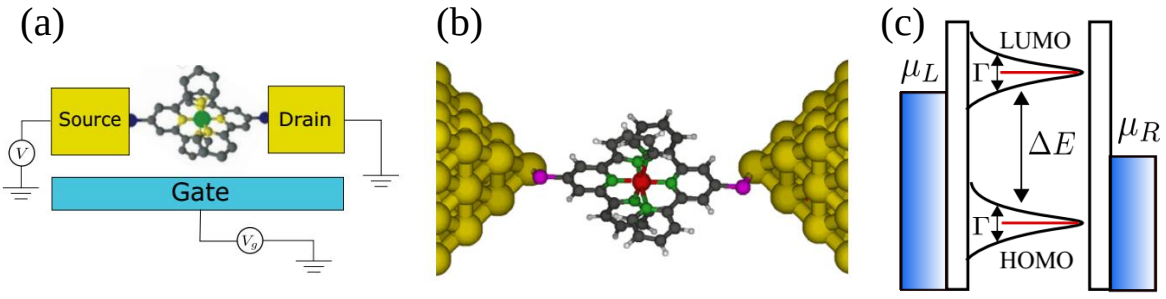

Figure 6: (a) Typical experimental set up encountered in molecular electronics: a magnetic organic molecule, [Co(tpy-SH)2]2+, coupled to the tips of nanocontacts. (b) The proper theoretical description of such devices need to take into account the realistic atomic and electronic structures of both the electrodes and the molecule. (c) Schematic representation of the energy diagram of the situation depicted. The molecular energy levels are broadened due to the hybridization with the electrodes. Figure 6a taken from Ref. [20]. Figure 6b extracted from Ref. [51] and Fig. 6c has been provided by Prof. Alexandre Reily Rocha (IFT-UNESP).

The literature in the subject is vast and has shown important progresses in the field [17, 52]. Exciting attempts to devise molecular structures acting as switches like in conventional FET's have been reported [20]. However it is clear from these advances that the success of this endeavour also depends on a proper theoretical description of the experiments. This necessarily demands a realistic account of the atomic and electronic

structure of these devices [51, 53, 54]. At the same time it is also crucial to take into account quantum effects, naturally present at the nanometer scale.

The most used approach for the description of molecular electronic devices is the combination of the density functional theory (DFT) with the Landauer transport theory [55] or with the non-equilibrium Green's function formalism (NEGF) [52,56,57]. The approach works very well in many contexts [51]. However molecule based devices containing magnetic atoms display strong correlations, which are not properly described by DFT. Indeed, transport experiments in molecular devices have reported the manifestation of the Coulomb blockade and the Kondo effects in the zero bias conductance of these systems [19,20]. Furthermore strong correlations could enhance the functionality of molecular devices by exploiting the spin degree of freedom of the electron in addition to its charge [51].

The successes of DMFT in the understanding of the electronic properties of strongly correlated materials have led to the proposition in the literature of combining DMFT ideas in the DFT+NEGF method [51,53,58]. This DFT+DMFT+NEGF approach consists of correcting the DFT electronic structure of the device in order to include the effect of strong correlations [51,53,58]. Roughly speaking this correction involves the projection of the Kohn-Sham Hamiltonian of the system into the correlated subspace of a set of localized molecular states. This process results in the problem of an impurity coupled to an effective bath. Once again one is faced with the task of solving the Anderson impurity model which is in general the most difficult step of the approach.

Unfortunately, due to the great theoretical and computational challenge the implementation of this approach represents, the works in this field are still incipient. However, there is no doubt that the successful description of the correlation effects in molecular devices could lead to a great progress of the molecular electronics research field.

In all these aforementioned contexts, the solution of the Anderson impurity model is a crucial step for a proper understanding of these system properties. The Anderson model can be solved numerically by several methods, which differ mainly by the computational cost involved and by the range of the model parameters where the used method is reliable. Unfortunately, none of them can be used isolatedly. Instead, it is often necessary a combination of methods in order to acquire quantitative and qualitative understanding of the systems properties. Given the variety of available methods and scenarios in which the Anderson model can be applied the task of benchmarking impurity solvers in each context is still important and far from being exhausted. One will always encounter some

aspects that make one solver more competitive in some range of parameters which can influence the choice of the solver to be used.

In this thesis we benchmark some impurity solvers for the SIAM in two contexts. Firstly, in the context of a QD, we compute its Green's function using different methods in order to obtain the density of states and the zero bias conductance of the dot. Next we study the Hubbard model using the Dynamical Mean Field Theory with different impurity solvers. In Chapter 2 we present the methods that will be used in this thesis, namely, EOM, OCA, NCA. In Chapter 3 we present the results obtained in the study of a QD paying attention to the Coulomb blockade regime and the Kondo effect. In Chapter 4 we present the equations and ideas of the DMFT. In Chapter 5 we discuss the solutions of different solvers for the Hubbard model applied to an infinite dimensional cubic lattice. Finally, in Chapter 6 we present our conclusions.

2 Anderson Model: a case study for different impurity solvers

In this chapter we study the Green's function and the conductance of a single level quantum dot, modeled by the single impurity Anderson model (SIAM) [1]. We compare the results obtained by different impurity solvers, namely truncated equations of motion (EOM) [46, 59], and slave boson at the non-crossing (NCA) and one-crossing approximations (OCA) levels [60–62]. We benchmark the different methods by calculating the density of states and the linear conductance for different model parameters.

The SIAM Hamiltonian reads

$$H = H_{\text{imp}} + H_C + H_{\text{lead}} \ , \tag{2.1}$$

where

$$H_{\text{imp}} = \sum_{\sigma} \varepsilon_0 f_\sigma^\dagger f_\sigma + U n_\uparrow n_\downarrow \ , \tag{2.2}$$

represents the single-level quantum-dot Hamiltonian, $f_\sigma(f_\sigma^\dagger)$ is the annihilation (creation) operator of an electron of spin $\sigma =\uparrow,\downarrow$ at the state of energy ε_0, U is the charging energy, and n_σ is the occupation operator.

The quantum dot is connected to leads (or terminals) represented by

$$H_{\text{lead}} = \sum_{\substack{\mathbf{k}\sigma \\ \alpha\in L,R}} \varepsilon_{\mathbf{k}\alpha} c_{\mathbf{k}\alpha\sigma}^\dagger c_{\mathbf{k}\alpha\sigma} \ , \tag{2.3}$$

which are in equilibrium with reservoirs (for simplicity we consider the two-terminal $\alpha = R, L$ case). Here $c_{\mathbf{k}\alpha\sigma}(c_{\mathbf{k}\alpha\sigma}^\dagger)$ is the annihilation (creation) operator of an electron at the α-lead with wavevector $\mathbf{k}$ and spin σ.

Finally, the impurity-lead coupling term is given by

$$H_{\rm C} = \sum_{\substack{\mathbf{k}\sigma \\ \alpha\in L,R}} \left(V_{\mathbf{k}\alpha} f^\dagger_\sigma c_{\mathbf{k}\alpha\sigma} + H.c. \right) \tag{2.4}$$

with obvious notation.

We study the linear conductance $\mathcal{G}$ of the system defined by Eq. (2.1). In this limit it was recently shown [63] that $\mathcal{G}$ can be calculated even beyond the proportional coupling regime [64, 65] by

$$\mathcal{G} = -\frac{2e^2}{h} \sum_\sigma \int_{-\infty}^{\infty} d\epsilon \left(-\frac{\partial f(\varepsilon)}{\partial \epsilon} \right) \Gamma_\sigma(\epsilon)\, \mathrm{Im}[G^r_\sigma(\epsilon)]. \tag{2.5}$$

Here, $G^r_\sigma(\varepsilon)$ is the Fourier transform of the full retarded Green's function, namely,

$$G^r_\sigma(t) = -i\theta(t)\langle\{f_\sigma(t) f^\dagger_\sigma(0)\}\rangle, \tag{2.6}$$

$f(\varepsilon) = 1/(1+e^{\beta\varepsilon})$ is the Fermi distribution, and

$$\Gamma_\sigma(\varepsilon) = \Gamma^L_\sigma(\varepsilon)\Gamma^R_\sigma(\varepsilon)/[\Gamma^L_\sigma(\varepsilon) + \Gamma^R_\sigma(\varepsilon)] \ , \tag{2.7}$$

where the α-lead decay width $\Gamma^\alpha_\sigma(\varepsilon)$ is given by

$$\Gamma^\alpha_\sigma(\varepsilon) = 2\pi \sum_{\mathbf{k}} |V_{\mathbf{k}\alpha}|^2 \delta(\varepsilon - \varepsilon_{\mathbf{k}\alpha}) \ , \quad \alpha = L, R \ . \tag{2.8}$$

Next we will review the methods we use to calculate the Green's functions G^r_σ, namely, equations of motion (EOM) and slave-boson approximation (SBA).

2.1 Equations of motion method

The EOM technique consists of building a set of coupled equations relating the different possible correlation functions of the system. The standard procedure is to take the time derivative of the Green's functions of interest. The corresponding differential equation contains usually Green's functions involving different kind of operators. For bilinear Hamiltonians the number of possible different correlation functions is finite and the equations of motion close. Hence the system of equations can be solved exactly. For Hamiltonians with many-body interactions, the number of coupled equations is infinite, involving a hierarchy of growing complexity correlation functions. Since the method does not rely on a small parameter expansion it is necessary to truncate the equations

by means of some reasonable physical arguments, yielding approximate solutions to the problem [66].

Let us ilustrate some steps of the method by calculating the dot Green's function, defined by (see Ref. [67] for a more detailed derivation)

$$G_\sigma(t-t') = -i\langle T\{f_\sigma(t)f_\sigma^\dagger(t')\}\rangle \ , \tag{2.9}$$

The corresponding EOM reads

$$i\frac{\partial}{\partial t}G_\sigma(t-t') = \delta(t-t') + \varepsilon_0 G_\sigma(t-t') + UG^{(2)}(t-t') + \sum_{\mathbf{k}\alpha} V_{\mathbf{k}\alpha}^* \Lambda_{\mathbf{k}\alpha\sigma}(t-t') \ , \tag{2.10}$$

with

$$G^{(2)}(t-t') \equiv -i\langle T\{f_\sigma(t)f_{\bar\sigma}^\dagger(t)f_{\bar\sigma}(t)f_\sigma^\dagger(t')\}\rangle \ , \tag{2.11}$$

$$\Lambda_{\mathbf{k}\alpha\sigma}(t-t') = -i\langle T\{c_{\mathbf{k}\alpha\sigma}(t)f_\sigma^\dagger(t')\}\rangle \ , \tag{2.12}$$

where we used the Heisenberg equation for the annihilation operator d_σ, namely,

$$i\dot{f}_\sigma = -[H, f_\sigma] = \varepsilon_0 f_\sigma + U f_\sigma n_{\bar\sigma} + \sum_{\mathbf{k}\alpha} V_{\mathbf{k}\alpha}^* c_{\mathbf{k}\alpha\sigma} \ . \tag{2.13}$$

Note that for $U = 0$ the EOM involves only G_σ and $\Lambda_{\mathbf{k}\alpha\sigma}$. In this case, by writing an EOM for $\Lambda_{\mathbf{k}\alpha\sigma}$ the set of coupled equations close, and the exact solution is readily obtained. For $U \neq 0$, a Green's function involving 4 operators appears, $G^{(2)}$. As we discuss below the EOM for $G^{(2)}$ involves other hierarchically more complex Green's functions and the set of equations never closes. In energy representation, Eq. (2.10) can be written as

$$(\omega - \varepsilon_0)G_\sigma(\omega) = 1 + UG^{(2)}(\omega) + \sum_{\mathbf{k}\alpha} V_{\mathbf{k}\alpha}^* \Lambda_{\mathbf{k}\alpha\sigma}(\omega) \ , \tag{2.14}$$

We find that $\Lambda_{\mathbf{k}\alpha\sigma}$ satisfies

$$(\omega - \varepsilon_{\mathbf{k}\alpha})\Lambda_{\mathbf{k}\alpha\sigma} = V_{\mathbf{k}\alpha}G_\sigma(\omega) \ . \tag{2.15}$$

Substituting this result in Eq. (2.14) we obtain

$$[\omega - \varepsilon_0 - \Sigma_0(\omega)]G_\sigma(\omega) = 1 + UG^{(2)}(\omega) \ , \tag{2.16}$$

where

$$\Sigma_0(\omega) = \sum_{\mathbf{k}\alpha} \frac{|V_{\mathbf{k}\alpha}|^2}{\omega - \varepsilon_{\mathbf{k}\alpha}} \ , \tag{2.17}$$

is the noninteracting self-energy due to the coupling to the leads, sometimes called em-

bedding self-energy [68].

The EOM for $G^{(2)}$ is given by

$$(\omega-\varepsilon_0-U)G^{(2)}(\omega)=\langle n_{\bar{\sigma}}\rangle+\sum_{\mathbf{k}\alpha}V^*_{\mathbf{k}\alpha}\Lambda^{(2)}_{1,\mathbf{k}\alpha}(\omega)+V_{\mathbf{k}\alpha}\Lambda^{(2)}_{2,\mathbf{k}\alpha}(\omega)-V^*_{\mathbf{k}\alpha}\Lambda^{(2)}_{3,\mathbf{k}\alpha}(\omega)\ , \quad (2.18)$$

which generates new correlation functions, namely,

$$\begin{aligned}
\Lambda^{(2)}_{1,\mathbf{k}\alpha}(t-t')&\equiv -i\langle T\{c_{\mathbf{k}\alpha\sigma}(t)n_{\bar{\sigma}}(t)f^\dagger_\sigma(t')\}\rangle\ ,\\
\Lambda^{(2)}_{2,\mathbf{k}\alpha}(t-t')&\equiv -i\langle T\{c^\dagger_{\mathbf{k}\alpha\bar{\sigma}}(t)f_\sigma(t)f_{\bar{\sigma}}(t)f^\dagger_\sigma(t')\}\rangle\ ,\\
\Lambda^{(2)}_{3,\mathbf{k}\alpha}(t-t')&\equiv -i\langle T\{c_{\mathbf{k}\alpha\bar{\sigma}}(t)f^\dagger_{\bar{\sigma}}(t)f_\sigma(t)f^\dagger_\sigma(t')\}\rangle\ .
\end{aligned} \quad (2.19)$$

It is interesting to note that, as the noninteracting problem ($U=0$) discussed above, the isolated interacting dot ($U\neq 0$) also has a simple solution. If we take $V_{\mathbf{k}\alpha}=0$ and

$$\Lambda^{(2)}_{1,\mathbf{k}\alpha}(\omega)=\Lambda^{(2)}_{2,\mathbf{k}\alpha}(\omega)=\Lambda^{(2)}_{3,\mathbf{k}\alpha}(\omega)=\Sigma_0(\omega)=0\ , \quad (2.20)$$

we find that $G_\sigma(\omega)$ satisfies

$$G_\sigma(\omega)=\frac{\langle n_{\bar{\sigma}}\rangle}{\omega-\varepsilon_0-U}+\frac{1-\langle n_{\bar{\sigma}}\rangle}{\omega-\varepsilon_0}\ . \quad (2.21)$$

This is the atomic limit usually considered in the Hubbard I approximation [29, 69].

Recalling that $G^<_\sigma(t)=i\langle f_\sigma(t)f^\dagger_\sigma(0)\rangle$ we write

$$\langle n_{\bar{\sigma}}\rangle=\int\frac{d\omega}{2\pi i}G^<_\sigma(\omega)\ . \quad (2.22)$$

Since we are interested in the linear response regime, we can use the fluctuation-dissipation theorem, $-iG^<_\sigma(\omega)=2f(\omega)\mathrm{Im}[G^r_\sigma(\omega)]$, to arrive at [67]

$$\langle n_{\bar{\sigma}}\rangle=-\frac{1}{\pi}\int d\omega f(\omega)\mathrm{Im}[G^r_\sigma(\omega)]\ . \quad (2.23)$$

The retarded Green's function is obtained with the substitution $\omega\to\omega+i\eta$. It consists of two peaks (resonances) at $\omega=\varepsilon_0+U$ and $\omega=\varepsilon_0$ weighted by $\langle n_{\bar{\sigma}}\rangle$ and $1-\langle n_{\bar{\sigma}}\rangle$, respectively [67]. Here ε_0 and ε_0+U are the single and double occupation resonance energies.

Next, we need to consider the coupling to the bath to describe the quantum dot transport properties. In the weak coupling limit, $\mathrm{Im}\Sigma^r_0(\omega)\ll U$[1], one can assume that the leads do not significantly change the self-energy and change G_σ *ad hoc* as $G^{-1}_\sigma\to G^{-1}_\sigma-\Sigma_0$

[1]The r superscript in $\Sigma^r_0(\omega)$ stands for the retarded counterpart of the embedding self-energy.

[67].

Let us proceed with the EOM standard steps. Instead of discarding all terms as in Eq. (2.20) we make a Hartree-Fock approximation [67], namely,

$$\Lambda^{(2)}_{1,\mathbf{k}\alpha}(\omega) \simeq \langle n_{\bar{\sigma}}\rangle \Lambda_{\mathbf{k}\alpha\sigma}(\omega) \ , \tag{2.24}$$

and set $\Lambda^{(2)}_{2,\mathbf{k}\alpha}(\omega) = \Lambda^{(2)}_{3,\mathbf{k}\alpha}(\omega) = 0$. In other words, in this approximation we are retaining only processes in which the electrons hop in and out of the quantum dot and discarding more complex ones, which involves particle-hole excitations (scattering at the levels ε_0 and $\varepsilon_0 + U$). Substituting these results in Eqs. (2.18) and (2.16) one obtains

$$G_\sigma(\omega) = \frac{\omega - \varepsilon_0 - U(1 - \langle n_{\bar{\sigma}}\rangle)}{(\omega - \varepsilon_\sigma)(\omega - \varepsilon_0 - U) - \Sigma_0(\omega)[\omega - \varepsilon_0 - U(1 - \langle n_{\bar{\sigma}}\rangle)]} \ . \tag{2.25}$$

The above Green's function can be approximated by [67]

$$G_\sigma(\omega) \simeq \frac{1 - \langle n_{\bar{\sigma}}\rangle}{\omega - \varepsilon_0 - \Sigma_0(\omega)} + \frac{\langle n_{\bar{\sigma}}\rangle}{\omega - \varepsilon_0 - U - \Sigma_0(\omega)} \ , \tag{2.26}$$

which explicitly shows that the two resonances are now broadened and shifted by the non-interacting tunneling (or embedding) self-energy $\Sigma_0(\omega)$. This result is identical to the procedure discussed above of adding Σ_0 by hand to G_σ in Eq. (2.21). It is worth to mention that in the strongly correlated systems community the steps to obtain this result are formally equivalent to what is known as the Hubbard I approximation [29, 69]. The obvious difference is the embedding self-energy Σ_0 due to the coupling of the dot to the leads. Eqs. (2.25) and (2.26) are expected to be accurate in the perturbative or weak coupling limit, such as in the Coulomb blockade regime

The next hierarchical level of complexity is to write the EOM's for the correlation functions in Eq.(2.19), namely,

$$\begin{aligned}
(\omega - \varepsilon_{\mathbf{k}\alpha})\Lambda^{(2)}_{1,\mathbf{k}\alpha}(\omega) =& V_{\mathbf{k}\alpha} G^{(2)}(\omega) + \\
&+ \sum_{\mathbf{q}\beta} \big[- V_{\mathbf{q}\beta}\Lambda^{(3)}_{1,\mathbf{k}\alpha\mathbf{q}\beta}(\omega) + V^*_{\mathbf{q}\beta}\Lambda^{(3)}_{2,\mathbf{k}\alpha\mathbf{q}\beta}(\omega)\big] \ , \\
(\omega + \varepsilon_{\mathbf{k}\alpha} - \varepsilon_\sigma - \varepsilon_{\bar{\sigma}} - U)\Lambda^{(2)}_{2,\mathbf{k}\alpha}(\omega) =& V^*_{\mathbf{k}\alpha} G^{(2)}(\omega) + \\
&+ \sum_{\mathbf{q}\beta} V^*_{\mathbf{q}\beta}\big[\Lambda^{(3)}_{3,\mathbf{k}\alpha\mathbf{q}\beta}(\omega) + \Lambda^{(3)}_{4,\mathbf{k}\alpha\mathbf{q}\beta}(\omega)\big] \ , \\
(\omega - \varepsilon_{\mathbf{k}\alpha} + \varepsilon_{\bar{\sigma}} - \varepsilon_\sigma)\Lambda^{(2)}_{3,\mathbf{k}\alpha}(\omega) =& V^*_{\mathbf{k}\alpha}[G_\sigma(\omega) - G^{(2)}(\omega)] + \\
&+ \sum_{\mathbf{q}\beta} \big[- V_{\mathbf{q}\beta}\Lambda^{(3)}_{5,\mathbf{k}\alpha\mathbf{q}\beta}(\omega) + V^*_{\mathbf{q}\beta}\Lambda^{(3)}_{6,\mathbf{k}\alpha\mathbf{q}\beta}(\omega)\big] \ ,
\end{aligned} \tag{2.27}$$

where the new correlation functions $\Lambda^{(3)}_{i,\mathbf{k}\alpha\mathbf{q}\beta}$ are defined by

$$\begin{aligned}
\Lambda^{(3)}_{1,\mathbf{k}\alpha\mathbf{q}\beta}(t-t') &= -i\langle T\{c_{\mathbf{k}\alpha\sigma}(t)c^{\dagger}_{\mathbf{q}\beta\bar{\sigma}}(t)f_{\bar{\sigma}}(t)f^{\dagger}_{\sigma}(t')\}\rangle \ , \\
\Lambda^{(3)}_{2,\mathbf{k}\alpha\mathbf{q}\beta}(t-t') &= -i\langle T\{c_{\mathbf{k}\alpha\sigma}(t)f^{\dagger}_{\sigma}(t)c_{\mathbf{q}\beta\bar{\sigma}}(t)f^{\dagger}_{\sigma}(t')\}\rangle \ , \\
\Lambda^{(3)}_{3,\mathbf{k}\alpha\mathbf{q}\beta}(t-t') &= -i\langle T\{c^{\dagger}_{\mathbf{k}\alpha\bar{\sigma}}(t)c_{\mathbf{q}\beta\sigma}(t)f_{\bar{\sigma}}(t)f^{\dagger}_{\sigma}(t')\}\rangle \ , \\
\Lambda^{(3)}_{4,\mathbf{k}\alpha\mathbf{q}\beta}(t-t') &= -i\langle T\{c^{\dagger}_{\mathbf{k}\alpha\bar{\sigma}}(t)f_{\sigma}(t)c_{\mathbf{q}\beta\bar{\sigma}}(t)f^{\dagger}_{\sigma}(t')\}\rangle \ , \\
\Lambda^{(3)}_{5,\mathbf{k}\alpha\mathbf{q}\beta}(t-t') &= -i\langle T\{c_{\mathbf{k}\alpha\bar{\sigma}}(t)c^{\dagger}_{\mathbf{q}\beta\bar{\sigma}}(t)f_{\sigma}(t)f^{\dagger}_{\sigma}(t')\}\rangle \ , \\
\Lambda^{(3)}_{6,\mathbf{k}\alpha\mathbf{q}\beta}(t-t') &= -i\langle T\{c_{\mathbf{k}\alpha\bar{\sigma}}(t)f^{\dagger}_{\bar{\sigma}}(t)c_{\mathbf{q}\beta\sigma}(t)f^{\dagger}_{\sigma}(t')\}\rangle \ .
\end{aligned} \tag{2.28}$$

The correlation functions $\Lambda^{(3)}$, as the $\Lambda^{(2)}$ ones, involve 4 creation and annihilation operators and reflect the complex spin correlations that develop in the system due to the lead-quantum dot tunneling terms. As in the previous hierarchy level, one can apply some physical truncation scheme/approximation to the $\Lambda^{(3)}$ correlation functions to close the equations of motion.

Let us discuss the approximation used in Ref. [46]. For the sake of convenience we call this approach EOM1. The truncation consists of discarding correlations in which unlike lead spin-indices appear, that is

$$\Lambda^{(3)}_{1} = \Lambda^{(3)}_{2} = \Lambda^{(3)}_{3} = \Lambda^{(3)}_{6} = 0 \ , \tag{2.29}$$

The remaining correlation functions are approximated as follows

$$\begin{aligned}
\Lambda^{(3)}_{4,\mathbf{k}\alpha\mathbf{q}\beta}(\omega) &\approx -\delta_{\mathbf{k}\alpha\mathbf{q}\beta}f(\varepsilon_{\mathbf{k}\alpha})G_{\sigma}(\omega) \ , \\
\Lambda^{(3)}_{5,\mathbf{k}\alpha\mathbf{q}\beta}(\omega) &\approx -\delta_{\mathbf{k}\alpha\mathbf{q}\beta}[1-f(\varepsilon_{\mathbf{k}\alpha})]G_{\sigma}(\omega) \ ,
\end{aligned} \tag{2.30}$$

where $f(\varepsilon_{\mathbf{k}\alpha})$ is the equilibrium occupation of lead α. We stress that by neglecting spin correlations, this approximations - by construction - is incapable to describe he Kondo regime.

The quantum dot Green's function in the EOM1 approximation is given by [46] (we refer the reader to the section 12.11 of Ref. [67] for a detailed derivation):

$$G_{\sigma}(\omega) = \frac{\omega - \varepsilon_0 - U(1-\langle n_{\bar{\sigma}}\rangle) - \Sigma_0(\omega) - \Sigma_3(\omega)}{[\omega - \varepsilon_0 - \Sigma_0(\omega)][\omega - \varepsilon_0 - U - \Sigma_0(\omega) - \Sigma_3(\omega)] + U\Sigma_1(\omega)} \tag{2.31}$$

where the self-energies $\Sigma_{1,3}$ are written as [2]

$$\Sigma_i(\omega) = \sum_{\mathbf{q}\beta} A^{(i)}_{\mathbf{q}\beta} |V_{\mathbf{q}\beta}|^2 \left[\frac{1}{\omega + \varepsilon_{\mathbf{q}\beta} - 2\varepsilon_0 - U} + \frac{1}{\omega - \varepsilon_{\mathbf{q}\beta}} \right] \tag{2.32}$$

with $A^{(1)}_{\mathbf{q}\beta} = f(\varepsilon_{\mathbf{q}\beta})$ and $A^{(3)}_{\mathbf{q}\beta} = 1$.

One can proceed analytically by simplifying the integral in Eq. (2.32) using the wide band approximation. In this way, we assume that the leads have a constant electronic density of states (DOS), ρ_α, which allows us to use the Sokhotski–Plemelj theorem,

$$\lim_{\eta \to 0^+} \int_a^b \frac{f(\varepsilon)}{\varepsilon - (\varepsilon_0 \pm i\eta)} d\varepsilon = \pm i\pi f(\varepsilon_0) + \mathcal{P} \int_a^b \frac{f(\varepsilon)}{\varepsilon - \varepsilon_0} d\varepsilon \ , \tag{2.33}$$

where $\mathcal{P}$ stands for the Cauchy principal value. Hence we obtain the self-energies

$$\begin{aligned} \Sigma_1(\omega) &= \frac{\Gamma}{2\pi} \left[-\Psi\left(\frac{1}{2} + \frac{\omega}{2\pi T i} \right) + \Psi\left(\frac{1}{2} + \frac{\omega - 2\varepsilon_0 - U}{2\pi T i} \right) + \ln \left| \frac{D + \omega}{D - \omega + 2\varepsilon_0 + U} \right| - i\pi \right] \\ \Sigma_3(\omega) &= \frac{\Gamma}{2\pi} \ln \left| \frac{D + \omega}{D - \omega + 2\varepsilon_0 + U} \right| - i\Gamma \ , \end{aligned} \tag{2.34}$$

where $\Gamma \equiv 2\pi \sum_\alpha |V_{\mathbf{k}\alpha}|^2 \rho_\alpha$ is the system line width, assumed to be constant inside the band width, namely $-D \leq \varepsilon_{\mathbf{k}\alpha} \leq D$, and Ψ is the digamma function . In order to make the double peak structure of this Green's function more explicit we write

$$\begin{aligned} G_\sigma(\omega) = &\frac{1 - \langle n_{\bar{\sigma}} \rangle}{\omega - \varepsilon_0 - \Sigma_0(\omega) + U\Sigma_1(\omega)[\omega - \varepsilon_0 - U - \Sigma_0(\omega) - \Sigma_3(\omega)]^{-1}} \\ &+ \frac{\langle n_{\bar{\sigma}} \rangle}{\omega - \varepsilon_0 - U - \Sigma_0(\omega) - U\Sigma_2(\omega)[\omega - \varepsilon_0 - \Sigma_0(\omega) - \Sigma_3(\omega)]^{-1}} \ , \end{aligned} \tag{2.35}$$

where Σ_2 is given by Eq. (2.32) with $A^{(2)}_{\mathbf{q}\beta} = 1 - f(\varepsilon_{\mathbf{q}\beta})$. Note that the Green's function depends on the temperature not only through $\langle n_{\bar{\sigma}} \rangle$ but also through the self-energies $\Sigma_1(\omega)$ and $\Sigma_2(\omega)$. This approximation scheme is well-known in the semiconductor quantum dots literature due to the seminal works of Meir, Wingreen, and Lee [46]. The self-energies $\Sigma_{i>0}(\omega)$ entail many-body effects, but no spin correlations. Their derivation is formally equivalent to the Hubbard III approximation [29, 70, 71].

For notational convenience, let us write the correlation functions and the EOM's in the Zubarev notation [72]. In this notation a general Green's function reads

$$\langle\langle X; Y \rangle\rangle_{\omega \pm i\eta} \equiv \mp i \int_{-\infty}^{+\infty} \theta(\pm t) \langle \{X(t); Y\} \rangle e^{i(\omega \pm i\eta)t} dt \ , \tag{2.36}$$

[2] In Eq. (2.32) we correct the typos of the corresponding equation in Ref. [67].

where X and Y are operators, θ is the Heaviside step function, and $\eta \to 0^+$. For instance, the Green's function reads

$$G_\sigma(z) \equiv \langle\langle f_\sigma; f_\sigma^\dagger \rangle\rangle_z \ , \quad z = \omega + i\eta \tag{2.37}$$

The Fourier transform of the EOM for the Green's function defined by Eq. (2.36) satisfies

$$\begin{aligned} z\langle\langle X; Y \rangle\rangle_z &= \langle\{X; Y\}\rangle + \langle\langle [X, H]; Y \rangle\rangle_z \\ &= \langle\{X; Y\}\rangle - \langle\langle X; [Y, H] \rangle\rangle_z \ . \end{aligned} \tag{2.38}$$

The thermal average $\langle XY \rangle$ is given by

$$\langle XY \rangle = i \oint_C \frac{dz}{2\pi} f(z) \langle\langle Y; X \rangle\rangle_z, \quad f(z) \equiv \frac{1}{1 + e^{z/T}} \ , \tag{2.39}$$

where C is a contour which runs clockwise around the real axis. In this way, one can work directly in the energy representation, avoiding the need of deriving the EOM's in time domain (which is not necessary for stationary processes).

The correlation functions $\Lambda^{(3)}$ are now written as

$$\begin{aligned} \Lambda^{(3)}_{1,\mathbf{k}\alpha\mathbf{q}\beta}(z) &= \langle\langle c_{\mathbf{k}\alpha\sigma} c^\dagger_{\mathbf{q}\beta\bar{\sigma}} f_{\bar{\sigma}}; f^\dagger_\sigma \rangle\rangle_z \ , \\ \Lambda^{(3)}_{2,\mathbf{k}\alpha\mathbf{q}\beta}(z) &= \langle\langle c_{\mathbf{k}\alpha\sigma} f^\dagger_\sigma c_{\mathbf{q}\beta\bar{\sigma}}; f^\dagger_\sigma \rangle\rangle_z \ , \\ \Lambda^{(3)}_{3,\mathbf{k}\alpha\mathbf{q}\beta}(z) &= \langle\langle c^\dagger_{\mathbf{k}\alpha\bar{\sigma}} c_{\mathbf{q}\beta\sigma} f_{\bar{\sigma}}; f^\dagger_\sigma \rangle\rangle_z \ , \\ \Lambda^{(3)}_{4,\mathbf{k}\alpha\mathbf{q}\beta}(z) &= \langle\langle c^\dagger_{\mathbf{k}\alpha\bar{\sigma}} f_\sigma c_{\mathbf{q}\beta\bar{\sigma}}; f^\dagger_\sigma \rangle\rangle_z \ , \\ \Lambda^{(3)}_{5,\mathbf{k}\alpha\mathbf{q}\beta}(z) &= \langle\langle c_{\mathbf{k}\alpha\bar{\sigma}} c^\dagger_{\mathbf{q}\beta\bar{\sigma}} f_\sigma; f^\dagger_\sigma \rangle\rangle_z \ , \\ \Lambda^{(3)}_{6,\mathbf{k}\alpha\mathbf{q}\beta}(z) &= \langle\langle c_{\mathbf{k}\alpha\bar{\sigma}} f^\dagger_{\bar{\sigma}} c_{\mathbf{q}\beta\sigma}; f^\dagger_\sigma \rangle\rangle_z \ . \end{aligned} \tag{2.40}$$

Let us now discuss another truncation scheme put forward in Refs. [73, 74]. The author decouples the correlation functions in Eq. (2.40) as

$$\begin{aligned} \langle\langle c_{\mathbf{k}\alpha\sigma} c^\dagger_{\mathbf{q}\beta\bar{\sigma}} f_{\bar{\sigma}}; f^\dagger_\sigma \rangle\rangle_z &\simeq \langle c^\dagger_{\mathbf{q}\beta\bar{\sigma}} f_{\bar{\sigma}} \rangle \langle\langle c_{\mathbf{k}\alpha\sigma}; f^\dagger_\sigma \rangle\rangle_z \ , \\ \langle\langle c_{\mathbf{k}\alpha\sigma} f^\dagger_{\bar{\sigma}} c_{\mathbf{q}\beta\bar{\sigma}}; f^\dagger_\sigma \rangle\rangle_z &\simeq -\langle f^\dagger_{\bar{\sigma}} c_{\mathbf{q}\beta\bar{\sigma}} \rangle \langle\langle c_{\mathbf{k}\alpha\sigma}; f^\dagger_\sigma \rangle\rangle_z \qquad z \equiv \omega + i\eta \ , \\ \langle\langle c^\dagger_{\mathbf{k}\alpha\bar{\sigma}} f_\sigma c_{\mathbf{q}\beta\bar{\sigma}}; f^\dagger_\sigma \rangle\rangle_z &\simeq \langle c^\dagger_{\mathbf{k}\alpha\bar{\sigma}} c_{\mathbf{q}\beta\bar{\sigma}} \rangle \langle\langle f_\sigma; f^\dagger_\sigma \rangle\rangle_z \ . \end{aligned} \tag{2.41}$$

The explicit derivation can be found, for instance, in Refs. [73, 74]. Here, for the sake of completeness, we present only the main results.

Let us consider the simple case where one can assume a constant density of states for the conduction electrons, $\rho(\omega) = 1/(2D)$, with $-D < \omega < D$, and a constant coupling matrix $V_{\mathbf{k}\alpha} = V$. It is straightforward to show that the dot Green's function reads

$$G_\sigma(\omega) = \frac{1 + \frac{U}{\omega - \varepsilon_0 - U + i\Delta}\big[\langle n_{\bar\sigma}\rangle + A(\omega)\big]}{\omega - \varepsilon_0 + i\Delta - \frac{U}{\omega - \varepsilon_0 - U + i\Delta}B(\omega) - i\Delta A(\omega)} \ , \tag{2.42}$$

where $\Delta = \pi V^2/2D = -\mathrm{Im}\Sigma_0^r \equiv \Gamma/2$, and

$$\begin{aligned} A(\omega) &= V\sum_{\mathbf{k}} \langle d_{\bar\sigma}^\dagger c_{\mathbf{q}\beta\bar\sigma}\rangle \Big(\frac{1}{\omega - \varepsilon_{\mathbf{k}}} + \frac{1}{2\varepsilon_0 + U - \omega - \varepsilon_{\mathbf{k}}}\Big) \ , \\ B(\omega) &= -V^2\sum_{\mathbf{kq}} \langle c_{\mathbf{q}\beta\bar\sigma}^\dagger c_{\mathbf{k}\alpha\bar\sigma}\rangle \Big(\frac{1}{\omega - \varepsilon_{\mathbf{k}}} - \frac{1}{2\varepsilon_0 + U - \omega - \varepsilon_{\mathbf{k}}}\Big) \ . \end{aligned} \tag{2.43}$$

Now we discuss the scheme used in Ref. [59], that we call EOM2. The basic idea consists of truncating the hierarchy of the EOM's by approximating the Green's functions of the form $\langle\langle X^\dagger Y Z; d^\dagger\rangle\rangle$ as decoupled products of two-operator Green's functions and thermal averages, namely,

$$\langle\langle X^\dagger Y Z; d^\dagger\rangle\rangle \cong \langle X^\dagger Y\rangle\langle\langle Z; d^\dagger\rangle\rangle - \langle X^\dagger Z\rangle\langle\langle Y; d^\dagger\rangle\rangle \ , \tag{2.44}$$

where at least two of the operators X,Y and Z correspond to bath (leads) electron operators, that is, belong to the $c_{\mathbf{k}\alpha\sigma}$ subspace. In the EOM2 approximation scheme the $\Lambda^{(3)}$ correlation functions are

$$\begin{aligned} &\langle\langle c_{\mathbf{k}\alpha\sigma} c_{\mathbf{q}\beta\bar\sigma}^\dagger f_{\bar\sigma}; f_\sigma^\dagger\rangle\rangle_z \simeq -\langle c_{\mathbf{q}\beta\bar\sigma}^\dagger c_{\mathbf{k}\alpha\sigma}\rangle\langle\langle f_{\bar\sigma}; f_\sigma^\dagger\rangle\rangle_z + \langle c_{\mathbf{q}\beta\bar\sigma}^\dagger f_{\bar\sigma}\rangle\langle\langle c_{\mathbf{k}\alpha\sigma}; f_\sigma^\dagger\rangle\rangle_z \ , \\ &\langle\langle c_{\mathbf{k}\alpha\sigma} f_{\bar\sigma}^\dagger c_{\mathbf{q}\beta\bar\sigma}; f_\sigma^\dagger\rangle\rangle_z \simeq \langle f_{\bar\sigma}^\dagger c_{\mathbf{k}\alpha\sigma}\rangle\langle\langle c_{\mathbf{q}\beta\bar\sigma}; f_\sigma^\dagger\rangle\rangle_z - \langle f_{\bar\sigma}^\dagger c_{\mathbf{q}\beta\bar\sigma}\rangle\langle\langle c_{\mathbf{k}\alpha\sigma}; f_\sigma^\dagger\rangle\rangle_z \ , \qquad z \equiv \omega + i\eta \\ &\langle\langle c_{\mathbf{k}\alpha\bar\sigma}^\dagger f_\sigma c_{\mathbf{q}\beta\bar\sigma}; f_\sigma^\dagger\rangle\rangle_z \simeq \langle c_{\mathbf{k}\alpha\bar\sigma}^\dagger f_\sigma\rangle\langle\langle c_{\mathbf{q}\beta\bar\sigma}; f_\sigma^\dagger\rangle\rangle_z - \langle c_{\mathbf{k}\alpha\bar\sigma}^\dagger c_{\mathbf{q}\beta\bar\sigma}\rangle\langle\langle f_\sigma; f_\sigma^\dagger\rangle\rangle_z \ . \end{aligned} \tag{2.45}$$

The explicit dot Green's function in the EOM2 approximation in the absence of external magnetic field is given by [59]

$$G_\sigma(z) = \frac{u(z) - \langle n_{\bar\sigma}\rangle - P_{\bar\sigma}(z) - P_{\bar\sigma}(z_2)}{u(z)[z - \varepsilon_0 - \Sigma_0(z)] + [P_{\bar\sigma}(z) + P_{\bar\sigma}(z_2)]\Sigma_0(z) - Q_{\bar\sigma}(z) + Q_{\bar\sigma}(z_2)} \ , \tag{2.46}$$

where

$$u(z) \equiv U^{-1}[U - z + \varepsilon_0 + 2\Sigma_0(z) - \Sigma_0(z_2)] \ , \tag{2.47}$$

$\Sigma_0(z)$ is the noninteracting self-energy of the dot, Eq. (2.17), generalized to the complex

plane, and $z_2 = -z + 2\varepsilon_0 + U$. The functions $P_\sigma(z)$ and $Q_\sigma(z)$ are given by

$$\begin{aligned} P_\sigma(z) \equiv & \frac{i}{2\pi}\oint_C f(w)G_\sigma(w)\frac{\Sigma_0(w)-\Sigma_0(z)}{z-w}dw \\ Q_\sigma(z) \equiv & \frac{i}{2\pi}\oint_C f(w)[1+\Sigma_0(w)G_\sigma(w)]\frac{\Sigma_0(w)-\Sigma_0(z)}{z-w}dw\,. \end{aligned} \tag{2.48}$$

To find $G_\sigma(z)$ we must solve Eqs. (2.46), (2.48), and (2.23) self-consistently. One can show that, in the particle-hole symmetric case, Eq. (2.46) reduces to a very simple form [59], namely,

$$[G_\sigma(\omega)]^{-1} = \omega - \Sigma_0(\omega) - \frac{U^2}{4[\omega - 3\Sigma_0(\omega)]}\ . \tag{2.49}$$

It is also straightforward to show that the EOM1 Green's function, Eq. (2.31), coincides with Eq. (2.49), in the symmetric case of the SIAM, see Appendix A.

The retarded and advanced counterparts of the functions above are obtained by making the substitution $z \to \omega \pm i\eta$, namely,

$$\begin{aligned} G_\sigma^{r(a)}(\omega) &= G(\omega \pm i\eta)\ , \\ \Sigma_0^{r(a)}(\omega) &= \Sigma_0(\omega \pm i\eta)\ , \\ P_\sigma^{r(a)}(\omega) &= P(\omega \pm i\eta)\ , \\ Q_\sigma^{r(a)}(\omega) &= Q(\omega \pm i\eta)\ , \end{aligned} \tag{2.50}$$

with $\eta \to 0^+$.

In order to numerically implement the EOM2 scheme and self-consistently solve the above equations, it is convenient to rewrite Eq. (2.48) as

$$\begin{aligned} P(z) = & -\frac{1}{\pi}\Bigg\{\mathcal{P}\int_{-\infty}^{\infty} d\varepsilon \frac{f(\varepsilon)}{\omega-\varepsilon}\mathrm{Im}[G_\sigma^r(\varepsilon)\Sigma_0^r(\varepsilon)] - i\pi f(\omega)\mathrm{Im}[G_\sigma^r(\omega)\Sigma_0^r(\omega)] - \\ & - \Sigma_0(z)\left[\mathcal{P}\int_{-\infty}^{\infty} d\varepsilon \frac{f(\varepsilon)}{\omega-\varepsilon}\mathrm{Im}[G_\sigma^r(\varepsilon)] - i\pi f(\omega)\mathrm{Im}[G_\sigma^r(\omega)]\right]\Bigg\}\ , \end{aligned} \tag{2.51}$$

$$\begin{aligned} Q(z) = & -\frac{1}{\pi}\Bigg\{\mathcal{P}\int_{-\infty}^{\infty} d\varepsilon \frac{f(\varepsilon)}{\omega-\varepsilon}\mathrm{Im}[\Sigma_0^r(\varepsilon)] - i\pi f(\omega)\mathrm{Im}[\Sigma_0^r(\omega)] + \\ & + \mathcal{P}\int_{-\infty}^{\infty} d\varepsilon \frac{f(\varepsilon)}{\omega-\varepsilon}\mathrm{Im}[G^r(\varepsilon)(\Sigma_0^r(\varepsilon))^2] - i\pi f(\omega)\mathrm{Im}[G^r(\omega)(\Sigma_0^r(\omega))^2] \\ & - \Sigma_0(z)\mathcal{P}\int_{-\infty}^{\infty} d\varepsilon \frac{f(\varepsilon)}{\omega-\varepsilon}\mathrm{Im}[G^r(\varepsilon)\Sigma_0^r(\varepsilon)] + i\pi\Sigma_0(z)f(\omega)\mathrm{Im}[G^r(\omega)\Sigma_0^r(\omega)]\Bigg\}\ . \end{aligned} \tag{2.52}$$

It is also useful to calculate these expressions using the asymptotic behavior in the $|\omega| \to \infty$ limit. In addition to be computationally faster it also helps to deal with functions with

shifted arguments. This is the case, for instance, of the function $P(z_2) = P(-z+2\varepsilon_0+U)$ appearing in Eq. (2.46). In order to avoid problems with array allocation, especially at its boundaries, we use the expressions obtained in the following for the asymptotic behavior to represent the tails ($|\omega| \to \infty$) of the principal value integrals in Eqs. (2.51) and (2.52).

One can expand the Cauchy principal integral in inverse powers of ω as follows

$$\mathcal{P}\int_{-D}^{D} d\varepsilon \frac{g(\varepsilon)}{\omega-\varepsilon} \approx \frac{1}{\omega}\int d\varepsilon \Big(1+\frac{\varepsilon}{\omega}\Big) g(\varepsilon) \cong \frac{C_1}{\omega} + \frac{C_2}{\omega^2} \ , \tag{2.53}$$

where $\omega \notin [-D, D]$. Hence, one can write

$$P^r(\omega) \cong -\frac{1}{\pi}\Big(\frac{C_1}{\omega} + \frac{C_2}{\omega^2}\Big) + \frac{1}{\pi}\Sigma_0^r(\omega)\Big(\frac{C_1'}{\omega} + \frac{C_2'}{\omega^2}\Big) \ , \tag{2.54}$$

where,

$$\begin{aligned} C_1 &= \int d\varepsilon \ f(\varepsilon)\mathrm{Im}[G^r(\varepsilon)\Sigma_0^r(\varepsilon)] \ , \\ C_2 &= \int d\varepsilon \ \varepsilon f(\varepsilon)\mathrm{Im}[G^r(\varepsilon)\Sigma_0^r(\varepsilon)] \ , \\ C_1' &= \int d\varepsilon \ f(\varepsilon)\mathrm{Im}[G^r(\varepsilon)] = \langle n_\sigma \rangle \ , \\ C_2' &= \int d\varepsilon \ \varepsilon f(\varepsilon)\mathrm{Im}[G^r(\varepsilon)] \ . \end{aligned} \tag{2.55}$$

Analogously for the function Q one can write

$$Q^r(\omega) \sim -\frac{1}{\pi}\Big(\frac{C_3}{\omega} + \frac{C_4}{\omega^2}\Big) + \frac{1}{\pi}\Sigma_0^r(\omega)\Big(\frac{C_3'}{\omega} + \frac{C_4'}{\omega^2}\Big) \ , \tag{2.56}$$

where,

$$\begin{aligned} C_3 &= \int d\varepsilon \ f(\varepsilon)\mathrm{Im}[\Sigma_0^r(\varepsilon)(1+\Sigma_0^r(\varepsilon)G^r(\varepsilon))] \ , \\ C_4 &= \int d\varepsilon \ \varepsilon f(\varepsilon)\mathrm{Im}[\Sigma_0^r(\varepsilon)(1+\Sigma_0^r(\varepsilon)G^r(\varepsilon))] \ , \\ C_3' &= \int d\varepsilon \ f(\varepsilon)\mathrm{Im}[G^r(\varepsilon)\Sigma_0^r(\varepsilon)] = C_1 \ , \\ C_4' &= \int d\varepsilon \ \varepsilon f(\varepsilon)\mathrm{Im}[G^r(\varepsilon)\Sigma_0^r(\varepsilon)] = C_2 \ . \end{aligned} \tag{2.57}$$

2.2 Slave boson methods: non crossing and one crossing approximations

Slave boson methods were introduced in the context of experimental investigations in compounds with rare-earth elements in the lates 70's and early 80's [7]. In compounds like the SmB_6, for example, the f states lie near the Fermi level and hybridizes weakly with the band of free electrons giving rise to the so-called *mixed* (or *intermediate*) *valence* regime [10,11,75]. In order to address this regime it is convenient to represent the spinless valence state of the localized level by a slave-boson while the spinning state is represented by a pseudofermion. The method was applied to the Anderson impurity model and also extended to lattice models like the Hubbard model. Using the pseudo-particle representation for the operators appearing in the used model a mean field theory was developed in the large U limit by considering an expansion on the hybridization and taking the limit of large degeneracy N of the localized level [7, 11, 29, 75–77]. This technique was applied to study heavy fermion systems [78, 79] and high-Tc superconductors [80, 81].

Let us now review a slightly more sophisticated slave boson based approach for the finite-U SIAM developed at about the same time. In most contexts, considering the interaction part of the model as a perturbation is problematic since U is one of the largest energy scales of the system. Alternatively, noting that the hybridization terms are small compared to U and the kinetic part of the Hamiltonian [60], one can treat them as the perturbation term of the problem.

We begin recalling that in the proposed scheme the SIAM Hamiltonian,

$$H = \sum_{\substack{\mathbf{k}\sigma \\ \alpha\in L,R}} \varepsilon_{\mathbf{k}\alpha} c^\dagger_{\mathbf{k}\alpha\sigma} c_{\mathbf{k}\alpha\sigma} + \sum_\sigma \varepsilon_0 f^\dagger_\sigma f_\sigma + U n_\uparrow n_\downarrow + \sum_{\substack{\mathbf{k}\sigma \\ \alpha\in L,R}} \left(V_{\mathbf{k}\alpha} f^\dagger_\sigma c_{\mathbf{k}\alpha\sigma} + \text{H.c.} \right) , \tag{2.58}$$

entails an unperturbed term,

$$H_0 = \sum_{\substack{\mathbf{k}\sigma \\ \alpha\in L,R}} \varepsilon_{\mathbf{k}\alpha} c^\dagger_{\mathbf{k}\alpha\sigma} c_{\mathbf{k}\alpha\sigma} + \sum_\sigma \varepsilon_0 f^\dagger_\sigma f_\sigma + U n_\uparrow n_\downarrow , \tag{2.59}$$

that is not bilinear. In this case one cannot use the standard perturbation theory since Wick's theorem does not apply.

However it is possible to circumvent this problem by employing another representation for the impurity operators, namely [61, 82, 83]:

$$f^\dagger_\sigma = s^\dagger_\sigma b + d^\dagger_{\bar\sigma\sigma} s_{\bar\sigma} , \tag{2.60}$$

where $b^\dagger$, $s^\dagger_\sigma$ and $d^\dagger_{\bar\sigma\sigma}$ are auxiliary (pseudo-particle) operators which operating on the vacuum state $|vac\rangle$, create the states $|0\rangle$, $|\sigma\rangle$ and $|\bar\sigma\sigma\rangle$, respectively. $b^\dagger$ and $d^\dagger_{\bar\sigma\sigma}$ are bosonic operators, while $s^\dagger_\sigma$ is a fermionic operator. This representation contains some unphysical states which can be eliminated by imposing that [84]

$$f^\dagger_\sigma f_\sigma = s^\dagger_\sigma s_\sigma + d^\dagger_{\bar\sigma\sigma} d_{\bar\sigma\sigma} \tag{2.61}$$

which represents the two ways of counting the number of fermions with a given spin. Now, the subspace of impurity states is formed by the four states $|0\rangle$, $|\uparrow\rangle$, $|\downarrow\rangle$ and $|\uparrow\downarrow\rangle$ representing an empty, single-occupied with spin up, single-occupied with spin down, and double occupied impurity states, respectively [3]. This implies that, at any time, we must have [53, 85–87]

$$Q \equiv b^\dagger b + \sum_\sigma s^\dagger_\sigma s_\sigma + d^\dagger_{\bar\sigma\sigma} d_{\bar\sigma\sigma} = 1 \ , \tag{2.62}$$

where Q the pseudo-particle charge.

After employing the slave-boson representation with the constraints given by Eqs. (2.61) and (2.62) the SIAM reads [61]

$$\begin{aligned} H = & \sum_{\substack{\mathbf{k}\sigma \\ \alpha\in L,R}} \varepsilon_{\mathbf{k}\alpha} c^\dagger_{\mathbf{k}\alpha\sigma} c_{\mathbf{k}\alpha\sigma} + \sum_\sigma \varepsilon_0 s^\dagger_\sigma s_\sigma + (2\varepsilon_0 + U) d^\dagger_{\bar\sigma\sigma} d_{\bar\sigma\sigma} + \\ & + \sum_{\substack{\mathbf{k}\sigma \\ \alpha\in L,R}} \left(V_{\mathbf{k}\alpha} s^\dagger_\sigma b \, c_{\mathbf{k}\alpha\sigma} + \text{H.c.} \right) + \sum_{\substack{\mathbf{k}\sigma \\ \alpha\in L,R}} \left(V_{\mathbf{k}\alpha} d^\dagger_{\bar\sigma\sigma} s_{\bar\sigma} c_{\mathbf{k}\alpha\sigma} + \text{H.c.} \right) \ , \end{aligned} \tag{2.63}$$

and H_0 is bilinear.

The constraint in Eq. (2.62) must be taken into account when calculating averages of operators, $\langle O\rangle$, using Hamiltonian of Eq. (2.63). This is done as follows: First, one calculates $\langle O\rangle_G$ in the grand canonical ensemble where Q is unrestricted. We recall that there are well established diagrammatic techniques to evaluate $\langle O\rangle_G$ [66, 88]. Next one projects $\langle O\rangle_G$ onto the $Q = 1$ subspace to find the projected expectation value, $\langle O\rangle_C$, in the canonical ensemble [7, 11, 65, 85, 89]. In the grand canonical ensemble, a chemical potential $-\lambda$ is associated with the pseudo-particle charge, Q. The density matrix reads

$$\rho_G = \frac{1}{Z_G} e^{-\beta(H+\lambda Q)} \ , \tag{2.64}$$

[3] In Ref. [75] a very enlightening notation is used for the impurity states in the slave boson representation. In this notation one has $|0\rangle = |b^1 s^0_\uparrow s^0_\downarrow d^0_{\uparrow\downarrow}\rangle$, $|\uparrow\rangle = |b^0 s^1_\uparrow s^0_\downarrow d^0_{\uparrow\downarrow}\rangle$, $|\downarrow\rangle = |b^0 s^0_\uparrow s^1_\downarrow d^0_{\uparrow\downarrow}\rangle$, and $|\uparrow\downarrow\rangle = |b^0 s^0_\uparrow s^0_\downarrow d^1_{\uparrow\downarrow}\rangle$.

while the partition function is given by

$$Z_G = \mathrm{Tr}[e^{-\beta(H+\lambda Q)}] = \sum_{Q=0}^{\infty} Z_C(Q)\zeta^Q \ , \tag{2.65}$$

where $Z_C(Q)$ is the canonical partition function for a given Q, and $\zeta = e^{-\beta\lambda}$ is the fugacity.

Let us consider two expectation values, namely,

$$\langle OQ\rangle_G = \mathrm{Tr}[\rho_G OQ] = \frac{1}{Z_G}\sum_{Q=0}^{\infty} \mathrm{Tr}[Oe^{-\beta H}]_{F_Q} Q e^{-\beta\lambda Q} \ , \tag{2.66}$$

where O is an arbitrary operator and the expectation value of the pseudo-particle charge, $\langle Q\rangle_G$,

$$\langle Q\rangle_G = \mathrm{Tr}[\rho_G Q] = \frac{1}{Z_G}\sum_{Q=0}^{\infty} \mathrm{Tr}[Qe^{-\beta H}]_{F_Q} e^{-\beta\lambda Q} \ . \tag{2.67}$$

In the expressions above F_Q denotes the subspace in which the pseudo-particle charge is Q. One can show that the projected expectation value of an arbitrary operator is given by the ratio between the two quantities introduced above [11, 89–92]

$$\langle O\rangle_C = \frac{\mathrm{Tr}[Oe^{-\beta H}]_{F_1}}{Z_C(1)} = \lim_{\lambda\to\infty}\frac{\langle OQ\rangle_G}{\langle Q\rangle_G} \tag{2.68}$$

Let us now obtain the canonical partition function in the subspace $Q = 1$, that is, $Z_C(1)$. For that purpose we use that by differentiating Z_G, Eq. (2.65), with respect to the fugacity gives

$$\frac{\partial Z_G}{\partial\zeta} = \sum_{Q=1}^{\infty} Q\zeta^{Q-1} Z_C(Q) = \sum_{Q=1}^{\infty} Q Z_C(Q) e^{-\beta\lambda(Q-1)} \ . \tag{2.69}$$

By taking the limit $\lambda\to\infty$, the only term in the sum of the r.h.s. that survives is $Q = 1$, rendering the identity

$$\lim_{\lambda\to\infty}\frac{\partial Z_G}{\partial\zeta} = Z_C(1) \ . \tag{2.70}$$

Hence, one explicitly writes

$$Z_C(1) = \lim_{\lambda\to\infty}\frac{\partial Z_G}{\partial\zeta} = \lim_{\lambda\to\infty}\mathrm{Tr}[Qe^{-\beta(H+\lambda(Q-1))}] = \lim_{\lambda\to\infty} e^{\beta\lambda}\langle Q\rangle_G Z_G \ . \tag{2.71}$$

Since the fugacity ζ diverges exponentially with growing λ and $\lim_{\lambda\to\infty} Z_G = Z_C(0)$, the expectation value of the pseudoparticle number $\langle Q\rangle_G$ is expected to decay exponentially with $\lambda \gg 1$. Thus

$$Z_C(1) = \lim_{\lambda\to\infty}\left(e^{\beta\lambda}\langle Q\rangle_G\right) Z_C(0) \tag{2.72}$$

In most cases, the expectation value of a given operator O in the $Q = 0$ subspace is zero, $\langle O\rangle_C^{Q=0} = 0$. Local observables acting on the impurity like the physical electron creation operator $f_\sigma^\dagger$ or the local spin operator $S = \Sigma_{\sigma\sigma'}\frac{1}{2}f_\sigma^\dagger\tau_{\sigma\sigma'}f_\sigma^\dagger$ are such examples. This implies that, in the $\lambda \to \infty$ limit,

$$\langle OQ\rangle_G \to \langle O\rangle_G \tag{2.73}$$

Then Eq.(2.68) simplifies to [86, 90–92]

$$\langle O\rangle_C = \lim_{\lambda\to\infty}\frac{\langle O\rangle_G}{\langle Q\rangle_G} \ , \tag{2.74}$$

a key relation for the method.

Let us now return to the central object of interest and calculate the dot Green's function which, in the Matsubara formalism, is defined by [66, 88]

$$\mathcal{G}_\sigma(\tau) \equiv -\langle T_\tau\{f_\sigma(\tau)f_\sigma^\dagger(0)\}\rangle \ , \tag{2.75}$$

where τ is the imaginary time defined in the interval $-\beta < \tau < \beta$, $\beta = 1/k_BT$, and T_τ is the imaginary time ordering operator. One can write the dot Green function in terms of the grand-canonical pseudo-particle Green's functions, given by

$$\begin{aligned}
\mathcal{G}_b(\tau) &\equiv -\langle T_\tau\{b(\tau)b^\dagger(0)\}\rangle_G \\
\mathcal{G}_{s_\sigma}(\tau) &\equiv -\langle T_\tau\{s_\sigma(\tau)s_\sigma^\dagger(0)\}\rangle_G \\
\mathcal{G}_d(\tau) &\equiv -\langle T_\tau\{d_{\bar\sigma\sigma}(\tau)d_{\bar\sigma\sigma}^\dagger(0)\}\rangle_G
\end{aligned} \tag{2.76}$$

and, similarly, the expectation value of the pseudo-particle number

$$\langle Q\rangle_G = \int d\epsilon[b(\epsilon)\mathcal{A}_b(\epsilon) + f(\epsilon)\sum_\sigma \mathcal{A}_{s_\sigma}(\epsilon) + b(\epsilon)\mathcal{A}_d(\epsilon)] \tag{2.77}$$

where $f(\epsilon)$ and $b(\epsilon)$ are the Fermi and Bose distribution, respectively, and $\mathcal{A}_m(\epsilon) = -\mathrm{Im}[\mathcal{G}_m(\epsilon)]/\pi,\ m = b, s_\sigma, d$, are the unprojected pseudo-particle density of states.

The perturbation expansion of the pseudo-particle Green's functions is given by [66, 88]:

$$\mathcal{G}_m(\tau) = -\sum_{n=0}^{\infty}\frac{(-i)^n}{n!}\int_0^\beta d\tau_1\cdots\int_0^\beta d\tau_n \ \ {}_0\langle T_\tau a_m(\tau)a_m^\dagger(0)H_V(\tau_1)\cdots H_V(\tau_n)\rangle_0 \tag{2.78}$$

where $a_m = b, s_\sigma$ or d, and $\mathcal{H}_V$ reads

$$H_V = \sum_{\substack{\mathbf{k}\sigma \\ \alpha\in L,R}} \left(V_{\mathbf{k}\alpha} s_\sigma^\dagger b\, c_{\mathbf{k}\alpha\sigma} + \text{H.c.}\right) + \sum_{\substack{\mathbf{k}\sigma \\ \alpha\in L,R}} \left(V_{\mathbf{k}\alpha} d_{\bar{\sigma}\sigma}^\dagger s_{\bar{\sigma}} c_{\mathbf{k}\alpha\sigma} + \text{H.c.}\right) \tag{2.79}$$

Here ${}_0\langle\cdots\rangle_0$ means that we are performing, as standard, an statistical average over the eigenstates of the unperturbed Hamiltonian

$$H_0 = \sum_{\substack{\mathbf{k}\sigma \\ \alpha\in L,R}} \varepsilon_{\mathbf{k}\alpha} c_{\mathbf{k}\alpha\sigma}^\dagger c_{\mathbf{k}\alpha\sigma} + \sum_\sigma \varepsilon_0 s_\sigma^\dagger s_\sigma + (2\varepsilon_0 + U) d_{\bar{\sigma}\sigma}^\dagger d_{\bar{\sigma}\sigma}\ . \tag{2.80}$$

In frequency domain one writes the Matsubara Green's functions as

$$\begin{aligned}
\mathcal{G}_b(i\omega_n) &= [i\omega_n - \lambda - \Sigma_b(i\omega_n)]^{-1} \\
\mathcal{G}_{s_\sigma}(i\omega_n) &= [i\omega_n - \varepsilon_0 - \lambda - \Sigma_{s_\sigma}(i\omega_n)]^{-1} \\
\mathcal{G}_d(i\omega_n) &= [i\omega_n - 2\varepsilon_0 - U - \lambda - \Sigma_d(i\omega_n)]^{-1}
\end{aligned} \tag{2.81}$$

Note that the energy eigenvalues of the Hamiltonian $H + \lambda Q$ scale to infinite as λQ because of the projection procedure, where we take $\lambda \to \infty$. As a consequence, it is convenient to shift the energy scale of the pseudo-particle Green's functions by λ and to define the projected pseudo-particle Green's functions, assuming we are already in the real axis, by [90, 91]

$$G_m(\omega) = \lim_{\lambda\to\infty} \mathcal{G}_m(\omega + \lambda) \quad m = b, s_\sigma, d \tag{2.82}$$

One can show [90,92] that this shift does not affect physical quantities like the dot Green's function since it corresponds to apply a gauge transformation to the pseudo-particle operators according to $b \to e^{i\lambda t} b$, $s_\sigma \to e^{i\lambda t} s_\sigma$ and $d \to e^{i\lambda t} d$. In other words, this is a symmetry of the Anderson model [61, 90, 92].

After analytic continuation and projection, in the frequency domain, the self-energies obey the following self-consistent equations [61]

$$\begin{aligned}
\Sigma_b(\omega) &= \int_{-\infty}^{\infty} \frac{d\epsilon}{\pi} f(\epsilon) \sum_\sigma \Delta_\sigma(\epsilon) G_{s_\sigma}(\epsilon+\omega) \Lambda_\sigma^{(0)}(\omega,\epsilon) \\
\Sigma_{s_\sigma}(\omega) &= \int_{-\infty}^{\infty} \frac{d\epsilon}{\pi} f(\epsilon) [\Delta_\sigma(-\epsilon) G_b(\epsilon+\omega) \Lambda_\sigma^{(0)}(\epsilon+\omega,-\epsilon) + \Delta_{\bar{\sigma}}(\epsilon) G_{d_{\sigma\bar{\sigma}}}(\epsilon+\omega) \Lambda_{\sigma\bar{\sigma}}^{(2)}(\epsilon+\omega,\epsilon)] \\
\Sigma_{d_{\sigma\bar{\sigma}}}(\omega) &= \int_{-\infty}^{\infty} \frac{d\epsilon}{\pi} f(\epsilon) [\Delta_\sigma(-\epsilon) G_{s_{\bar{\sigma}}}(\epsilon+\omega) \Lambda_{\sigma\bar{\sigma}}^{(2)}(\omega,-\epsilon) + \Delta_{\bar{\sigma}}(-\epsilon) G_{s_\sigma}(\epsilon+\omega) \Lambda_{\bar{\sigma}\sigma}^{(2)}(\omega,-\epsilon)]
\end{aligned} \tag{2.83}$$

where $\Delta_\sigma(\epsilon) = \pi \sum_{\mathbf{k}} |V_{\mathbf{k}\sigma}|^2 \delta(\epsilon - \varepsilon_{\mathbf{k}\sigma})$ is the hybridization function, and the pseudo-particle

propagators are expressed in terms of their respective self-energies, namely:

$$\begin{aligned} G_b(\omega) &= [\omega - \lambda - \Sigma_b(\omega)]^{-1} \\ G_{s_\sigma}(\omega) &= [\omega - \lambda - \varepsilon_0 - \Sigma_{s_\sigma}(\omega)]^{-1} \\ G_d(\omega) &= [\omega - \lambda - 2\varepsilon_0 - U - \Sigma_d(\omega)]^{-1} \end{aligned} \tag{2.84}$$

The functions $\Lambda^{(2)}_{\bar{\sigma}\sigma}(\omega,\omega')$ and $\Lambda^{(0)}_{\sigma}(\omega,\omega')$ contain vertex corrections and are given by

$$\begin{aligned} \Lambda^{(0)}_{\sigma}(\omega,\omega') &= 1 + \int_{-\infty}^{\infty} \frac{d\epsilon}{\pi} f(\epsilon)\Delta_{\bar{\sigma}}(\epsilon) G_{s_{\bar{\sigma}}}(\omega+\epsilon) G_{d_{\bar{\sigma}\sigma}}(\omega+\omega'+\epsilon) \\ \Lambda^{(2)}_{\sigma\bar{\sigma}}(\omega,\omega') &= 1 + \int_{-\infty}^{\infty} \frac{d\epsilon}{\pi} f(-\epsilon)\Delta_{\sigma}(\epsilon) G_{s_{\bar{\sigma}}}(\omega-\epsilon) G_{b}(\omega-\omega'-\epsilon). \end{aligned} \tag{2.85}$$

If we discard the vertex corrections, which correspond to set $\Lambda^{(2)}_{\bar{\sigma}\sigma}(\omega,\omega') = \Lambda^{(0)}_{\sigma}(\omega,\omega') = 1$, we obtain the so called non-crossing approximation (NCA) [60]. If we include the vertex corrections we arrive at the one-crossing approximation (OCA) [61,93]. This nomenclature is related to the diagrams that represent each approximation, see Fig. 7. In the NCA diagrams the lines representing bath conduction electrons do not cross. In the one crossing approximation, in addition to all NCA diagrams, higher order diagrams in which the conduction electron lines cross once are also included.

From the solution of the above equations we obtain the pseudo-particle propagators. Next we can compute the dot density of states, $\rho_\sigma(\omega)$, since it can be expanded in terms of the pseudoparticle propagators according to the following expression [61, 93]

$$\rho_\sigma(\omega) = \frac{Z_C(0)}{Z_C(1)} \int_{-\infty}^{\infty} d\epsilon \; e^{-\beta\epsilon}[A_b(\epsilon)A_{s_\sigma}(\epsilon+\omega) \; + A_{s_\sigma}(\epsilon)A_d(\epsilon+\omega)] \tag{2.86}$$

where $Z_C(1)/Z_C(0)$, which came from the projection to the $Q = 1$ subspace, can be written as:

$$\frac{Z_C(1)}{Z_C(0)} = \int d\epsilon e^{-\beta\epsilon}[A_b(\epsilon) + \sum_\sigma A_{s_\sigma}(\epsilon) + A_d(\epsilon)] \tag{2.87}$$

The numerical implementation of the above equations is not trivial because the term $e^{-\beta\epsilon}$ diverges exponentially for $\epsilon < 0$. To compensate this behavior the pseudo-particle spectral functions must vanish exponentially below some threshold energy E_0 in order to obtain a finite ρ_σ. It was further noted that at $T = 0$ the auxiliary spectral functions diverge at E_0 [90, 91]. To circumvent these problems, it is convenient to formulate the NCA/OCA equations in terms of [90, 91]

$$\tilde{A}_m(\omega) \equiv A_m/f(-\omega) \quad \text{and} \quad \widetilde{\mathrm{Im}\Sigma_m}(\omega) \equiv \mathrm{Im}\Sigma_m(\omega)/f(-\omega) \tag{2.88}$$

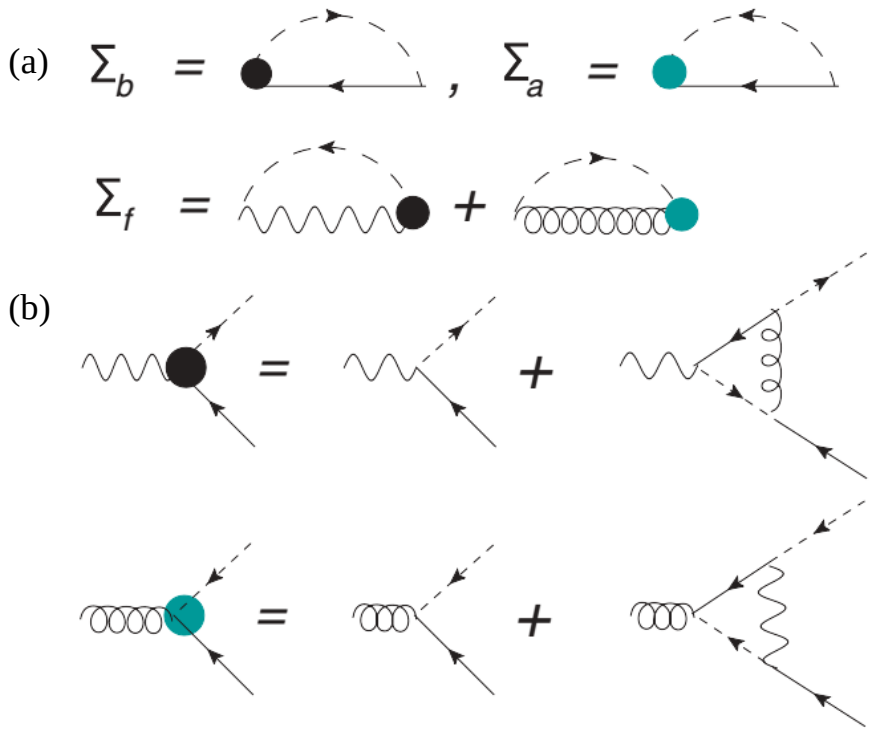

Figure 7: (a) Diagrammatic representation of the pseudoparticle self-energies. (b) Vertex corrections. The solid, wiggly, dashed, and curly lines corresponds to the pseudofermion, empty boson, conduction electron, and doubly occupied boson propagators, respectively. When the black and green vertices in (a) are replaced by the bare ones we obtain the diagrams of the non-crossing approximation. The one crossing approximation consists of including the vertices in the self-energy diagrams. Extracted from Ref. [62]

.

The Fermi distribution appearing in the definitions above removes both the problem of the diverging exponential factor and the threshold behavior of the pseudo-particle spectral functions. Before performing the projection, in which we make the replacement $\omega \to \omega+\lambda$, we re-define the frequency scale of the pseudo-particle spectral functions according to $\omega \to \omega+\lambda_0$, where λ_0 is a finite parameter. At the NCA level, the pseudo-particle density of states can now be written, using the tilde quantities, Eq. (2.88), as

$$\begin{aligned}
\tilde{A}_b(\omega) &= -\frac{1}{\pi}\frac{\widetilde{\text{Im }\Sigma_b}(\omega)}{[\omega+\lambda_0-\text{Re }\Sigma_b(\omega)]^2+[\text{Im }\Sigma_b(\omega)]^2} \\
\tilde{A}_{s_\sigma}(\omega) &= -\frac{1}{\pi}\frac{\widetilde{\text{Im }\Sigma_{s_\sigma}}(\omega)}{[\omega+\lambda_0-\varepsilon_0-\text{Re }\Sigma_{s_\sigma}(\omega)]^2+[\text{Im }\Sigma_{s_\sigma}(\omega)]^2} \\
\tilde{A}_d(\omega) &= -\frac{1}{\pi}\frac{\widetilde{\text{Im }\Sigma_d}(\omega)}{[\omega+\lambda_0-2\varepsilon_0-U-\text{Re }\Sigma_d(\omega)]^2+[\text{Im }\Sigma_d(\omega)]^2}
\end{aligned} \tag{2.89}$$

where the tilde self-energies are given by

$$\begin{aligned}
\widetilde{\text{Im }\Sigma_b}(\omega) &= \sum_\sigma \int_{-\infty}^{\infty} \frac{d\epsilon}{\pi} \frac{f(\epsilon)f(-\epsilon-\omega)}{f(-\omega)} \Delta_\sigma(\epsilon)\tilde{A}_{s_\sigma}(\epsilon+\omega) \\
\widetilde{\text{Im }\Sigma_{s_\sigma}}(\omega) &= \int_{-\infty}^{\infty} \frac{d\epsilon}{\pi} \frac{f(\epsilon)f(-\epsilon-\omega)}{f(-\omega)} [\Delta_\sigma(-\epsilon)\tilde{A}_b(\epsilon+\omega) + \Delta_{\bar{\sigma}}(\epsilon)\tilde{A}_d(\epsilon+\omega)] \\
\widetilde{\text{Im }\Sigma_d}(\omega) &= \int_{-\infty}^{\infty} \frac{d\epsilon}{\pi} \frac{f(\epsilon)f(-\epsilon-\omega)}{f(-\omega)} [\Delta_\sigma(-\epsilon)\tilde{A}_{s_{\bar{\sigma}}}(\epsilon+\omega) + \Delta_{\bar{\sigma}}(-\epsilon)\tilde{A}_{s_\sigma}(\epsilon+\omega)]
\end{aligned} \tag{2.90}$$

The real parts of the self-energies can be obtained using the Kramers-Kronig relation (see Appendix B), namely,

$$\text{Re }\Sigma_m(\omega) = \frac{1}{\pi}\mathcal{P}\int d\epsilon \frac{\text{Im }\Sigma_m(\epsilon)}{\epsilon-\omega} \quad m = b, s_\sigma, d \tag{2.91}$$

thus, closing the set of equations.

The dot spectral function is finally written as

$$\rho_\sigma(\omega) = \frac{Z_C(0)}{Z_C(1)} \int_{-\infty}^{\infty} d\epsilon \ \frac{f(\epsilon)f(-\epsilon-\omega)}{f(-\omega)} [\tilde{A}_b(\epsilon)\tilde{A}_{s_\sigma}(\epsilon+\omega) \ + \tilde{A}_{s_\sigma}(\epsilon)\tilde{A}_d(\epsilon+\omega)] \tag{2.92}$$

where $Z_C(1)/Z_C(0)$ is now given by

$$\frac{Z_C(1)}{Z_C(0)} = \int d\epsilon f(\epsilon)[\tilde{A}_b(\epsilon) + \sum_\sigma \tilde{A}_{s_\sigma}(\epsilon) + \tilde{A}_d(\epsilon)] \ . \tag{2.93}$$

In order to converge the above equations, one can follow, at least, two approaches. Both must be combined with an appropriate choice of frequency meshes that will resolve properly the extremely sharp peaks often present in the pseudo-particle spectral functions.

In the first method, one can determine λ_0 appearing in Eq. (2.89) in each iteration so that

$$\frac{Z_C(1)}{Z_C(0)} = \int d\epsilon f(\epsilon)[\tilde{A}_b(\epsilon) + \sum_\sigma \tilde{A}_{s_\sigma}(\epsilon) + \tilde{A}_d(\epsilon)] = 1 \ . \tag{2.94}$$

This procedure guarantees that, at $T = 0$, the threshold divergence E_0 of the pseudo-particle spectral functions is at zero frequency [90, 92]. In this case one can use a grid with more frequency points near $\omega = 0$.

It turns out that when $T \neq 0$ the above method may eventually present difficulties to converge since now E_0 is not *exactly* at $\omega = 0$ and even changes in each iteration. A small deviation of E_0 from the zero frequency is enough to compromise the convergence of a calculation in a fixed mesh even the one with large density of points close to $\omega = 0$. In this case, instead of changing the grid in each iteration, a second approach can be used, which

is to calculate λ_0 so that the peak position of the main pseudo-particle is always fixed exactly at zero frequency. An example of such approach is presented in Ref. [61]. This allows one to use the same mesh in each iteration. In this thesis we use both approaches depending on which ones presents the best convergence.

3 Numerical analysis

In this chapter we provide an extensive comparison between the approximate methods presented previously, namely, EOM, NCA, OCA applied to the SIAM. Additionally we also include results obtained by the numerical renormalization group (NRG) method [1] [94]. We discuss the strengths and weaknesses of these approaches, considering their simplicity and computational cost. For the EOM method, we mainly study two truncation schemes: the one given by Eq. (2.31), which we call here EOM1 method, and that of Eq. (2.46), which we call here EOM2 method. The numerical implementation of EOM and NCA methods were performed by the author. For calculations using the OCA method we used the numerical implementation of Kristjan Haule from Rutgers University [2]. Using the Green's functions obtained in each approach we calculate the density of states and the conductance in the linear response regime as a function of the chemical potential (represented by changes in the quantum dot level ε_0) and the temperature.

Quantum dots display very distinct transport features depending on the temperature. The high temperature limit is associated to the Coulomb blockade regime, while at low temperatures quantum dots show Kondo physics. Here "high" and "low" refer to the ratio between the actual temperature T and the Kondo temperature T_K that defines the relevant physical temperature scale.

Accordingly, it is standard to analyse the SIAM results taking as a guide these two limiting case of high $T \gg T_K$ an low temperatures $T \lesssim T_K$. The characteristic Kondo temperature of the system can be estimated by the Haldane expression [86], namely,

$$k_B T_K \sim \sqrt{U\Gamma}\exp\left[-\pi\frac{|\varepsilon_0||\varepsilon_0+U|}{U\Gamma}\right]. \tag{3.1}$$

[1] The NRG calculations were performed by the professor Luis Gregório Dias da Silva from the University of São Paulo (USP).

[2] The algorithm can be found at http://hauleweb.rutgers.edu/tutorials/. Note that the impurity solver code is part of a full package developed to realistically calculate the electronic properties of strongly correlated materials by merging density functional theory and the dynamical mean field theory.

Here we use the wide band approximation and Γ, defined by Eq. (2.8), is assumed to be constant for energies within the bandwidth.

3.1 Spectral functions and density of states

We begin our analysis by studying the spectral function, that, in general, reads

$$\mathcal{A}(\mathbf{r},\mathbf{r}',\omega) = i[G^r(\mathbf{r},\mathbf{r}',\omega) - G^a(\mathbf{r},\mathbf{r}',\omega)] \tag{3.2}$$

whose diagonal term give the local density of states (LDOS)

$$\rho(\mathbf{r},\omega) = -\frac{1}{\pi}\int d\mathbf{r}'\delta(\mathbf{r}-\mathbf{r}')\mathrm{Im}G^r(\mathbf{r},\mathbf{r}',\omega) \tag{3.3}$$

Since we are interested in the density of states (DOS) of the quantum dot, we consider the simple expression

$$\rho_\sigma(\omega) = -\frac{1}{\pi}\mathrm{Im}G^r_\sigma(\omega) \tag{3.4}$$

for a given spin projection σ.

Let us first study the high temperature limit. In all calculations presented in this chapter we use $U = 10$ (arbitrary units). In Figs. 8, 9, and 10 we set $\Gamma = T = 0.1U$. In the particle-hole symmetric point, where $\varepsilon_0 = -U/2$, the estimated Kondo temperature, calculated from the Eq. (3.1) is $T_K \approx 10^{-4}U$. In this case only the density of states obtained by the NRG approach exhibit a more severe discrepancy in comparison with the other methods. The density of states obtained by OCA, NCA, and EOM methods agree very well giving resonances at $\omega = \varepsilon_0$ and $\omega = \varepsilon_0 + U$. The double peak structure is the main feature of this regime and it helps to understand the Coulomb blockade in quantum dots. Both peaks have the same height which implies that the dot is occupied with one electron. With respect to the NRG result it is important to emphasize that the NRG approach suffers from some difficulties in spectral functions calculations. In the NRG implementation used here, called the complete Fock space algorithm (CFS-NRG), the spectral density is not computed for $|\omega| < T$ [94, 95]. At high temperatures this problem becomes much more evident as can be seen in Figs. 8, 9, and 10. There is another implementation of NRG method called the full density matrix algorithm (FDM-NRG) [94, 96] that can be used to compute spectral quantities at energies lower than the temperature, but we will not use this approach here since the energy window of $|\omega| < T$ is not the main issue of analysis. In Fig. 8 we also note that the two resonances appearing in the density of states are also not well described in the NRG result. The poor description

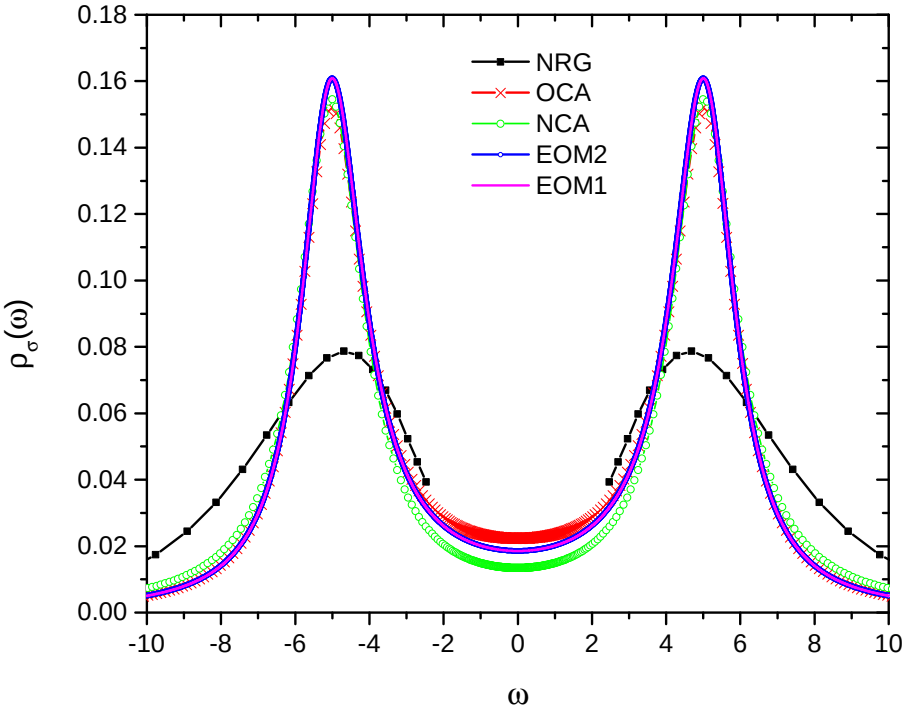

Figure 8: Density of states of the SIAM for the particle-hole symmetric case, $\varepsilon_0 = -U/2$, with $\Gamma = 0.1U$ and $T = 0.1U$ and $T/T_K \approx 1000$ obtained by different methods.

of the high energy features of the spectral functions are also a recurrent problem in NRG calculations and has already been reported and discussed in the literature [30, 38]. The spectral resolution of the high energy features depends on the numerical procedures used in NRG calculations [38] and in principle can be improved at the cost of an increase of the computational effort. We will not discuss the details involved in such procedures here. The results of the standard NRG are sufficient to show that this method is neither numerically efficient nor accurate for the $T \gg T_K$ temperature regime.

As one moves away from the particle hole symmetric case, the differences between the methods become more evident. The spectral densities still show good agreement for $\varepsilon_0 = -0.26U$, see Fig. 9, except for the NRG result. However, as shown in Fig. 10, for $\varepsilon_0 = 0$ the EOM1 spectral function exhibit a considerably lower peak at $\omega = 0$ in comparison with the ones obtained in EOM2, NCA and OCA.

Remarkably, we find that the EOM1 approximation gives poor results for $\varepsilon_0 = 0$ even in a very weak coupling , $\Gamma \ll U$, in which the Kondo temperature becomes extremely low. This is shown in Fig. 11, for $\Gamma = 0.02U$ and $T = 0.01U$. The Kondo temperature in this case is $T_K \approx 10^{-18}U$ for $\varepsilon_0 = -U/2$. In this case we do not compare with OCA since for such low T/T_K the calculations converge very slowly. This result suggests that in such situations even at weak coupling, many-body corrections to the embedding self-energy

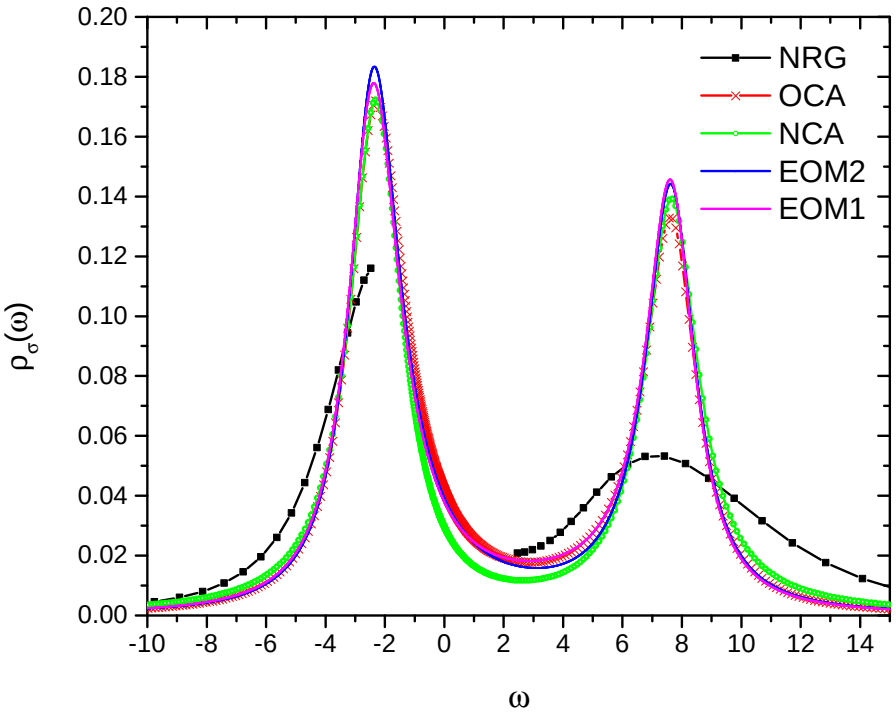

Figure 9: Density of states of the SIAM for $\varepsilon_0 = -0.26U \simeq -U/4$, with $\Gamma = 0.1U$ and $T = 0.1U$ obtained by different methods.

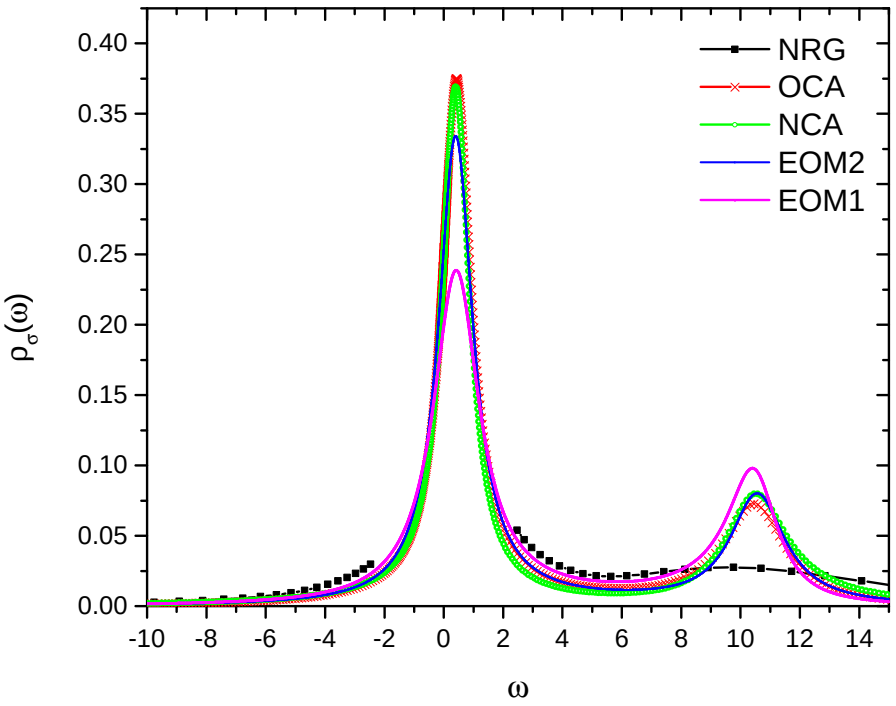

Figure 10: Density of states of the SIAM calculated within different approximation schemes for $\Gamma = 0.1U$, $T = 0.1U$, and $\varepsilon_0 = 0$.

are significant.

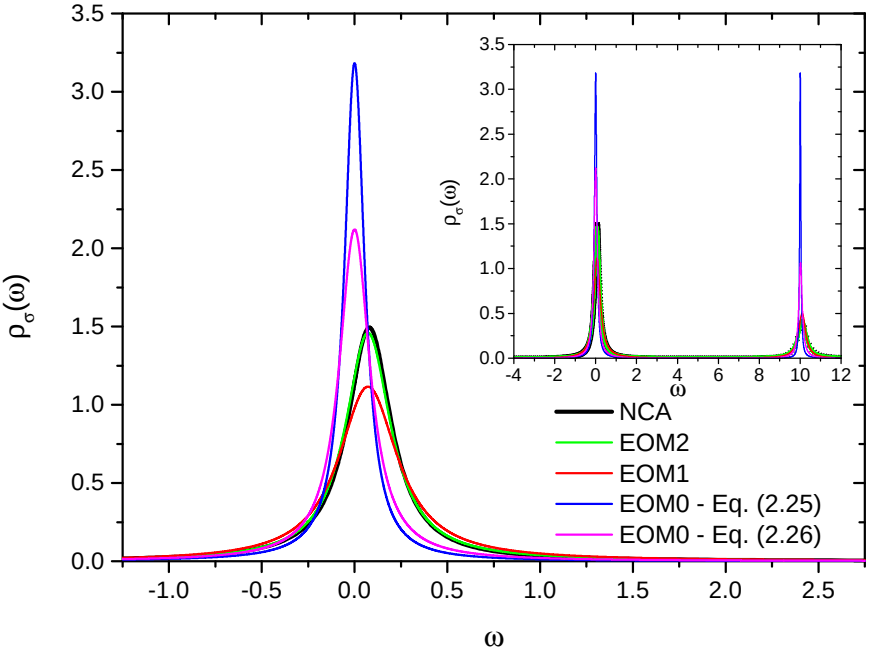

Figure 11: Impurity density of states for $\Gamma = 0.02U$, $\varepsilon_0 = 0$ and $T = 0.1U$ near the Fermi level $\omega = 0$ obtained by different EOM schemes and also by the NCA. Here the estimated Kondo temperature is $T_K \sim 10^{-17}$ for $\varepsilon_0 = -U/2$. In the inset we show the density of states in a more extended range of energies.

As we will discuss in the next section, this feature prevents the EOM1 method from yielding conductance values in agreement with the other methods, even in the high temperature limit. This is rather unexpected, since at the Coulomb blockade regime most studies neglect entirely many-body effects in the self-energy and use an even simpler approximation scheme, namely, the EOM0 truncation, Eqs. (2.25) and (2.26). However, assuming that $\Sigma(\omega)$ is solely due to embedding, $\Sigma^r = -i\Gamma/2$, a straightforward analytical calculation gives $\rho_{\rm ex}^{\rm EOM0}(0) \approx 3.18$ using the exact form of the Green's function given in Eq. (2.25), and $\rho_{\rm app}^{\rm EOM0}(0) \approx 2.12$ using the approximated version given in Eq. (2.26) showing the quantitative inaccuracy of the most naive approaches, as can be seen in Fig. 11 (see also the appendix A).

Now we turn to the low temperature regime. Our results for the symmetric SIAM are summarized in Fig. 12. Firstly, let us focus our analyzis in the results obtained by the NRG, NCA, and OCA methods. The density of states of these methods exhibits the usual resonances at the energies $\omega = \varepsilon_0$ and $\omega = \varepsilon_0 + U$. However in the NRG result these peaks are considerably different from the ones obtained in the other approaches. As discussed previously in this section and reported in the literature the description of high

energy features of spectral densities in the NRG method presents some problems related to the numerical procedures used in the calculations [38,94]. In this way, we can conclude that the single particle resonances are better described in NCA and OCA [38].

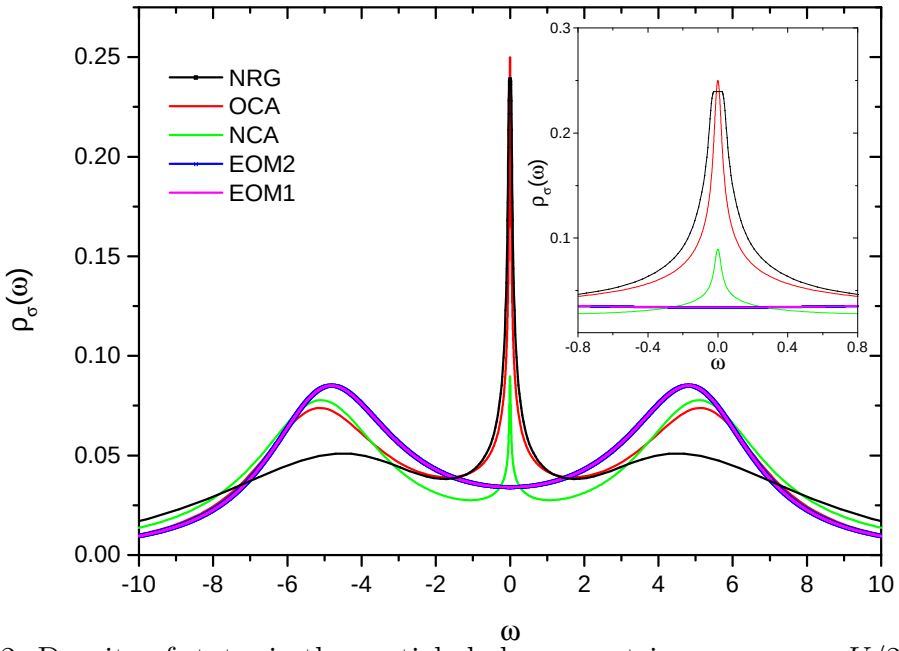

Figure 12: Density of states in the particle-hole symmetric case, $\varepsilon_0 = -U/2$, for $\Gamma = 0.2U$, $T = 0.001U$. Here the estimated Kondo temperature is $T_K \approx 0.009U$. The inset shows a zoom of the region near the Fermi level $\omega = 0$.

The density of states obtained by NRG, NCA and OCA exhibit a pronounced and sharp peak at the Fermi level. This peak is a signature of the Kondo effect, which is a consequence of the strong correlations that develop between the dot and the bath electrons when the temperature becomes comparable to the Kondo temperature of the system. For the symmetric case, $\varepsilon_0 = -U/2$, and $\Gamma = 0.2U$, the estimated Kondo temperature, calculated from the Haldane expression, is $T_K \approx 0.009U$. As discussed in the previous chapter, the NRG was the first approach to give a satisfactory description of the Kondo physics down to the $T \to 0$ limit, yielding an accurate account of the low excitation energies in this regime and the correct characteristic Kondo temperature of the system [2, 7, 38]. Hence it is tradicionally recommended as one of the best methods to address the low temperature limit as well as the low energy physics of systems displaying the Kondo effect, and will serve as a benchmark for our $T \lesssim T_K$ analysis.

Figure 12 also shows an excellent agreement between both EOM schemes which is related to the already mentioned equivalence of the Green's functions of both methods in the particle-hole symmetric case, see Appendix A. On the other hand the peak at

$\omega = 0$ is not present. As discussed in the previous chapter the EOM1 method [46] is not expected to capture the physics of the problem because many-body correlation terms are discarded by the used truncation scheme. The EOM2 approach [59], should work better. However, there is a deeper reason that prevents the EOM2 to capture Kondo physics in this setting: the particle-hole symmetry prevents the EOM Green's functions to exhibit a resonance at $\omega = 0$ [59].

Let us discuss the performance of the NCA and OCA methods. It is a known result in the literature that the OCA method improves some pathologies of the NCA approach, especially those related to the description of the Kondo regime [38, 86, 87]. Assuming that the Kondo peak in the NRG result is the most accurate we verify that the OCA method considerably improves the width and the height of the Kondo resonance when compared with the one given by the NCA. In this sense the OCA approach provides a better estimative of the scale T_K for the system [36, 86]. However it is also known that the OCA method also presents some problems. When the temperature is decreased well below T_K, the density of states obtained using OCA violates the limit imposed by the Friedel sum rule [7, 97], namely,

$$\rho(0) = \frac{1}{\pi \frac{\Gamma}{2}} \ , \tag{3.5}$$

sometimes referred to as the "unitarity" condition [59]. In other words, OCA overestimates the height of the Kondo peak as shown in Fig. 13. This undesirable feature starts to appear at about $T \lesssim 0.1 T_K$. Thus, the temperature $T = 0.1 T_K$ can be considered as the limit of accuracy for the OCA method [25, 51, 62, 98] .

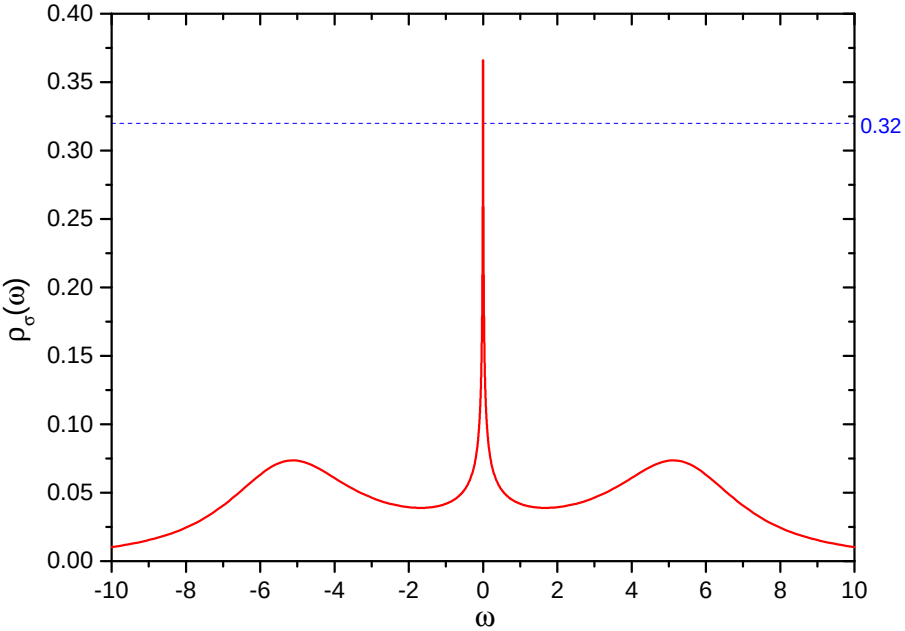

Figure 13: Density of states obtained using the OCA method in the particle-hole symmetric case, $\varepsilon_0 = -U/2$, for $\Gamma = 0.2U$, $T = 0.0001U$. Here the Kondo temperature is $T_K \approx 0.009U$. Note that the height of the Kondo resonance is above the limit imposed by the Friedel sum rule, indicated by the dashed line.

Let us now address the asymmetric case, namely, when $\varepsilon_0 \neq -U/2$. In Fig. 14 we plot the spectral functions for $\varepsilon_0 = -0.26U \approx -U/4$. The NRG, NCA, and OCA results show a Kondo peak at $\omega \sim 0$ as expected since the Kondo temperature in this case is $T_K \approx 0.02U$, according to the Haldane's expression, Eq. (3.1). OCA overestimates the height of the Kondo peak which is better described in the NRG approach. On the other hand, the one crossing approximation improves the width of the Kondo resonance over the NCA result although it still underestimates the Kondo temperature. The slave boson methods also yield a broad resonance at $\omega = \varepsilon_0 + U = 0.74U$ and another one resembling a shoulder at $\varepsilon_0 = -0.26U$ while in NRG these resonances are less pronounced, a similar feature to the one discussed in Fig. 12.

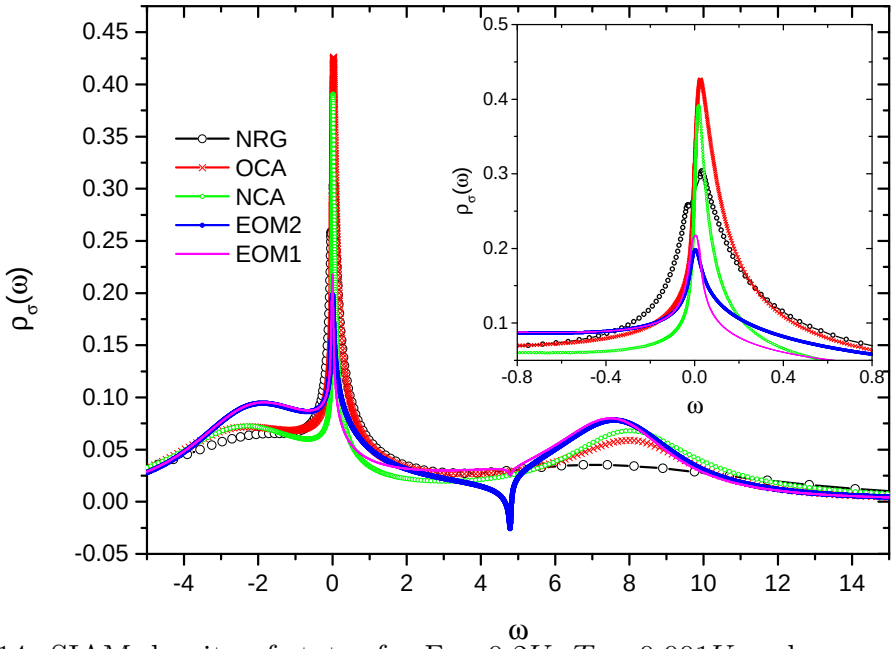

Figure 14: SIAM density of states for $\Gamma = 0.2U$, $T = 0.001U$ and $\varepsilon_0 = -0.26U \simeq -U/4$ obtained from different approximation schemes. The inset shows a zoom of the region near the Fermi level $\omega = 0$.

The EOM density of states also exhibit a resonance at the Fermi level, although with a smaller peak height than in OCA and NCA, and an unphysical peak at $\omega = 2\varepsilon_0 + U = 0.48U$. This peak is enhanced in the EOM2 solution as compared with the EOM1 approximation (see also Fig. 16), leading to an unphysical negative density of states. This spurious singularity is an artifact of the solution and comes from the decoupling scheme used in both EOM methods. Another issue related to the truncation is whether one can regard the peak at the Fermi energy in the EOM1 result as a Kondo peak. Actually the truncation in Eqs. (2.29) and (2.30) discards unlike spin correlations between the dot and the bath, that is, terms like $\langle c_{\bar{\sigma}} d^\dagger_\sigma \rangle$. Hence in principle the Kondo effect should not be

manifest at this approximation level. Like the spurious peak at $\omega = 2\varepsilon_0 + U$, this peak at $\omega = 0$ can be misleading, since it seems more an artifact of the truncation than a peak due to many-body effects.

Let us examine this issue in more detail. In the EOM1 solution both singularities at $\omega = 0$ and $\omega = 2\varepsilon_0 + U$ are related to the self-energy $\Sigma_1(\omega)$ given by Eq. (2.34). More precisely, we can trace back their origin to the digamma functions present in the self-energy. In Fig. 15 we show $\Sigma_1^r(\omega)$ for the same set of parameters of the Fig. 14. One can see that the two peaks at $\omega = 0$ and at $\omega = 2\varepsilon_0 + U$ are associate with the real part of $\Sigma_1(\omega)$. When we calculate the Green's function by arbitrarily setting $\mathrm{Re}[\Sigma_1(\omega)] = 0$ both peaks disappear, as shown in Fig. 16.

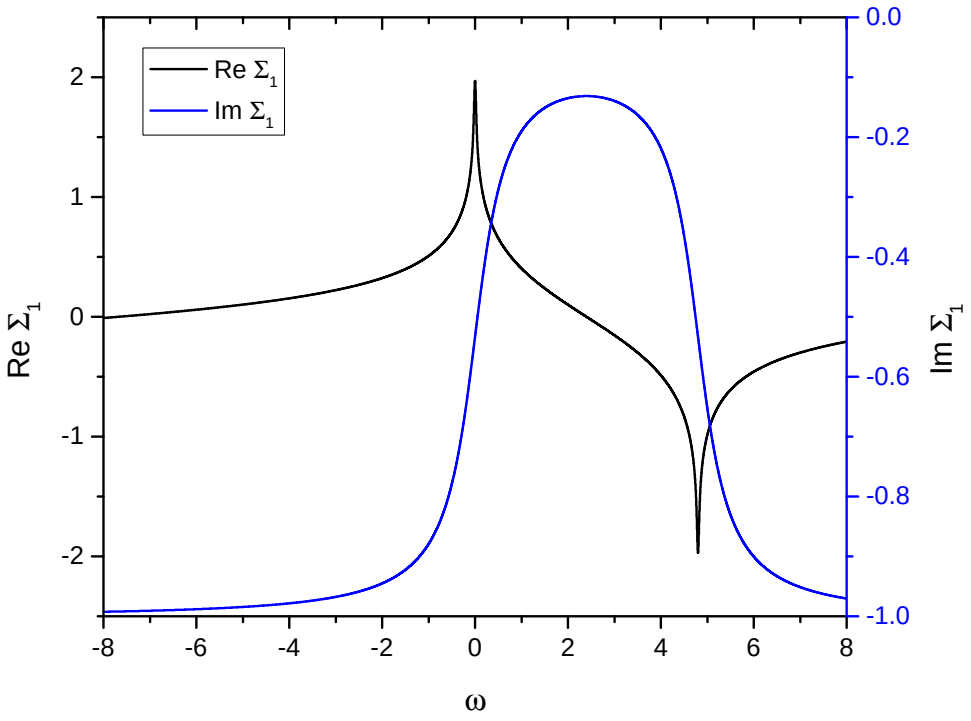

Figure 15: Self-energy $\Sigma_1^r(\omega)$ in the EOM1 approximation for $\Gamma = 0.2U$, $T = 0.001U$, and $\varepsilon_0 = -0.26U$.

In EOM2 case, the corresponding singularities come from the functions $P(z)$ and $Q(z)$, see Figs. 17 and 18. In the integrals of Eqs. (2.51) and (2.52) we note that the integrands have a great similarity to the one appearing in the integral for $\Sigma_1(\omega)$, Eq. (2.32). More importantly, in all of the integrands, there is a Fermi distribution $f(\varepsilon)$ multiplied by a term of the form $F(\varepsilon)/(\omega - \varepsilon)$. For $F(\varepsilon) = 1$ the integral can be evaluated analytically giving the digamma function, as already discussed [see Eq. (2.34)]. In Eqs. (2.51) and (2.52) we have $F(\varepsilon) = \mathrm{Im}[G^r(\varepsilon)\Sigma^r(\varepsilon)]$, $F(\varepsilon) = \mathrm{Im}[G^r(\varepsilon)]$, etc. that need to be calculated numerically. Figure 19 clearly shows that, like in the case of EOM1, the singularities in

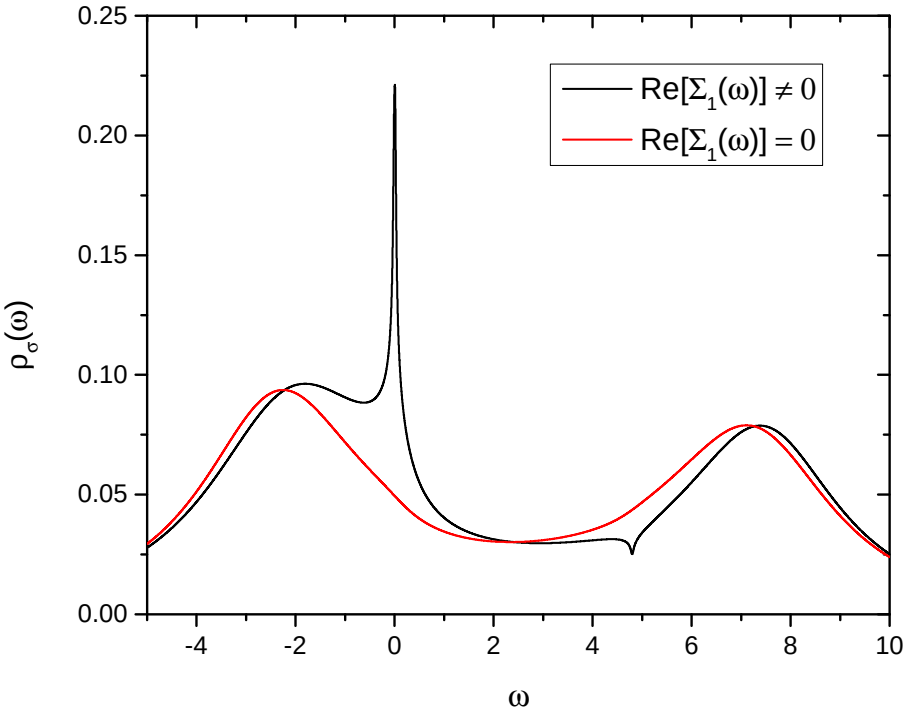

Figure 16: SIAM density of states obtained using EOM1 for $\Gamma = 0.2U$, $T = 0.001U$,and $\varepsilon_0 = -0.26U \approx -U/4$. The black line corresponds to the result shown in Fig. 14, while the red one is obtained by arbitrarily setting $\mathrm{Re}[\Sigma_1(\omega)] = 0$.

EOM2 solution come from these types of integrals. The singularity at $\omega = 0$ are associated with the functions $P(z)$ and $Q(z)$ and the one at $\omega = 2\varepsilon_0 + U$ are associated with the functions $P(z_2)$ and $Q(z_2)$, all of them appearing in Eq. (2.46). We find that only when we exclude both functions (and both their real and imaginary parts), the peaks disappear in the spectral function.

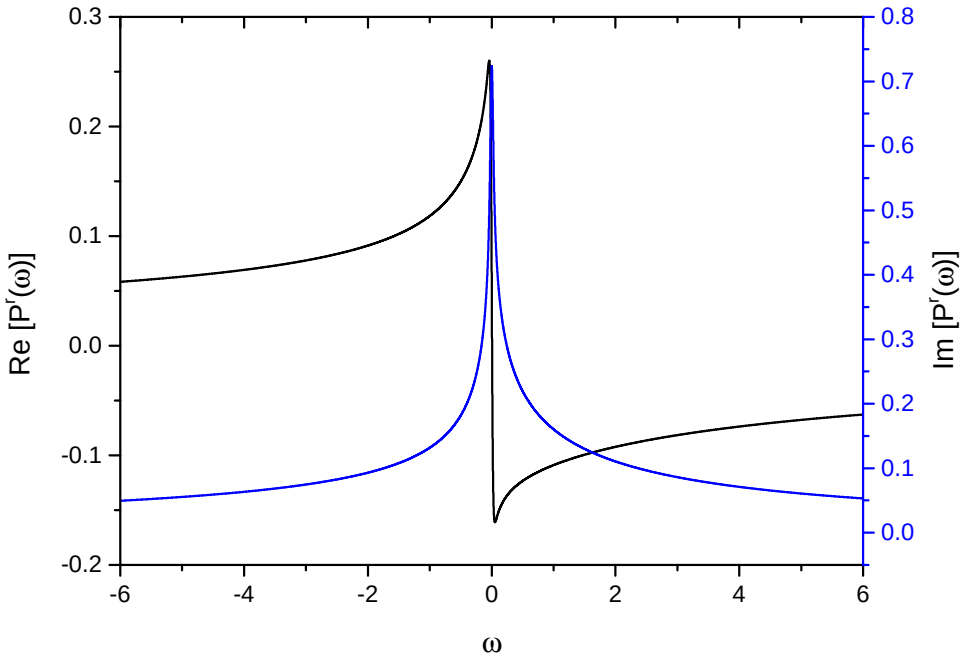

Figure 17: Real and imaginary parts of the function $P^r(\omega)$ as a function of the frequency ω for the EOM2 density of states of Fig. 14.

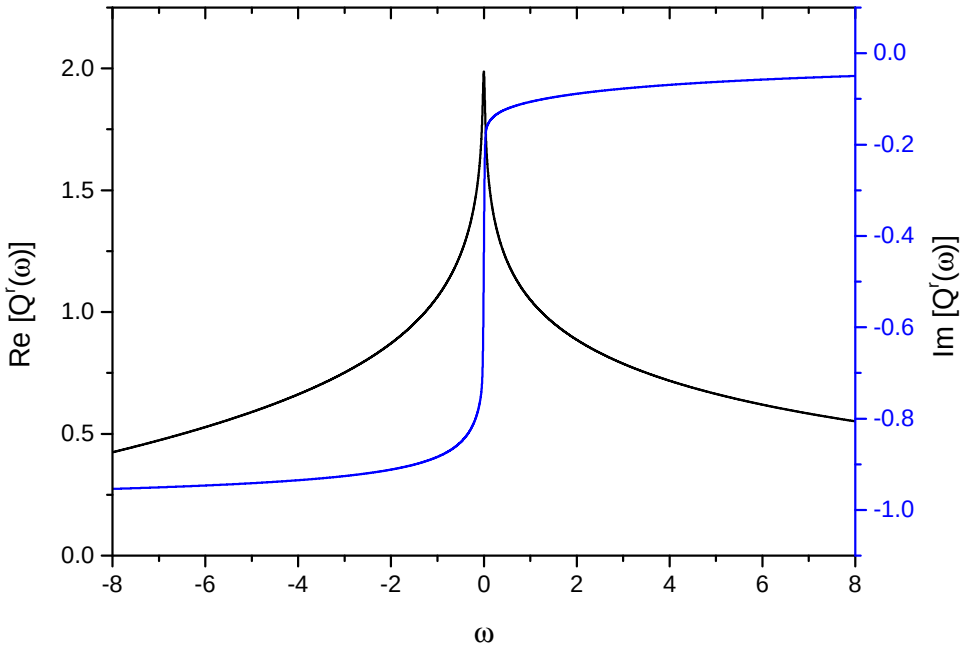

Figure 18: Real and imaginary parts of the function $Q^r(\omega)$ as a function of the frequency ω for the EOM2 density of states of Fig. 14.

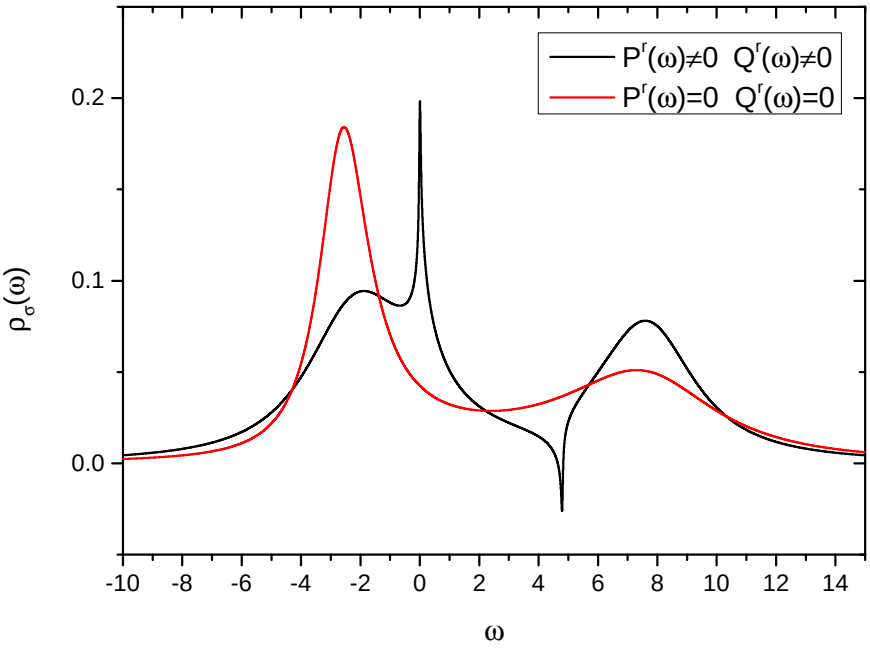

Figure 19: Density of states of the SIAM in the EOM2 approximation and by imposing $P^r(\omega) = Q^r(\omega) = P^r(\omega_2) = Q^r(\omega_2) = 0$ for $\Gamma = 0.2U$, $T = 0.001U$, and $\varepsilon_0 = -2.6$

In Fig. 20 we show the computed density of states for $\varepsilon_0 = 0$. The differences between the methods at the energies ω very close to the Fermi level are remarkable. In the OCA and NCA density of states there is a sharp peak near $\omega = 0$ while no peak shows up in the results obtained by NRG and EOM2, see inset of Fig. 20. The presence of these peaks

in NCA and OCA results will influence the conductance calculations and we will return to this subject in the next section. The EOM1 density of states exhibits a somewhat unexpected result with an anti-peak (deep) at the Fermi level. This rather artificial feature severely compromises the performance of the EOM1 scheme in the conductance calculations as will be clear in the next section.

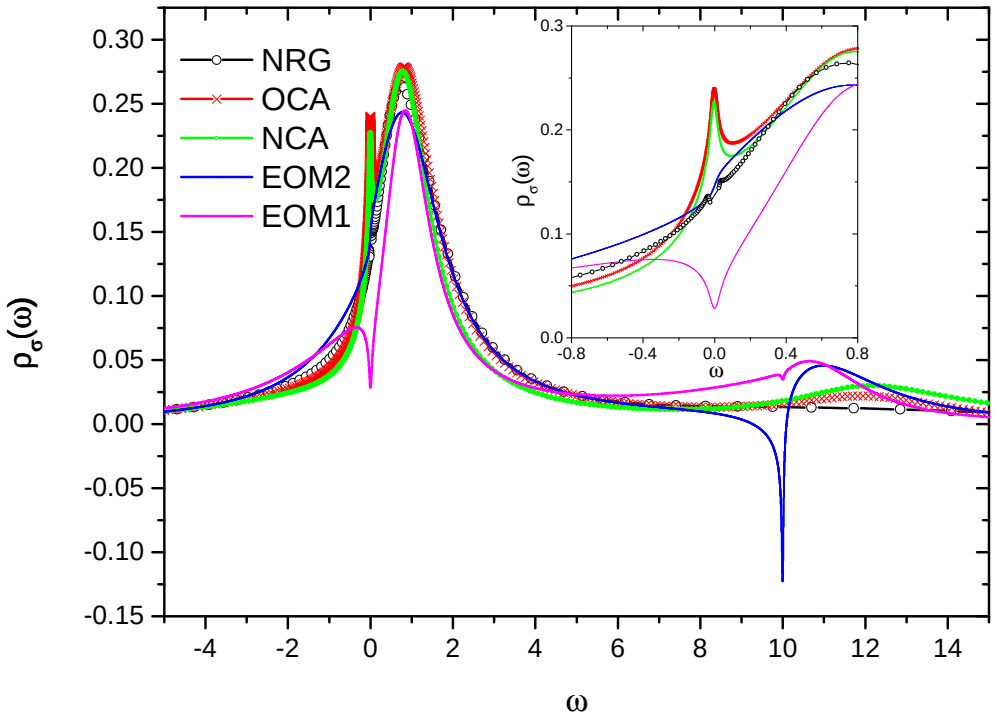

Figure 20: SIAM spectral function for $\Gamma = 0.2U$, $T = 0.001U$ and $\varepsilon_0 = 0$ obtained from different approximation schemes. The inset shows a zoom of the region near the Fermi level $\omega = 0$.

A discussion on the computational cost of the different approximation schemes is now in order. The most important bottleneck here is the large amount of CPU time that OCA spends when compared to the other methods. Let us comment on the calculation of a spectral function like the one in Fig. 12. We restrict our analysis, at least for a while, to NCA and OCA only since both were implemented in the same code by Haule [87]. We note that NCA is very fast even when running on just one core. We run a calculation for a single impurity Anderson model with a single level, using one core and $N = 1060$ points in the pseudo-particle frequency mesh. NCA converges in $9s$ within 20 iterations[3]. In contrast OCA converges in 76 minutes within 15 iterations. Next we run the same calculation using 12 cores. In this case OCA converges in 8.25 minutes. Typical calculations using

[3]The calculations were performed using the processor Intel ®Xeon ®X5650 2.67GHz.

the EOM1 solver takes no more than $10s$ and using the EOM2 solver about $30s$ to converge (running on just one core).

The double convolutions in the OCA approach, which involves overlapping integrations over functions with rich structure, are the major cause for this large CPU time [38]. In a single level NCA calculation with N points in the frequency mesh, there are three single convolutions to evaluate in each iteration. In the OCA scheme there are three double convolutions.

In the multi-orbital case, the OCA performance gets even worse since the number of pseudo-particle increases. For an impurity Anderson model with 2 levels using $N = 1698$ and 12 cores, NCA takes $13s$ to converge, while OCA takes 222 minutes.

Unless one has access to a larger number of cores this is a serious restriction for using OCA despite the remarkable work of Haule in optimizing the vertex corrections calculations. One of the greatest features of the Haule's implementation, besides the direct calculation of the Green's function on the real axis, is the use of frequency meshes with non-uniform spacing. This optimizes the calculation since it uses a less amount of points in numerical integrations. In summary, despite this remarkable optimization effort, OCA calculations need to be performed using as many CPU cores as possible otherwise it will have a bad performance when it comes to time to converge.

3.2 Conductance

In this section we study the conductance of the SIAM in the linear response regime, which is calculated using Eq. (2.5). In all calculations we fix the chemical potential at $\mu = 0$ as a reference energy. We also assume that the single-particle energy ε_0 can be tuned by an external applied voltage, $\varepsilon_0 = \varepsilon_0(x)$, such as a back gate voltage $x \equiv V_g$

Let us begin analyzing the high temperature limit. The most representative result of this regime is given in Fig. 21a where $T = 0.1U$ is much higher than the estimated Kondo temperature, $T_K = 0.0001U$, calculated for $\varepsilon_0 = -U/2$. All plots exhibit the main features of a Coulomb blockade regime: two peaks separated by an energy U with low conductance region in between. The Coulomb blockade peaks correspond to situations where the system resonances at ε_0 and $\varepsilon_0 + U$ have the same energy as $\mu = 0$. More explicitly, the Coulomb blockade conductance peak at $\varepsilon_0 = 0$ corresponds to a single-occupied dot, while the one at $\varepsilon_0 + U = 0$ is related to a double-occupation configuration.

The conductances shown in Fig. 21a calculated by all considered methods show a good qualitative agreement, except for the EOM1 result, which presents a more pronounced discrepancy especially near the charge fluctuation points $\varepsilon_0 = 0$, and $\varepsilon_0 + U = 0$. This rather unexpected behaviour of the EOM1 result is a consequence of the observed discrepancy in its density of states as compared to other methods, as discussed in the previous section (see Figs. 10 and 11).

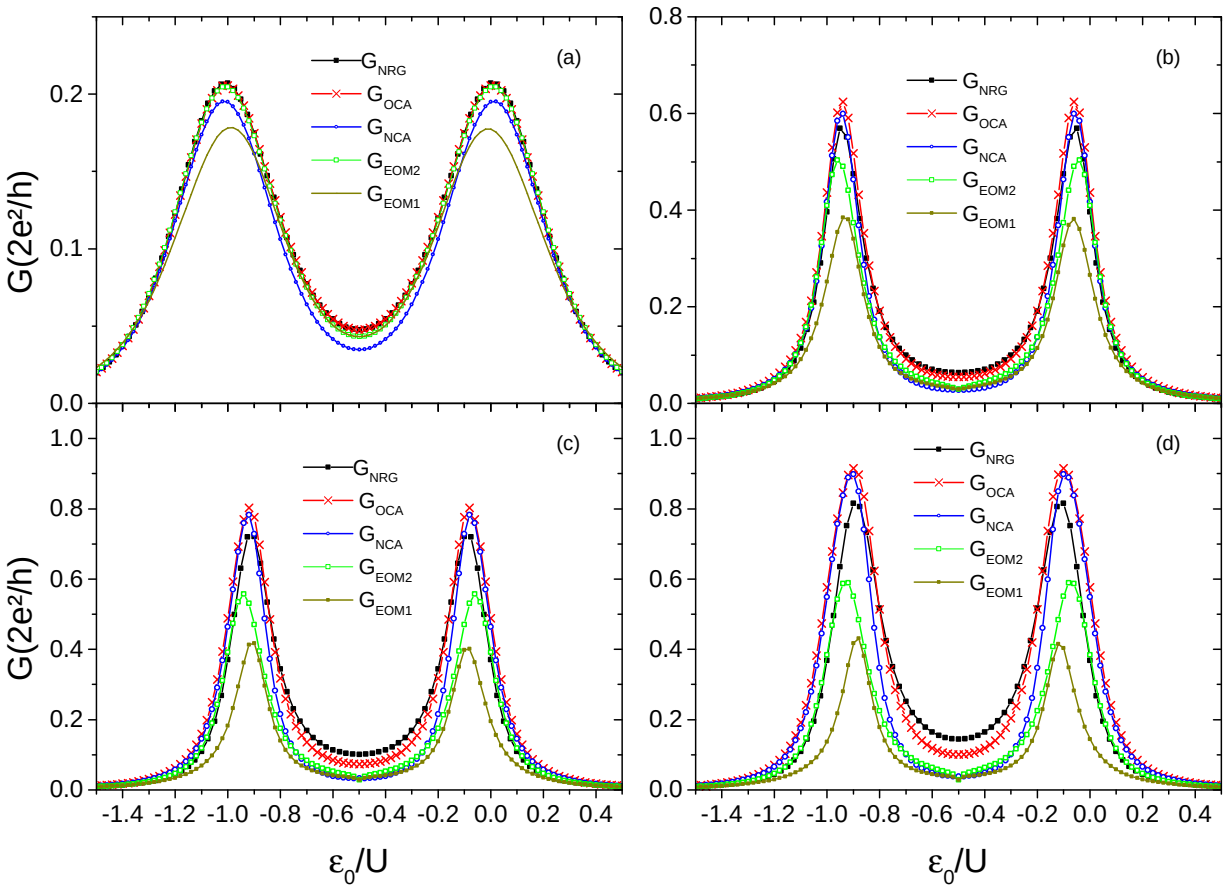

Figure 21: Condutance $\mathcal{G}$ as a function of the single particle energy ε_0 for $\mu = 0$, $\Gamma = 0.1U$, and different values of temperature (a) $T = 0.1U$, (b) $T = 0.01U$, (c) $T = 0.003U$, (d) $T = 0.001U$.

As we decrease the temperature, approaching the Kondo regime, the discrepancies between the results delivered by the different methods become more pronounced. One can clearly observe that the conductance peak heights given by the EOM are consistenly smaller than those given by the SBA or NRG methods, see Figs. 21b, 21c, and 21d.

In order to address the Kondo regime, $T \lesssim T_K$, we increase the coupling strenght to $\Gamma = 0.2U$. In this case the estimated Kondo temperature also increases to $T_K = 0.009U$. This allows us to compute the Green's functions at not too low temperature values, which makes the convergence in NCA and OCA algorithms more difficult. Let us analyze the EOM results. The conductance at mid-valley of both the EOM2 and the EOM1

methods differs significantly from the results of the other approaches, as can be seen in Fig. 22. The well-known increase of the conductance between the peaks as T is decreased, which is a signature of the Kondo effect, is also not reproduced by the EOM schemes. This is a direct consequence of the problems exhibited by both EOM spectral functions, namely the missing of the Kondo resonance at particle-hole symmetric point and the presence of spurious peaks in the asymmetric case (see the previous section). As the temperature is lowered the discrepancy of the EOM1 conductance as compared to the other results becomes more severe. As discussed in the previous section, the EOM1 presents an artificial anti-peak in its density of states in the resonance peak configuration ($\varepsilon_0 = 0$, see Fig. 20) which explains this rather poor performance. We find, as expected, that the method EOM2 improves to some extent the conductance results obtained by the EOM1 scheme. However, the problems in its spectral functions (also discussed in the previous section) seriously compromise the height of the conductance peaks when the temperature decreases, as can be seen in Figs. 22b, 22c, and 22d. We conclude that the EOM approach is not indicated to study neither the low temperature limit nor the Kondo-Coulomb blockade crossover regime in quantum dots. The NCA results show a

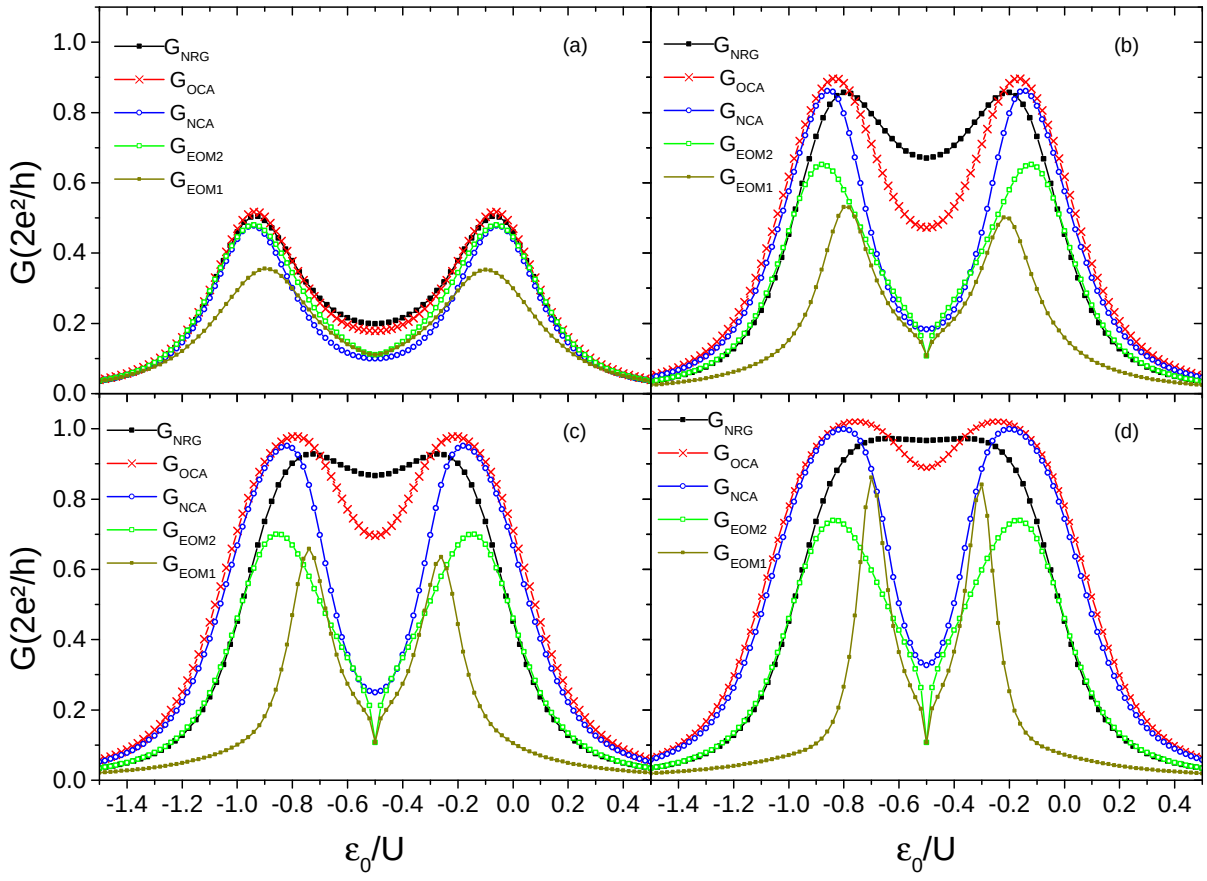

Figure 22: Conductance as a function of the impurity energy level for $\mu = 0$, and for different temperatures. (a)$T = 0.04U$, (b)$T = 0.003U$, (c)$T = 0.001U$, and (d) $T = 0.0004U$. The coupling strength here is $\Gamma = 0.2U$.

discrete increase of the conductance in comparison to the EOM ones. The OCA represents a significant improvement over the NCA conductance. This is a direct consequence of the better agreement of the OCA spectral function with NRG: the Kondo peak in the OCA spectral function is higher and wider than in the NCA one (see the previous section). However, a closer comparison with the NRG result shows that the OCA conductance is still far from developing a perfect Kondo plateau, as can be seen in Fig. 22d.

When the temperature is further decreased, the OCA conductance exhibits a plateau, but it exceeds the quantum of conductance, $G_{\text{plateau}} > 2e^2/h$ as shown in Fig 23. This undesired unphysical feature is related to the violation of limit imposed by the Friedel sum rule which results in the overestimation of the height of the Kondo peak as discussed in the previous section [62].

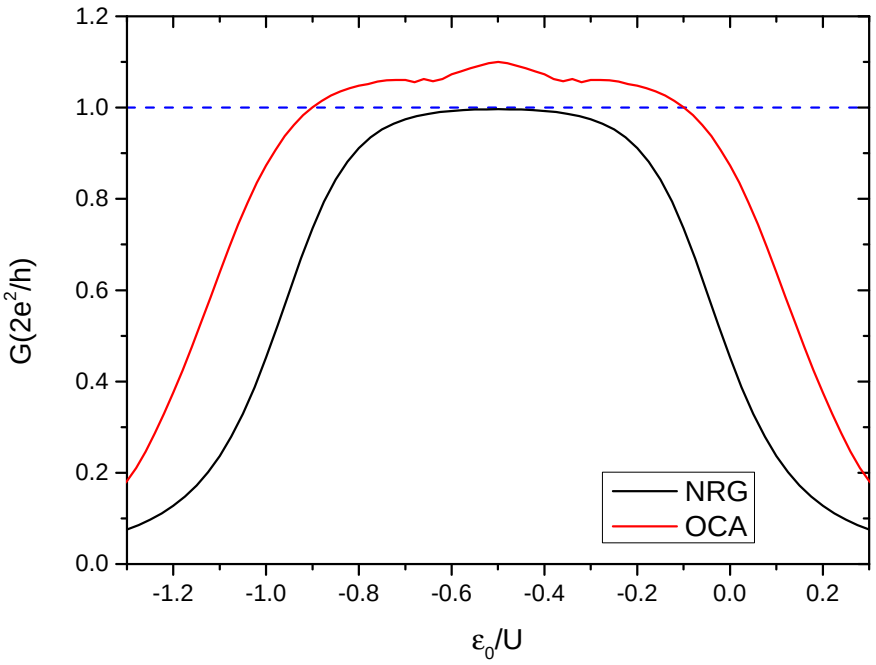

Figure 23: Conductance as a function of the impurity energy level for $\Gamma = 0.2U$,$T = 0.0001U$ calculated using OCA and NRG approaches. The Kondo plateau in the OCA method is above the quantum limit of conductance which is indicated by the blue dashed line. This unphysical feature is a consequence of the overestimation of the Kondo peak height whose correct value is obtained using the Friedel sum rule.

Another problem with NCA and OCA results is the increase of the conductance in the regions $\varepsilon_0 < -U$ and $\varepsilon_0 > 0$ when the temperature is decreased. As shown in Figs. 22d and 24, the NRG conductance over these regions for $T = 0.0004U$ is significantly lower than those calculated using NCA and OCA at the same temperature. This behavior can be understood by looking at the spectral functions in these regions. In Fig. 25 we note that the density of states obtained in the NCA approach exhibits a sharp peak at the

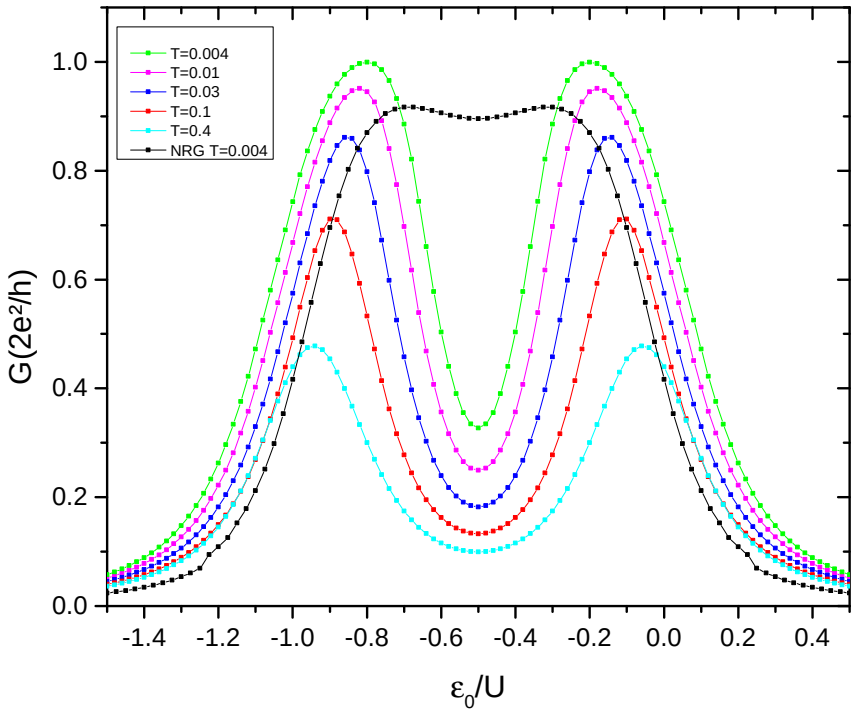

Figure 24: Conductance $\mathcal{G}$ as a function of the single-particle level energy ε_0/U for $\Gamma = 0.2U$. Note the increase of the NCA conductance for $\varepsilon_0 < -U$ and $\varepsilon_0 > 0$, when compared to the NRG result, as temperature decreases.

Fermi level as we pointed out in Fig. 20 and this peak increases when the temperature decreases. In the NRG density of states this peak does not appear. We conclude that the observed increase in the conductance is related to this resonance. It is not clear for us what is the reason behind this resonance appearing in NCA/OCA density of states close to the charge fluctuation points. Possibly it is an artifact of these approximations but at this moment we did not test the accuracy of this statement.

Let us now investigate the temperature dependence of the conductance with more detail. For this purpose we select three different configurations, namely, $\varepsilon_0 + U/2 = 0$, $\varepsilon_0 + U/4 = 0$, and $\varepsilon_0 = 0$. Recalling that we have set $\mu = 0$, the latter cases correspond to the midvalley, a crossover, and the resonance peak configurations, respectively. Figure 26 shows that in the high temperature limit all methods agree very well, as it has been already suggested by Fig. 21a. In the present analysis we do not include the NRG results, which we will discuss in a moment when addressing the scaling behavior of the conductance.

As the temperature decreases, the differences start to appear. In the particle-hole symmetric point, Fig. 26a, both EOM schemes fail dramatically to capture the increase of the conductance due to the missing of the Kondo peak in the spectral function. Those

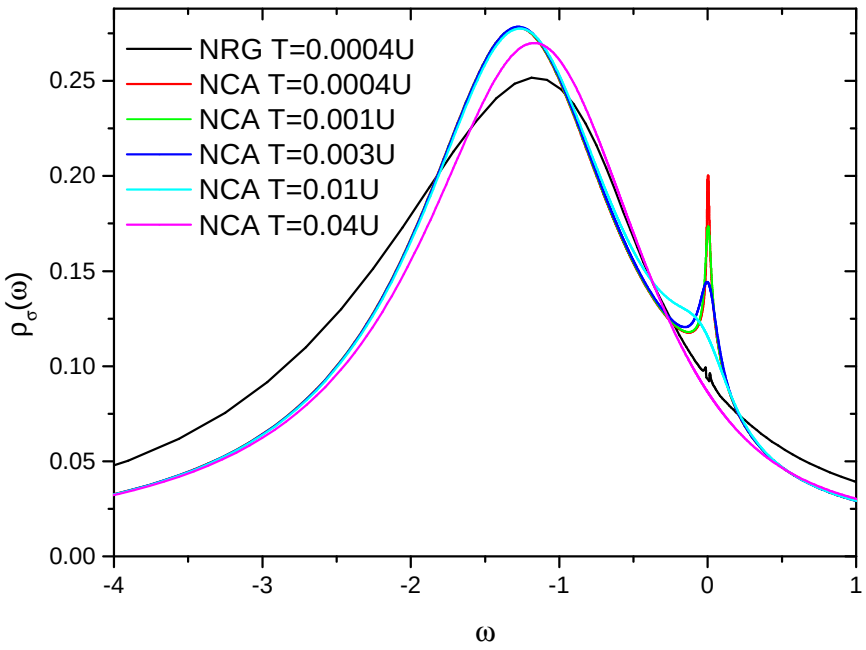

Figure 25: Density of states of the SIAM for $\varepsilon_0 = -1.06U$, $\Gamma = 0.2U$, and different temperatures. Note that in the NCA result there is a resonance at the Fermi energy which does not appear in the NRG result (solid black line). The height of this resonance increases as the temperature decreases.

methods render an almost temperature independent spectral function. The OCA method gives significantly better results than NCA capturing with good accuracy the onset of conductance increase. When the temperature is decreased below about $T_K/10$, the OCA conductance saturates but at an unphysical value, which is greater than the quantum of conductance $G_{\text{plateau}} > 2e^2/h$. When $\varepsilon_0 = -U/4$ and $\varepsilon_0 = 0$, Figs. 26b and 26c, respectively, the EOM1 conductance starts to decrease below a certain temperature. The EOM2 method seems to correct this unexpected behavior to a certain extent, but its already discussed unphysical features prevent the method to yield conductance values close to the OCA/NCA ones. Although we investigated different SIAM configurations, we did not find a clear quantitative criterion to establish the EOM2 validity range.

The analogy between quantum dots and impurity systems extend to the scaling behavior of their properties. Indeed, in Ref. [3] it is experimentally verified that the conductance of a quantum dot depends only on the ratio T/T_K in the low temperature limit.

According to a semi-empirical result obtained by NRG calculations for a spin-1/2, the conductance of a quantum dot is given by [62, 99]

$$\mathcal{G}(T) = \frac{2e^2}{h}\frac{1}{[1+(2^{1/s}-1)(T/T_K)^2]^s} \tag{3.6}$$

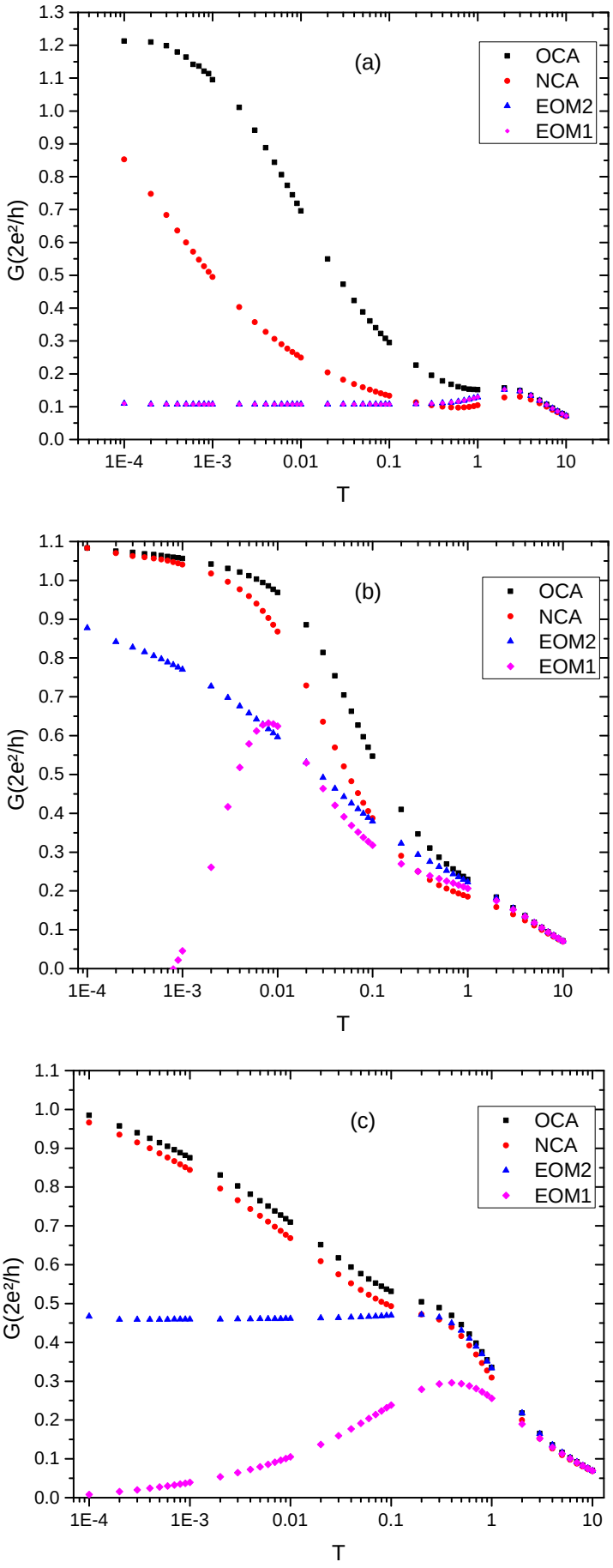

Figure 26: Conductance $\mathcal{G}$ in units of $2e^2/h$ as a function of the temperature T for (a) $\varepsilon_0 = -U/2$, (b) $\varepsilon_0 = -U/4$, (c)$\varepsilon_0 = 0$ corresponding respectively to the midvalley, a crossover, and the resonance peak configuration. Here $\Gamma = 0.2U$.

where $s = 0.22$ [62].

Let us discuss how the scaling behavior is described by the OCA and NCA methods and how it compares with the predicted behavior by the above NRG formula. Firstly, it is important to note that the Kondo temperature given by the OCA method is larger than the one given by NCA (recall that the Kondo peak is wider in OCA than in NCA).

In order to calculate the Kondo temperature for each method we adopted the same procedure used in Ref. [62] which defines T_K as the temperature for which $\mathcal{G}/(2e^2/h) = 1/2$. In this way, we obtained $T_K^{\mathrm{OCA}} \approx 0.0028U$ for the OCA method and $T_K^{\mathrm{NCA}} \approx 0.000097U$ for the NCA solver. Hence the conductance of each method must be scaled by its respective Kondo temperature.

In Fig. 27 we show the conductance as function of T/T_K obtained in NRG, OCA, and NCA methods. Since the OCA method gives unphysical conductance values when $T \lesssim 0.1T_K$, our analysis of the scaling starts from this temperature [62]. Clearly, the scaling obtained using OCA is better than the one yielded by the NCA solver in the sense that the former is closer to the NRG result than the latter. However, as previously reported in Ref. [62], the inclusion of vertex corrections is not enough to recover the NRG prediction.

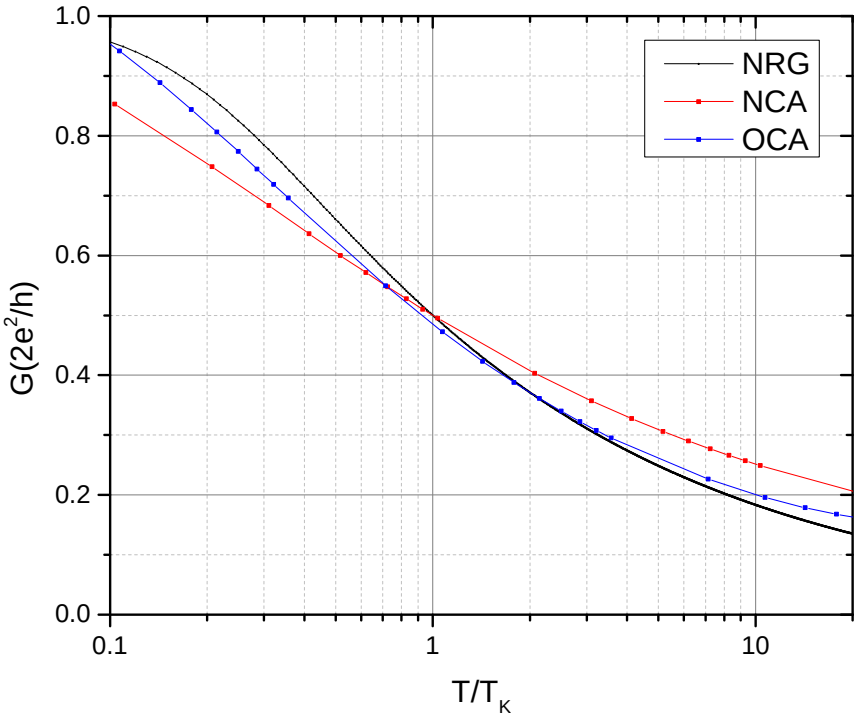

Figure 27: Conductance $\mathcal{G}$ in units of $2e^2/h$ as a function of the scaled temperature T/T_K for $\varepsilon_0 = -U/2$. Here $\Gamma = 0.2U$, $T_K^{\mathrm{OCA}} \approx 0.0028U$, $T_K^{\mathrm{NCA}} \approx 0.000097U$, and $T_K = 0.009U$[Haldane's expression].

In summary, as stated in Ref. [30] there is no solver for the SIAM that can be considered the most appropriate. Often, one needs a combination of them to fully understand many-body problems. As a nice example we mention the work of Ref. [100] where the authors use both EOM and NCA to study low-temperature (nonequilibrium) transport through a quantum dot.

The tests perfomed in this thesis allow us to conclude that to study the SIAM in the high temperature limit, $T \gg T_K$, and close to the particle-hole symmetric point both OCA and NCA as well as EOM2 and EOM1 are appropriate methods giving comparable results. It is worth to stress that if one consider the CPU time to converge the self-consistent solutions only OCA presents a considerable disadvantage in this respect. In the asymmetric case as one approaches the resonance peak configuration, the EOM1 exhibits surprising (and not yet reported) discrepancies compared to the other methods (see Figs. 10 and 11) which makes it an option that can be discarded.

In the particle-hole symmetric Kondo regime, $T \sim T_K$, OCA was the only method to give results close to the NRG ones in the limit $\omega \to 0$. However its drawbacks related to computational time pratically put NRG as the best choice to study the low energy excitations of the SIAM in the Kondo regime. Recall that the used NRG procedure, the CFS-NRG, restrict its calculations to values of energy $|\omega| > T$. In this case one must complement your analysis with the FDM-NRG procedure as discussed in the beginning of the previous section.

The same analysis applies for $T \ll T_K$. Here we add that OCA can be used only for temperatures above $0.1T_K$. Below this value it yields unphysical results for the conductance, violating the unitarity condition and making it totally inappropriate.

EOM schemes are also not suitable to study the Kondo effect in both symmetric and asymmetric case. According to Ref. [59], the missing of the Kondo peak in the particle-hole symmetric point of the SIAM has been reported in many works [101–106].

In the asymmetric case, the inclusion of more correlation terms in the truncation scheme gives some improvements of the EOM2 with respect to EOM1, but fail to fix all unphysical features of the approach. For instance, instead of correcting the spurious resonance, the method enhances it. Hence, the applicability of EOM2 in the Kondo regime is thus restricted to the $U \to \infty$ case only as discussed in Ref. [59]. In this case the spurious peak at $\omega = 2\varepsilon_0 + U$ is pushed away from the conduction band.

Based on the discussion of the previous paragraphs we can summarize the results of

this Chapter in a table like the one shown in Fig. 28.

Method	$T \leq T_K$	$T \sim T_K$	$T > T_K$
EOM0	X	X	X
EOM1	X	X	+−
EOM2	+− *	✓ *	✓
NCA	+−	✓	✓
OCA	✓	✓	✓
NRG	✓	+−	X

* Restricted to the $U \to \infty$ limit

Figure 28: Summary of the performance of each impurity solver for the three temperature regions defined from the characteristic Kondo temperature of the quantum dot.

The EOM0 method have proved to be an inaccurate approach even in the high temperature limit. The EOM1 improves EOM0 result at some extent but still has a poor behavior in the charge fluctuation point when compared to more involved methods. On the other hand, the EOM2 corrects very well the performance of the previous EOM schemes giving consistent results with the ones obtained in the slave boson approches. NRG has a poor performance in spectral functions calculations for $T > T_K$ although it can provide surprisingly accurate results for the conductance. In any case it is safer to use it in the low temperature regime since it was specifically developed to yield accurate results in this very limit.

The crossover region is better addressed by the slave-boson methods, followed by the NRG approach. The EOM2 approach can also be used but only in the $U \to \infty$ limit as explained before. In the Kondo regime, NRG is the best method followed by the OCA, the use of the latter restricted to the temperatures $T \gtrsim 0.1T_K$.

4 Dynamical Mean Field Theory

In the last chapter we studied the accuracy of different solvers for the SIAM on the description of the transport properties of quantum dots. Besides its applicability to study quantum dots and impurities in metals, the SIAM plays an important role on the study of other important strongly correlated systems, such as transition metals and their oxides, heavy fermion compounds, etc.

These materials have open d and f shells in their atoms. Due to the spatial confinement of these orbitals, electrons occupying the latter experience a strong Coulomb repulsion. Hence, band theories based on the independent electron approximation, are not appropriate to address these materials [26,107]. Also the density functional theory (DFT) has proved to be inaccurate to describe many of these d- and f-electron systems [26].The strong interaction which can be comparable to or larger than the kinetic energy makes the problem nonperturbative in nature giving rise to strong electronic correlations and a large plethora of phenomena [30].

The large interest in these materials dates back to the 60's. At that time, the main interest was to understand experiments on transition metal oxides and phenomena like the Mott metal-insulator transition and itinerant ferromagnetism [30]. Since these pioneering investigations the field has expanded a lot: Nowadays one knows that strong correlations in materials are the cause of a huge variety of intriguing phenomena such as the high temperature superconductivity and the colossal magnetoresistance [107]. These are very active subjects in condensed matter physics.

The conventional approach to study such strongly correlated systems has been the proposition and solution of model Hamiltonians. These models drastically reduce the number of degrees of freedom of the problem to the relevant ones involved in a given phenomena. One of the simplest models to account for electron-electron interaction is the

single-band Hubbard model [69]

$$\hat{H} = \sum_{\langle ij\rangle,\sigma} t_{ij} c^{\dagger}_{i\sigma} c_{j\sigma} + H.c. + U \sum_{i} n_{i\uparrow} n_{i\downarrow} \ , \tag{4.1}$$

where $c^{\dagger}_{i\sigma}(c_{i\sigma})$ creates (annihilates) an electron with spin σ at site i, t_{ij} is the hopping between sites i and j, U is the on-site Coulomb interaction, $n_{i\sigma} = c^{\dagger}_{i\sigma} c_{i\sigma}$ is the occupation number and $\langle \cdots \rangle$ means that only nearest neighbors hopping are considered. The kinetic energy is associated with the hopping term and allows the electrons to move in the lattice. The interaction term has an opposite role. It tends to difficult the hopping of electrons, making them localized, since the energy is minimal when they stay as far apart from each other as possible. This competition between itinerant and localized aspects is central to understand strongly correlated systems (SCS) [36, 107].

Despite its simplicity, the Hubbard model has been proved to be very difficult to handle. For a long time its properties were only known for one-dimensional (1D) systems [30,33,108,109]. Analytical progress is challenging since perturbation expansions are only appropriate in two limits of the model: (i) the weak coupling in which the kinetic energy is much larger than the interaction and (ii) the strong coupling where the interaction is much larger than the kinetic energy [26]. However, the SCS fall exactly in the intermediate regime which can not be addressed by perturbative approaches [107].

An interesting breakthrough was reached in 1989: Metzner and Vollhardt [109] have shown that in the limit of infinite dimensions, $d \to \infty$, the study of the Hubbard model becomes much simpler than in finite dimensions. The authors adressed the problem of a cubic lattice of infinite dimensions (hypercubic lattice). They stressed that in order to the kinetic energy and the interaction energy remain of the same order of magnitude in the limit of infinite dimensions, the hopping amplitude must be rescaled properly, namely

$$t_{ij} = \frac{t_*}{\sqrt{2d}} \tag{4.2}$$

This rescaling ensures that in the $d \to \infty$ limit, the DOS remains finite. Using weak-coupling pertubation theory they also showed that , in the $d \to \infty$ limit, the self-energy of the problem is momentum independent, i.e., local in space: $\Sigma_{ij}(i\omega_n) = \delta_{ij}\Sigma(i\omega_n)$. This pioneering work triggered a rapid theoretical development, see for instance Refs. [110–112] in which the Falicov-Kimball model [113–115] and the Kondo lattice model [116] were solved exactly. This line of research culminated in the work of Ref. [117] which puts these previous ideias into a mean-field perspective in a new approach for SCS that would be later called the dynamical mean field theory (DMFT).

DMFT is a theory that replaces a lattice many-body problem with many degrees of freedom by a single-site effective problem. For the Hubbard model the single effective site is modeled by the SIAM. The single site interacts with a bath function which is created from the degrees of freedom in all other sites. This is a powerful method that can address the limiting and intermediate regimes of the ratio U/t in a single framework.

The DMFT equations can be derived by different ways [26, 30]. Here we will only present the main results and equations and the basic ideas leading to them. We refer the reader to the Ref. [30] for a complete derivation.

For the Hubbard model, Eq. (4.1) the partition function can be conveniently written as a functional integral over Grassman variables [118], namely

$$Z = \int \prod_i Dc^\dagger_{i\sigma} Dc_{i\sigma} e^{-S} \ , \tag{4.3}$$

with the action S given by

$$S = \int_0^\beta d\tau \left(\sum_{i\sigma} c^\dagger_{i\sigma} \partial_\tau c_{i\sigma} - \sum_{ij,\sigma} t_{ij} c^\dagger_{i\sigma} c_{j\sigma} - \mu \sum_{i\sigma} c^\dagger_{i\sigma} c_{i\sigma} + U \sum_i n_{i\uparrow} n_{i\downarrow} \right) . \tag{4.4}$$

The idea of DMFT is to find a single-site Z_{eff} and S_{eff}, such that

$$\frac{1}{Z_{\text{eff}}} e^{-S_{\text{eff}}} = \frac{1}{Z} \int \prod_{i \neq o} Dc^\dagger_{i\sigma} Dc_{i\sigma} e^{-S} \tag{4.5}$$

In other words all fermions are integrated out except the one at site o. In the limit of infinite dimensions, the hoppings are rescaled according to Eq. (4.2) and the effective action for the site o reads

$$S_{\text{eff}} = U \int_0^\beta d\tau n_{o\uparrow}(\tau) n_{o\downarrow}(\tau) - \int_0^\beta d\tau \int_0^\beta d\tau' \sum_\sigma c^\dagger_{o\sigma}(\tau) \mathcal{G}_0(\tau - \tau') c_{o\sigma}(\tau') \ . \tag{4.6}$$

$\mathcal{G}_0(\tau - \tau')$ is constructed/obtained by integrating all other degrees of freedom of the lattice. $\mathcal{G}_0(\tau - \tau')$ plays the role of an effetive field and is not known a priori. It represents an amplitude of a process in which an electron hops from the external bath to the site o at a time τ' and leaves the site at a time τ returning to the bath. In this sense, it is said that local temporal fluctuations are captured in this theory although spatial fluctuations are totally frozen. That is why the theory is called *dynamical*. $\mathcal{G}_0$ is not to be confused with the non-interacting Green's function of the Hubbard model (when $U = 0$).

The interacting Green's function of the effetive problem is defined as standard

$$G_{\text{eff}}(\tau-\tau') \equiv -\langle Tc(\tau)c^{\dagger}(\tau')\rangle_{S_{\text{eff}}}$$
$$G_{\text{eff}}(i\omega_n) = \int_0^{\beta} d\tau G_{\text{eff}}(\tau)e^{i\omega_n\tau} \quad , \quad \omega_n \equiv \frac{(2n+1)\pi}{\beta} \tag{4.7}$$

and is connected with the function $\mathcal{G}_0$ by the Dyson equation

$$G_{\text{eff}}^{-1}(i\omega_n) = \mathcal{G}_0^{-1}(i\omega_n) - \Sigma_{\text{eff}}(i\omega_n) \ , \tag{4.8}$$

where $\Sigma_{\text{eff}}(i\omega_n)$ is the self-energy of the effective problem.

4.1 The self-consistency condition

The self-consistency condition establishes the connection between the effective problem and the original lattice problem.

We are interested in the Green's function of the Hubbard model defined by

$$G_{ij}(\tau-\tau') \equiv -\langle Tc_{i,\sigma}(\tau)c_{j,\sigma}^{\dagger}(\tau')\rangle \ . \tag{4.9}$$

The Fourier transform of the above equation is written as [30]

$$G(\mathbf{k}, i\omega_n) = \frac{1}{i\omega_n + \mu - \epsilon_{\mathbf{k}} - \Sigma(i\omega_n)} \ , \tag{4.10}$$

where $\Sigma(i\omega_n)$ is the self-energy due to electron-electron interaction.

One can show that, for the Hubbard model, the bath function $\mathcal{G}_0$ appearing in Eq. (4.6) reads [30]

$$\mathcal{G}_0^{-1}(i\omega_n) = i\omega_n + \mu - \sum_{ij} t_{oi}t_{oj}G_{ij}^{(o)}(i\omega_n) \ . \tag{4.11}$$

In this expression $G_{ij}^{(o)}$ represents the full Green's function of the Hubbard model *with one site removed*. For a general lattice, $G_{ij}^{(o)}$ is given by [30]

$$G_{ij}^{(o)} = G_{ij} - \frac{G_{io}G_{oj}}{G_{oo}} \ . \tag{4.12}$$

Using this result in Eq. (4.11) one has

$$\mathcal{G}_0^{-1}(i\omega_n) = i\omega_n + \mu - \sum_{ij} t_{oi}t_{oj}G_{ij} - \sum_{ij} t_{oi}t_{oj}\frac{G_{io}G_{oj}}{G_{oo}} \ . \tag{4.13}$$

One can simplify the term $\sum_{ij} t_{oi}t_{oj}G_{ij} - (\sum_i t_{oi}G_{io})^2/G_{oo}$ carrying out the following steps:

First one performs a Fourier transform on this expression, next inserts the form in Eq. (4.10) for the lattice Green's function and finally converts the summation in $\mathbf{k}$ into an integral [30]. After performing these steps, one obtains

$$\sum_{ij} t_{oi}t_{oj}G_{ij} - \frac{\left(\sum_i t_{oi}G_{io}\right)^2}{G_{oo}} = \int_{-\infty}^{+\infty} d\epsilon D(\epsilon)\frac{\epsilon^2}{\zeta-\epsilon} - \frac{\left(\int_{-\infty}^{+\infty} d\epsilon D(\epsilon)\frac{\epsilon}{\zeta-\epsilon}\right)^2}{\int_{-\infty}^{+\infty} d\epsilon D(\epsilon)\frac{1}{\zeta-\epsilon}} , \tag{4.14}$$

where

$$\zeta = i\omega_n + \mu - \Sigma(i\omega_n), \tag{4.15}$$

and $D(\epsilon)$ is the density of states of the lattice when $U = 0$. Using the identities [1] [30],

$$\begin{aligned} \int_{-\infty}^{+\infty} d\epsilon D(\epsilon)\frac{\epsilon^2}{\zeta-\epsilon} &= \zeta\int_{-\infty}^{+\infty} d\epsilon D(\epsilon)\frac{\epsilon}{\zeta-\epsilon} , \\ \int_{-\infty}^{+\infty} d\epsilon D(\epsilon)\frac{\epsilon}{\zeta-\epsilon} &= -1 + \zeta\int_{-\infty}^{+\infty} d\epsilon D(\epsilon)\frac{1}{\zeta-\epsilon} , \end{aligned} \tag{4.17}$$

one can write the following relation

$$\mathcal{G}_0^{-1} = \Sigma + 1/\tilde{D}(i\omega_n + \mu - \Sigma(i\omega_n)) . \tag{4.18}$$

In this expression $\tilde{D}[i\omega_n + \mu - \Sigma(i\omega_n)]$ is the Hilbert transform of the argument, namely, $\tilde{D}(z) \equiv \int_{-\infty}^{+\infty} d\epsilon D(\epsilon)/(z-\epsilon)$. It is nothing but the local component of the original lattice Green's function, $G_{ii}(i\omega_n) = \sum_{\mathbf{k}} G(\mathbf{k}, i\omega_n)$, where $G(\mathbf{k}, i\omega_n)$ is given by Eq. (4.10).

By calculating $\Sigma(i\omega_n)$ from the effective problem using Eq.(4.8), we obtain the so-called *self-consistency condition*:

$$G_{\text{eff}}(i\omega_n) = G_{ii}(i\omega_n) = \int d\epsilon \frac{D(\epsilon)}{i\omega_n + \mu - \Sigma(i\omega_n) - \epsilon} . \tag{4.19}$$

Eq. (4.19) ensures that $G_{\text{eff}}(i\omega_n)$ coincides with the site-diagonal Green's function of the lattice model provided that $\Sigma_{\text{eff}}(i\omega_n) = \Sigma_{ii}(i\omega_n)$. Remember that in the limit $d = \infty$ the self-energy is local, i.e., it only depends on frequency, $\Sigma_{ij}(i\omega_n) = \delta_{ij}\Sigma(i\omega_n)$. In order to simplify the notation it is usual to call both $G_{\text{eff}}(i\omega_n)$ and $G_{ii}(i\omega_n)$ simply by $G(i\omega_n)$.

The single-site problem, Eq. (4.6), subjected to the constraint in Eq. (4.19), leads to a closed system of functional equations and fully determines $G(i\omega_n)$ and $\mathcal{G}_0(i\omega_n)$ [30, 119].

[1] The first identity can be derived by using that

$$\frac{\epsilon^2}{\zeta-\epsilon} = \frac{\epsilon^2 - \zeta^2 + \zeta^2}{\zeta-\epsilon} , \tag{4.16}$$

and that $t_{oo} = \sum_{\mathbf{k}} t_{\mathbf{k}} = \int d\epsilon D(\epsilon)\epsilon = 0$ [30]. The second identity follows from a very similar trick.

These equations are exact in the limit $d \to \infty$. For finite dimensions the theory becomes an approximation. The statement that the Green's function of the single site effective problem equals the local Green's function of a lattice in $d = \infty$ have been demonstrated by various authors using perturbation theory in the interaction strength U [26, 30, 109].

It is worth to mention that, in the form presented here, the DMFT equations are valid only if there is no spin or translational symmetry breaking. In the presence of a magnetic field or in order to describe antiferromagnetic phases with two-sublattice long-range order, one needs a generalization of the DMFT equations [119].

The single-site effective problem of the dynamical mean-field theory can be viewed as the problem of a single impurity embedded in a conduction electron bath. In Chapter 1 we note that the problem of a magnetic impurity can be modeled by the Anderson model (SIAM), given by Eq. (1.2) . The action obtained for the impurity by integrating out all the conduction electrons has the form of Eq. (4.6) with

$$\mathcal{G}_0^{-1}(i\omega_n) = i\omega_n + \mu - \int_{-\infty}^{+\infty} d\omega \frac{\Delta(\omega)}{i\omega_n - \omega} \ , \tag{4.20}$$

where

$$\Delta(\omega) = \sum_{\mathbf{k}\alpha} |V_{\mathbf{k}\alpha}|^2 \delta(\omega - \varepsilon_{\mathbf{k}\alpha}) \ . \tag{4.21}$$

Therefore, one can say that the dynamical mean-field theory of the Hubbard model maps the lattice problem onto a single-impurity effective problem coupled to a self-consistent bath, as illustrated by Fig. 29. Indeed, this connection is one of the greatest findings of the theory. The DMFT converts an extremely complicated problem into one for which there are several methods of solution, as discussed in Chapter 2 [11, 14, 60, 120–122].

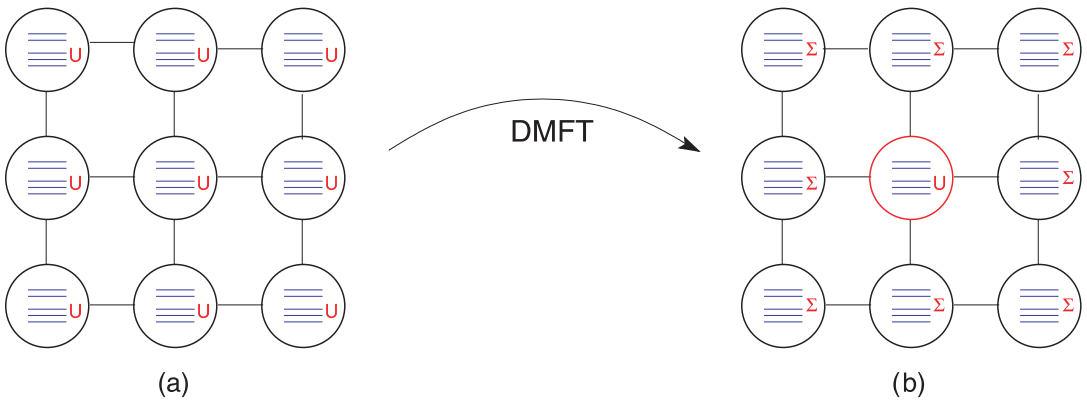

Figure 29: The DMFT maps the lattice problem (a) onto a single impurity problem coupled to an effective medium (b). The effect of the electronic correlations is contained in the self-energy Σ. Extracted from Ref. [26].

The equations of the DMFT are solved by iteration, see the flow chart sketched in Fig. 30. One can start with a initial guess for the effective bath Green's function $\mathcal{G}_0(i\omega_n)$ which is the input for the Anderson model. Next we have to solve the SIAM in order to calculate its Green's function $G_{\rm imp}(i\omega_n)$. Using the Dyson equation, Eq. (4.8), we obtain the self-energy $\Sigma(i\omega_n)$. Next we employ Eq. (4.19) to compute the lattice Green's function. The self-consistent condition states that the impurity Green's function equals the local Green's function. Using Eq. (4.8) again we compute a new bath function and start a new iteration cycle. The problem is iterated until convergence is reached.

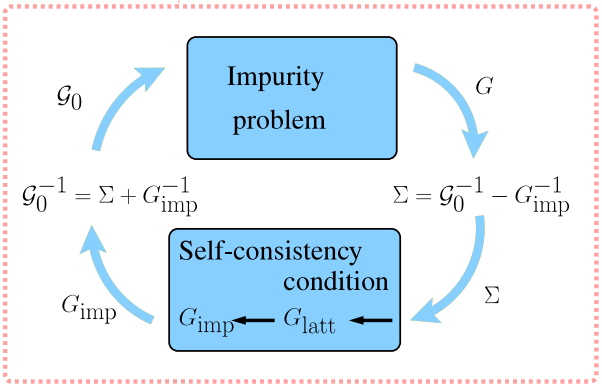

Figure 30: Self-consistent cycle of DMFT. Extracted from Ref. [123].

4.2 Hubbard model for the Bethe and hypercubic lattices

In this section we study the DMFT equations for the Hubbard model applied to a Bethe lattice and a d-dimensional hypercubic lattice, both in the limit $d \to \infty$.

Bethe lattices (also called Cayley trees) are lattices characterized by the number of nearest neighbors $\mathcal{Z}$ of a site, or by its connectivity which is defined as $K = \mathcal{Z} - 1$ [124]. For example, the one dimensional lattice is a Bethe lattice with $\mathcal{Z} = 2$ ($K = 1$). The lattice shown by Fig. (31) is a Bethe lattice with $\mathcal{Z} = 3$ ($K = 2$).

In the limit $\mathcal{Z} \to \infty$, the hopping matrix elements are rescaled as $t_{ij} = t_*/\sqrt{\mathcal{Z}}$ and the density of states assumes a semicircular shape, namely,

$$D(\epsilon) = \begin{cases} \frac{2}{\pi D}\sqrt{1 - \left(\frac{\epsilon}{D}\right)^2} & |\epsilon| < D \\ 0 & |\epsilon| \geq D \end{cases} \tag{4.22}$$

where $D = 2t_*$ is half the bandwidth.

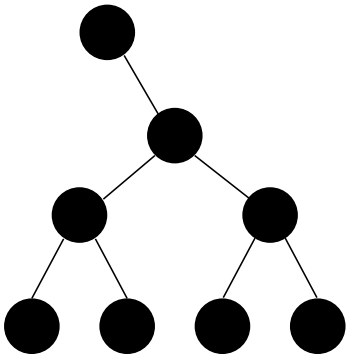

Figure 31: Bethe lattice with $\mathcal{Z} = 3$ and $K = 2$. Extracted from Ref. [125].

The Green's function is computed using Eq. (4.19) and reads [30, 125]

$$G(i\omega_n) = \frac{2}{\zeta + s\sqrt{\zeta^2 - D^2}} \tag{4.23}$$

where $s = \text{sgn}[\text{Im}(\zeta)]$. In this case, the relation between the bath function $\mathcal{G}_0$ and the local Green's function takes a much simpler form, namely

$$\mathcal{G}_0^{-1}(i\omega_n) = i\omega_n + \mu - t_*^2 G(i\omega_n) \ . \tag{4.24}$$

Following the connection with the Anderson model we can identify the last term of this expression with the hybridization function of the SIAM. In other words, it represents the self-energy due to the coupling of the impurity site to the electron bath [125]

$$\Sigma_{\text{hyb}}^{\text{AM}}(i\omega_n) = \sum_{\mathbf{k}\alpha} V_{\mathbf{k}\alpha} \frac{1}{i\omega_n + \mu - \varepsilon_{k\alpha}} V_{\mathbf{k}\alpha}^* = t_*^2 G(i\omega_n) \ . \tag{4.25}$$

For the hypercubic lattice, the density of states assumes a Gaussian form in the limit $d \to \infty$:

$$D(\epsilon) = \frac{1}{t_*\sqrt{\pi}} e^{-\frac{\epsilon^2}{t_*^2}} \ . \tag{4.26}$$

The corresponding Green's function reads

$$G(i\omega_n) = -is\sqrt{\pi} e^{-\zeta} \text{erfc}(-is\zeta) \tag{4.27}$$

where erfc denotes the complementary complex error function [126]. There is no explicit form for the relation between $\mathcal{G}_0$ and G in this case. In this model, one can use Eq. (4.18) to compute a new bath function.

4.3 Successes and limitations of the DMFT

The DMFT has been able to describe many interesting phenomena associated with strong correlations in materials. The description of the metal-insulator (or Mott-Hubbard) transition [27, 28], characteristic of many transition metal oxides and heavy-fermion systems, is one of the first successes of the theory. It was the first method that describe both the strongly correlated metallic phase and the Mott insulator phase in a single framework [30, 37, 119]. According to Ref. [26], the DMFT also contributed to the description of the crossover from Slater to Heisenberg antiferromagnetism and associated metamagnetism, the influence of the lattice and Hund's exchange on ferromagnetism, scattering at impurities or spins, the effects of phonons on the colossal magnetoresistance in manganites, superconductivity, etc. These effects will not be discussed here.

All of these phenomena are captured by taking into account only the local part of electronic correlations. However, according to Ref. [26], short-range and long-range correlations play an important role in a variety of phenomena such as valence bonds, pseudogaps, (possibly) d-wave superconductivy, (para-)magnons, quantum critical behavior, and the critical behavior in the vicinity of phase transitions. Since DMFT neglects non-local correlations completely, one should keep in mind that these effects are not accounted for by the theory. In order to capture the dynamical effects of intersite interactions, extensions of DMFT have been proposed such as the cluster DMFT approach (see Ref. [127]) and the dynamical cluster approximation (DCA) (see Ref. [128]) which we will not discuss here.

5 DMFT - Results

In the last chapter we showed how the dynamical mean-field theory can be used to study the electronic properties of strongly correlated systems for a given many-body Hamiltonian model. The main goal of the theory is the calculation of the site-diagonal (local) Green's function of the model of interest from which one can obtain several properties of the system, namely, the density of states, response functions, transport properties, etc..

In this chapter we present and discuss DMFT results for the density of states of the Hubbard model applied to a hypercubic lattice in the limit $d \to \infty$ at half-filling ($\mu = U/2$). We use OCA, NCA and EOM as impurity solvers and compare the results obtained by each approximation for the paramagnetic case ($G^{\sigma}_{ii} = G^{\bar{\sigma}}_{ii}$). It is important to mention here that for the half-filled case, the EOM1 and EOM2 Green's functions, Eqs. (2.31) and (2.46), respectively, coincide, as explicitly shown in Appendix A. In our calculations we set the hopping t_* as the energy unit, $t_* = 1$.

It is noteworthy that the density of states for all above solvers displays the so-called Mott-Hubbard metal-insulator transition. For $U/t_* \to 0$ the density of states is metallic with a single peak at the Fermi energy. As U increases the central peak gradually decreases, vanishing at some critical value $U_{\rm c}$, whose exact value will not be computed here, giving rise to two bands separated by a pseudo-gap, usually called the lower (LHB) and the upper Hubbard bands (UHB). We compare the overall evolution of the density of states as U is increased and note that there are significant differences between the results obtained by each solver. The main goal of this chapter is to address these differences.

In our study of the Mott-Hubbard transition we always start from a metallic solution. We also first compute the results in the metallic phase $U \to 0$ gradually reaching the insulator regime. In the literature it is usual to address the situation in which one starts from an insulator solution. In general, the two approaches will yield different results for the critical interaction U_c at which the transition occurs [98, 119]. More explicitly, when

one starts with a metallic solution, a critical value $U = U_{c_2}$ is obtained. Starting from an insulator solution will result in another critical value $U = U_{c_1}$ with $U_{c_1} < U_{c_2}$. In this way a region of coexistence is defined in the interval $U_{c_1} < U < U_{c_2}$ [98,119]. In this thesis we only consider the critical value U_{c_2}.

Let us discuss the results for which the density of states is metallic. Firstly, for values of $U \lesssim 1.3$, it was possible to obtain a converged solution for the local Green's function when using both the EOM and the NCA as the impurity solver. Within the U range we fail to obtain a converged solution when we used OCA as the solver. It remains unclear what happens in this limit with the OCA solutions. One possibility is, based on the discussion of Ref. [119], that the converged solution is obtained only when one uses the antiferromagnetic set of DMFT equations for the Hubbard model. In order to achieve convergence in this case, it would be necessary to break translational symmetry of the lattice by defining two sublattices and two corresponding local Green's functions, see discussion in Refs. [30,119]. It is beyond the scope of our analysis to clarify whether this is the real picture and we will not discuss the antiferromagnetic solution here.

Figure 32 shows the density of states for $U = 0.4$ obtained using NCA and EOM, and, for comparison, the non-interacting density of states. The EOM density of states is very similar to the non-interacting one, while in the NCA result we already see a slight deviation from the gaussian shape predicted by Eq. (4.26).

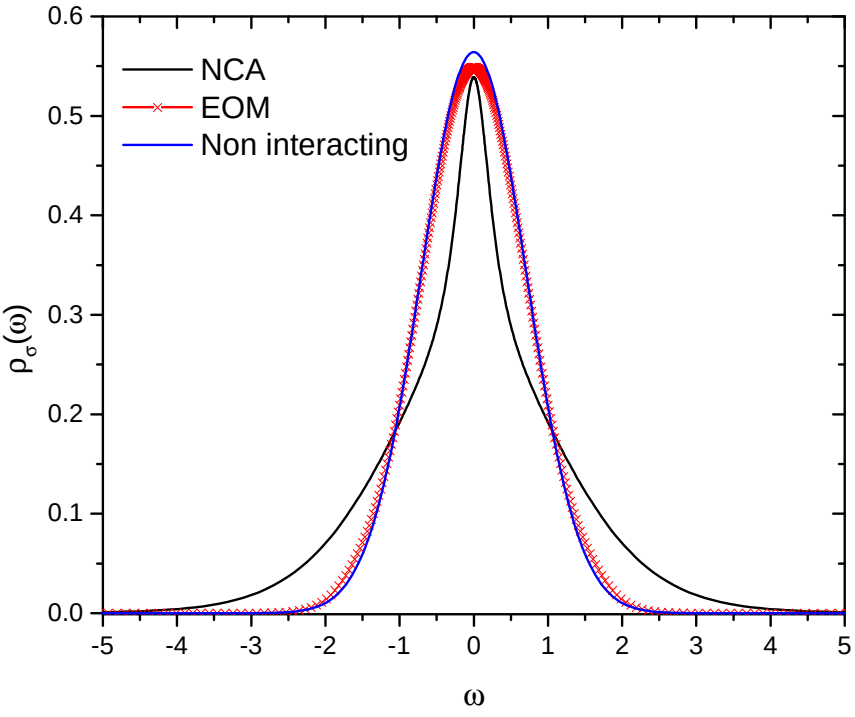

Figure 32: Density of states ρ_σ as a function of the energy ω of the Hubbard model for $U = 0.4$ and $\beta = 7.2$ obtained using NCA and EOM as solvers.

As can be seen in Fig. 33, in the EOM result the effect of increasing the interaction is to reduce the height of the central peak while its shape pratically does not change. On the other hand, the NCA density of states shows significant modifications (as well as OCA, which we will discuss in a moment), as U increases: The height of the central peak decreases and its shape changes considerably (see Fig. 33). More importantly it is possible to note the formation of the two Hubbard bands showing up on each side of a central peak, resembling two shoulders. The central peak can be identified as the Kondo peak [108, 119] and the model is said to be in a strongly correlated metallic phase [30]. The absence of a Kondo peak in the EOM density of states as a direct consequence of the inability of the EOM scheme to describe Kondo correlations, especially in particle-hole symmetric case, as discussed in Chapter 3 [30].

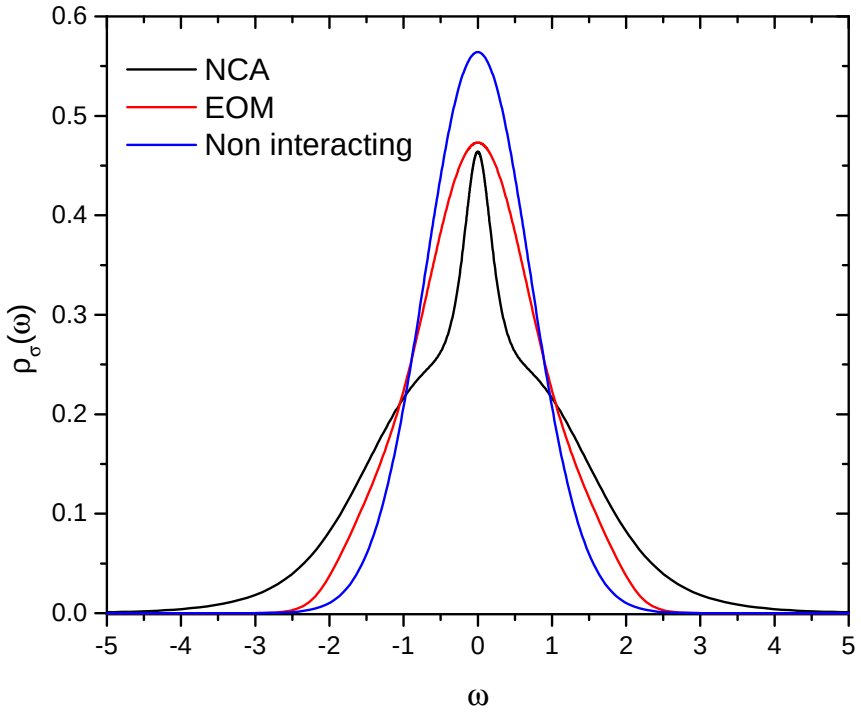

Figure 33: Density of states of ρ_σ as a function of the energy ω of the Hubbard model for $U = 1$ and $\beta = 7.2$ obtained using NCA and EOM as solvers.

In Figures 34 and 35, in addition to EOM and NCA, we also show the density of states for the OCA solver. In these cases where $U \gtrsim 3$ full convergence is attained. One can see that the main effect of OCA is to increase the height and the width of the Kondo peak when compared with the NCA result. A similar effect has been discussed in the case of quantum dots in Chapter 3. In Figure 35 neither the NCA nor the EOM result exhibit the central Kondo peak while the OCA solver displays it. Also note how the Hubbard bands are easier to distinguish from the central peak in the OCA result.

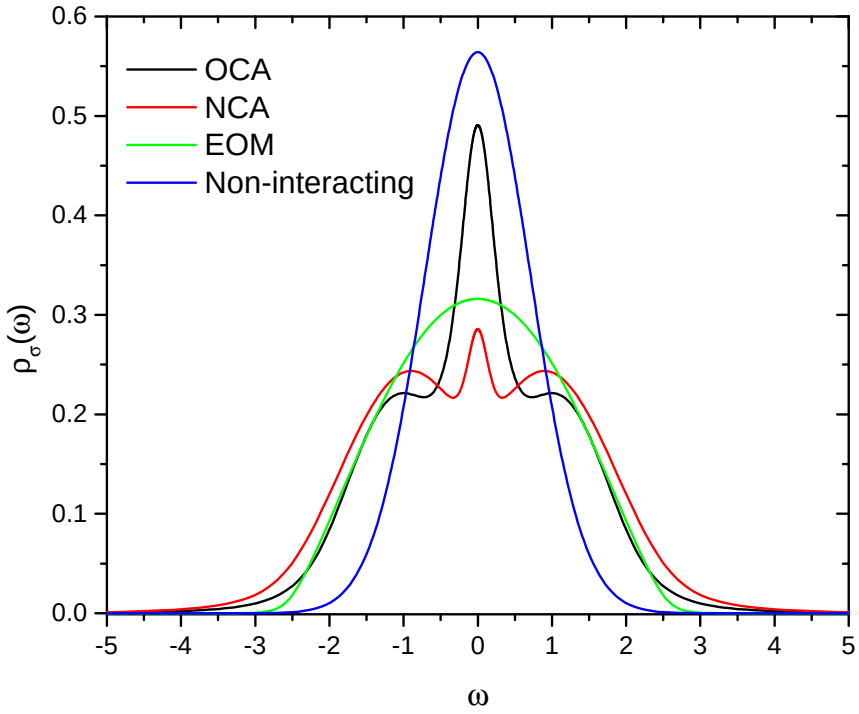

Figure 34: Density of states ρ_σ as a function of the energy ω of the Hubbard model for $U = 1.7$ and $\beta = 7.2$ obtained using OCA, NCA and EOM as solvers.

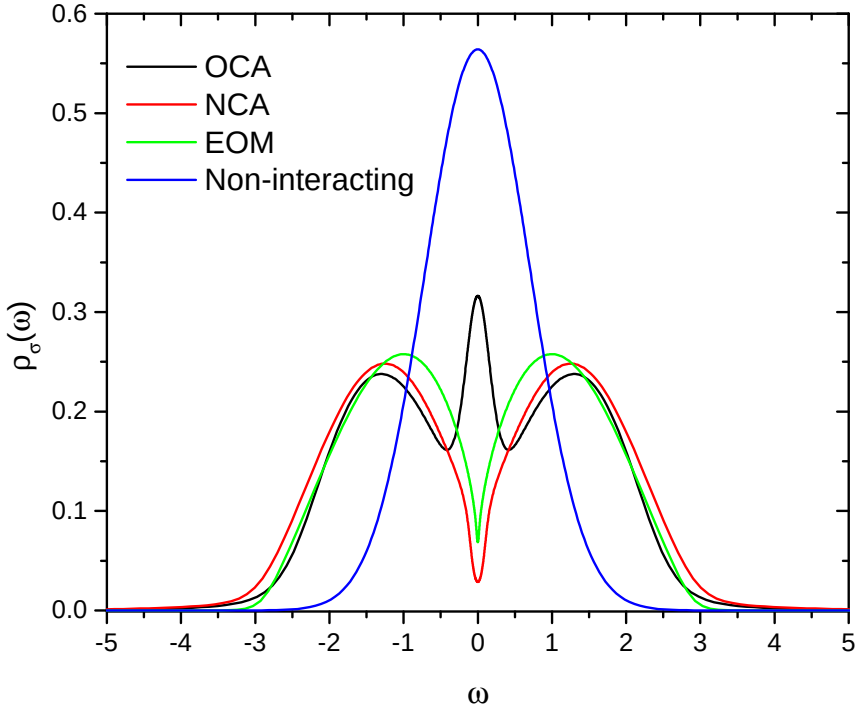

Figure 35: Density of states ρ_σ as a function of the energy ω of the Hubbard model for $U = 2.4$ and $\beta = 7.2$ obtained using OCA, NCA and EOM as solvers.

Let us discuss now the results for the insulating phase. As shown in Fig. 36, all the density of states, obtained by the different methods, display a remarkable good qualitative agreement even for the EOM solver. The upper and lower Hubbard bands have similar shapes and the distance between the centers of each band is approximately given by

the Coulomb interaction U. One could conjecture that this performance of EOM in the insulator phase has to do with the fact that, since there is no Kondo peak and, hence, no signature of Kondo correlations taking place, it is expected that EOM should yield good result. This also means that, in the atomic limit correlations giving rise to the quasi-particles near the Fermi energy are reduced. We stress that the most significant difference between the results obtained by using distinct impurity solvers is related to the size of the pseudogap. Most notably in OCA the pseudogap is smaller than the ones obtained using the NCA and EOM impurity solvers. In the Ref. [98] the authors compared OCA with the quantum Monte Carlo method for a Bethe lattice and also noticed a similar feature. The authors traced the observed discrepancy to the underestimation of the second moment in the high-frequency expansion of the Green's function, discussed in Ref. [129]. However, the critical value of $U = U_{c_2}$ at which the quasiparticle peak disappears and the pseudogap opens shows good agreement with the result obtained by the QMC [98].

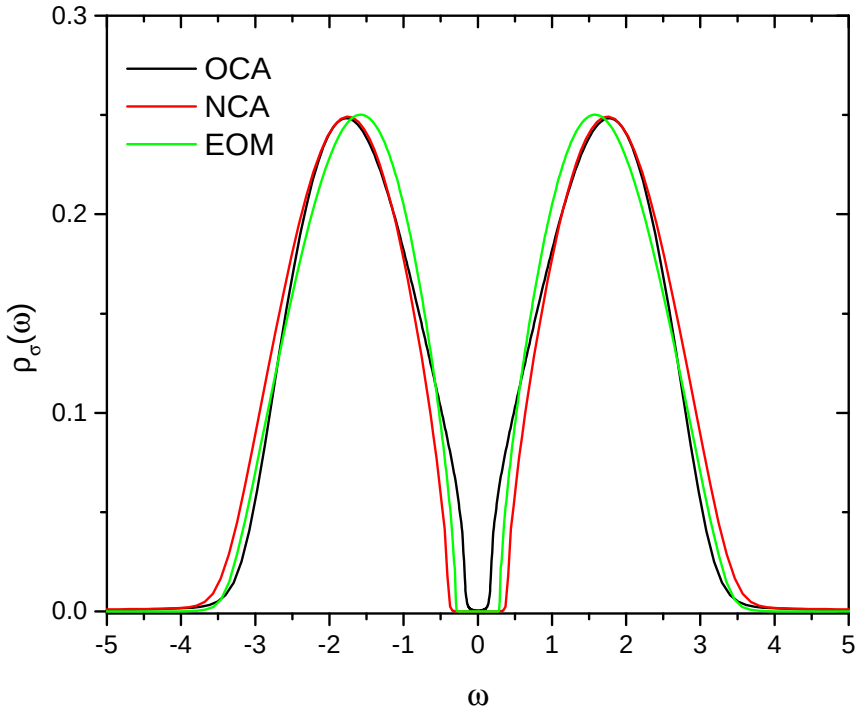

Figure 36: Density of states ρ_σ as a function of the energy ω of the Hubbard model for $U = 3.4$ and $\beta = 7.2$ obtained using OCA, NCA and EOM as solvers.

The figures 37, 38, and 39 show a countour plot of the density of states ρ_σ as a function of ω and U obtained using the OCA, NCA, and EOM solvers, respectively, for $\beta = 1/T = 7.2$. The overall evolution of the density of states allows us to conclude that the inclusion of vertex corrections in NCA has interesting consequences. Firstly, as we already discussed, for values of $U \lesssim 1.3$, the OCA method does not yield a converged solution and we mention the speculation that in this case the solution is antiferromagnetic [30, 119].

It is also evident from these contour plots that the quasiparticle peaks are higher and wider in OCA than in NCA. Another important effect of the vertex corrections is related to value of U at which the (pseudo)gap opens. In the OCA result the critical interaction U_{c_2} is larger than the value obtained by the NCA method. Inspired by the vastly stressed idea that the competition between the band and atomic limits is at the very heart of the strongly correlated systems, we speculate that the larger U_c observed in OCA as compared to NCA is due to the following: Since OCA includes more processes (and with higher complexity) in which the electron leaves the impurity site going to the bath (hopping processes), unless there is an accidental cancelation of scattering amplitudes a larger U is necessary to compensate for the increase of such transitions. In other words, a larger U_c is related to the fact that OCA captures more correlations than NCA in its description of the SIAM. The inclusion of more hopping processes favors the metallic character of the DOS, then it is necessary to increase U in order to favor the insulator character of the DOS. This is a manifestation of the competition between itinerant and localized aspects, as discussed in Chapter 4.

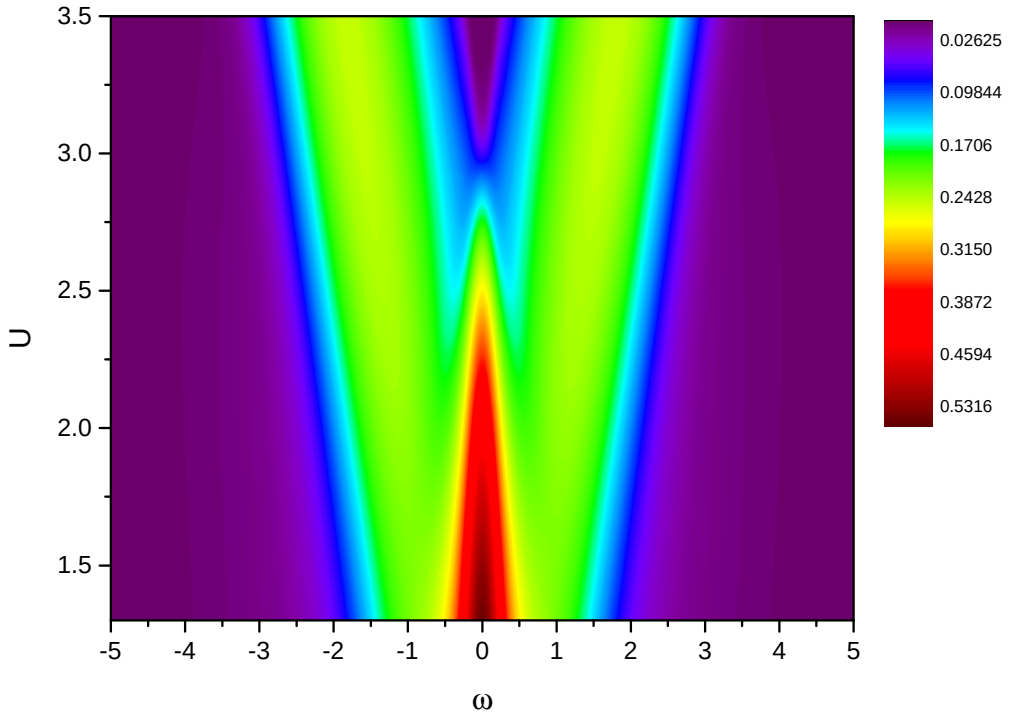

Figure 37: Contour plot of the OCA density of states as a function of U and ω for the half-filled Hubbard model (hypercubic lattice) and $\beta = 7.2$.

In the EOM contour plot, Fig. 39, one can note that for $U \lesssim 2$ there is a flat and featureless peak approaching the non interacting gaussian DOS, indicating that the EOM method does not yield an accurate description of the metallic phase of the model. On the other hand, in the insulating part, the main feature which is the appearance of the two

Hubbard bands is well captured by the method and the results are in good agreement with the OCA and NCA approaches. The centers of the upper and lower Hubbard bands approximately coincide with the points of the straight lines $U(\omega) = 2\omega$ and $U(\omega) = -2\omega$, respectively, indicating that the separation between the two bands is governed by the interaction, as expected.

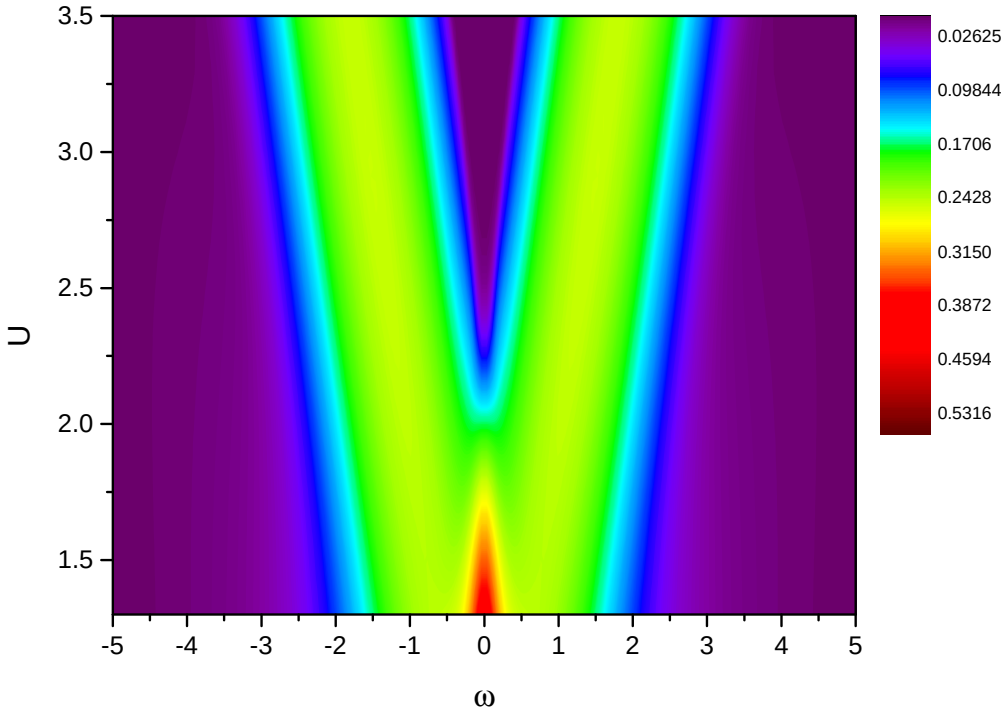

Figure 38: Contour plot of the NCA density of states as a function of U and ω for the half-filled Hubbard model (hypercubic lattice) and for $\beta = 7.2$.

Let us briefly comment on the computational cost of the methods. This is an important issue since in every iteration of the DMFT loop showed in Fig. 30 one must run the impurity solver. Furthermore, the convergence of the DMFT self-consistency condition is considerably slower close to the metal-insulator transition requiring more iterations. In the case of NCA and OCA this means that in each cycle the set of self-consistent equations of these methods must be solved, see Chapter 2. We run a DMFT calculation for $U = 2$, $\beta = 7.2$, and $N = 846$ points in the pseudo-particle mesh using 12 cores (see footnote at page 58). In this case, NCA spent 10.6 minutes in 83 iterations, while OCA took 674.9 minutes to converge in 55 iterations. Based on this performance and the discussion in the Chapter 3 it is clear that the use of OCA as a solver demands an implementation with parallel computing using as many CPU cores as possible since it spends a lot of time to calculate the spectral function.

Now we believe that a discussion about the applicability of each solver studied in this Chapter is in order. We recall that the dynamical mean field theory is a method that is concerned with the whole energy range of the model spectra [30]. However no solver

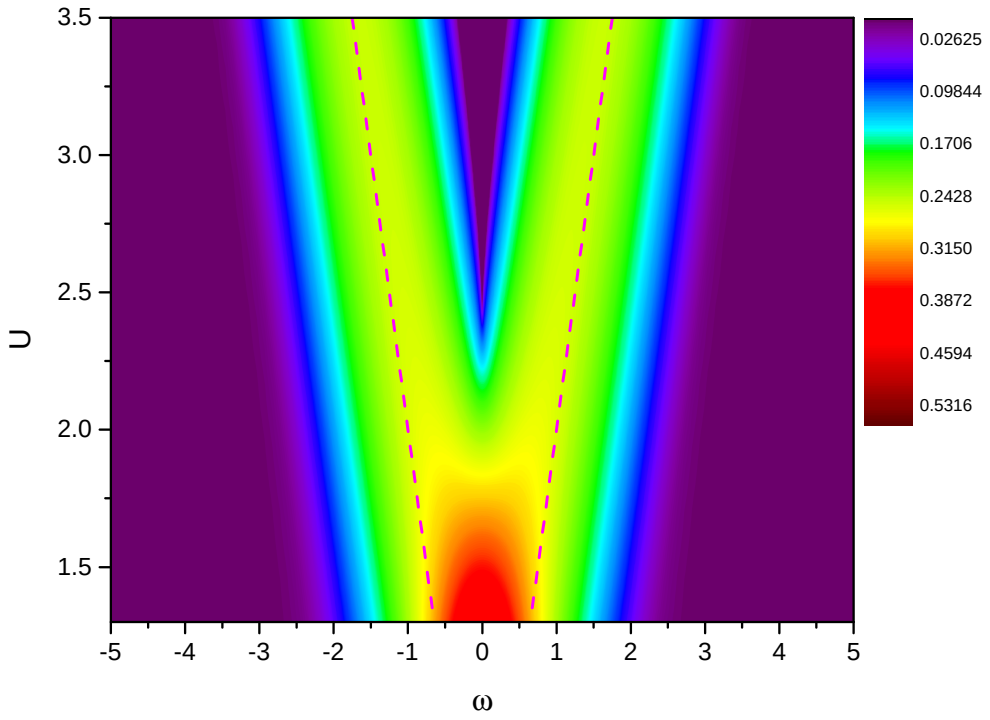

Figure 39: Contour plot of the EOM density of states as a function of U and ω for the half-filled Hubbard model (hypercubic lattice) and for $\beta = 7.2$. The dashed lines represent the curves $U(\omega) = \pm 2\omega$. The center of the two Hubbard bands approximately coincides with the points of these straight lines, indicating that the separation between the Hubbard bands is given by the interaction U.

can yield accurate results for the whole range of energies and parameters. For instance, the numerical renormalization group approach is tradicionally known for providing better results for low energy excitations [30]. The quantum Monte Carlo method (QMC) is computationally expensive, its calculations are performed on the imaginary time axis requiring analytical continuation to the real axis. On the other hand OCA, NCA, and EOM have the advantage of giving results directly on the real axis [98]. Furthermore both NRG and QMC methods present some difficulties in the case of large orbital degeneracy of the correlated shell [36, 98].

In Chapter 3 we discussed the performance exhibited by EOM, NCA, and OCA methods in the description of the Coulomb blockade and Kondo physics of a quantum dot. It is clear from the results presented in this chapter that the shortcomings these methods present in the context of a single impurity influence the performance of the methods in the context of DMFT. The non crossing approximation severely underestimates the Kondo energy scale while OCA improves NCA estimative giving the correct order of magnitude of T_K. However, OCA overestimates the height of the Kondo resonance for suficiently low temperatures. Despite these drawbacks both solvers have been successfully used in both

DMFT and in combination with *ab initio*+DMFT calculations to describe the most essential features of several strongly correlated materials yielding results in good agreement with experiments as reported in the literature [36, 130, 131]. In general the NCA method can be considered a reliable approximation at half filling, for U large and for $T > t_*/40$ according to Ref. [132]. Moreover its accuracy increases in the $U \to \infty$ limit with large orbital degeneracy according to Ref. [38]. Both NCA and OCA yield better results for the high energy region of the spectra being especially more accurate for the insulating regimes [133, 134]. However since OCA presents a good compromise between accuracy and computational effort [38] it has been used in many works being capable of giving reasonable results for spectral densities both in the high and low energy regions of the spectrum especially for not too low temperatures, $T \gtrsim 0.1T_K$, [38, 98, 135]. According to Ref. [87] OCA was very useful in describing features like the crossover between itinerant and localized regimes in Ce-111 materials, the mixed valence state in Pu, transport properties in titanides, the α to γ transition in Ce, as reported in Refs. [136–138]. However it is stressed that OCA needs to be used with care especially for systems with only moderate correlation [87]. One also must be aware of the sum rule violations OCA exhibits in the high frequency expansion of the Green's which are especially worse in the case of the multi-orbital version as discussed in Ref. [129].

Some progresses have been made in extending the OCA approach to include more diagrams in the hybridization expansion in order to improve its description of the low energy excitations of the spectrum. As reported in Refs. [36, 38, 87] different methods like SUNCA, FNCA, CA1 have presented exciting performances when compared to the more accurate Monte Carlo and NRG approaches, nevertheless at the cost of more computational effort. We believe that the increase of the computational resources may contribute to a more and more utilization of these methods in the next years.

The good performance of EOM method in the insulator phases reinforces its applicability only for the strongly interacting limit $U \gg t$ [30, 119, 139], which is the case of rare-earth systems [139]. The EOM method can also be used to yield qualitative results if one is interested only on the high energy spectrum, for instance, for spectroscopic purposes [30, 139, 140].

In Fig. 40 we show the metal insulator transition seen from a perspective tradicionally presented in the literature just to complement the discussion developed in the previous paragraphs.

Finally, in Fig. 41, we summarize the performance of the used impurity solvers in the

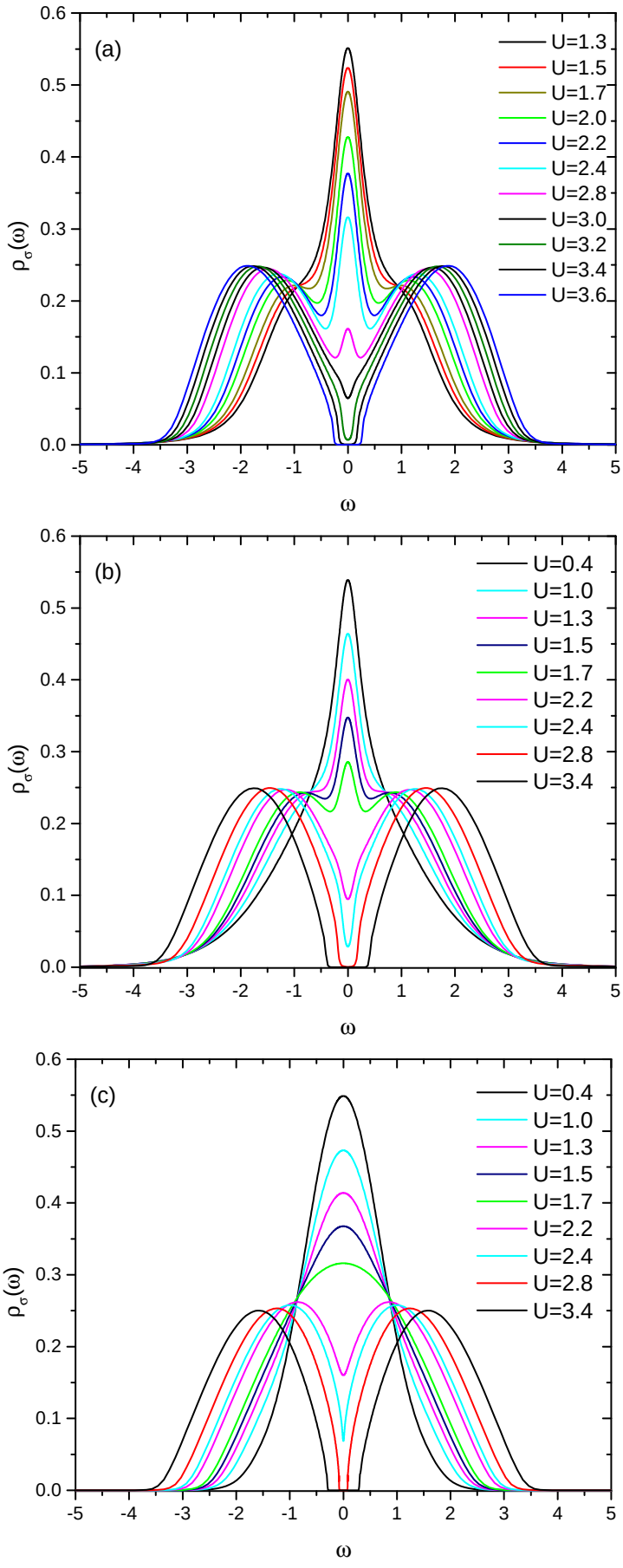

Figure 40: Evolution of the density of states for the Hubbard model in a hypercubic lattice in the limit of infinite dimensions for different values of the interaction U and for $\beta = 1/T = 7.2$ obtained using (a) OCA, (b) NCA, and (c) EOM methods.

three main regions of the Mott transition. According to the discussion of the previous paragraphs all used impurity solvers (OCA, NCA, and EOM) have a good performance in the insulator phase. Near the metal-insulator transition, OCA is the best method while both NCA and EOM give inaccurate results. For $U < U_c$ the EOM solver is completely inappropriate to address the strongly correlated metal. OCA has the best accuracy and NCA can yield, at most, qualitative results.

Method	$U < U_c$	$U \sim U_c$	$U > U_c$
EOM	X	X	✓
NCA	+−	X	✓
OCA	✓	✓	✓

Figure 41: Summary of the performance of each impurity solver for the three main regions of the Mott transition: the metallic phase ($U < U_c$), close to the transition ($U \sim U_c$), and the insulating phase ($U > U_c$).

6 Conclusions

In this thesis we showed by means of several examples the importance of the single impurity Anderson model (SIAM) for the description of a wide variety of strongly correlated systems. Originally proposed to study diluted magnetic impurities in metal alloys, the SIAM has become the standard model to study the effects of strong correlations in heavy-fermion systems, superconductors, transition metal oxides, quantum dots, and more recently, molecular electronic devices with magnetic atoms through DFT+DMFT based transport calculations.

Given its growing importance and protagonism in several contexts of many-body physics, it became also important to search accurate and efficient methods of solution capable of providing the relevant quantities for the different specific problems such as critical exponentes, Green's functions, response functions, optical and transport properties, etc..

In this journey many impurity solvers were proposed [7, 30]. However, as we showed, there is no universal method that can give reliable results in all parameter range of the model. In many cases we find that more than one method can be applied and one has to weight their accuracy and computational cost. In this thesis we assess the reliability of the EOM, SBA, and NRG methods in giving the correct description of the problem in two contexts, namely, in the study of quantum dots and in the study of a lattice many-body problem using a model Hamiltonian (the Hubbard model) solved using the Dynamical Mean Field Theory.

In Chapter 2 we presented the main steps involved in the calculations of the (impurity) local Green's functions for various EOM schemes, and also, for the OCA and NCA methods.

In Chapter 3 we applied these methods to calculate the density of states (DOS) and the linear conductance of a quantum dot symmetrically coupled to two leads in the wide band approximation. We found that in the high temperature limit, OCA, NCA, EOM2, and EOM1 give remarkable close results for the spectral functions in the symmetrical

case. The NRG density of states suffers from artifacts related to the numerical procedures used. Surprisingly, our calculations show that the EOM1 and the simpler EOM0 approaches give very poor results for the SIAM at the charge fluctuation points. We also calculate the conductance and found that NRG, OCA, and EOM2 results show an excellent agreement. NCA is less accurate in the high temperature limit than previously believed. Despite providing a proper description of the characteristic Coulomb blockade physics for $T \gg T_K$, NRG is not a good choice. For technical reasons, NRG calculations become increasingly impractical for increasing T. We observe that OCA requires a very large computational time when compared with other methods, something that makes it attractive only in a heavy computing parallelization scenario. The EOM1 conductance displayed a disappointing performance in this limit, which is intimately related to the poor result obtained in the spectral function calculation with this procedure.

In the low temperature limit, the EOM spectral functions fail dramatically in capturing the correct Kondo physics characteristics. In the symmetric case, due to symmetry constraints, the spectral functions does not display the Kondo peak. In the asymmetric case there is a sharp peak at the Fermi level, however there is also an spurious peak at $\omega = 2\varepsilon_0 + U$ which is an artifact of the truncation. NCA, OCA and NRG have (in this order) growing accuracy in capturing the correct Kondo resonance. We verified the known results in the literature that OCA corrects the deficiencies presented in NCA, mainly the height and the width of the Kondo peak. We also studied the deficiencies presented in OCA below $T < T_K$ [62, 130], namely, a slight overestimation of the height of the Kondo peak. As tradicionally reported, the NRG is the best method to describe the low energy regions of the spectra. It is worth to emphasize, however, that for multiorbital systems NRG present serious difficulties, and in this case OCA is often quoted in the literature as the best cost/accuracy choice [38, 98]. We also find that OCA improves the NCA scaling behavior of the conductance expected from Fermi-liquid calculations for $T \lesssim T_K$ in the symmetric Anderson model.

In Chapter 4 we presented the basic equations and ideas of the Dynamical Mean Field Theory in the limit of infinite dimensions. We saw how a lattice many-body problem can be mapped into a problem of a single interacting site coupled to an effective bath representing all degrees of freedom of the other sites. We reviewed how the original lattice problem and the single impurity effective problem are connected by means of a self-consistency condition, and how the equations can be solved in an iterative manner. Next we study the specific equations for the Bethe and hypercubic lattices both in the limit of large coordination number, and showed how they simplify in analytical closed

expressions in these cases.

In Chapter 5 we applied the DMFT to study an hypercubic lattice modeled by the Hubbard model in the $d \to \infty$ limit using EOM, NCA, OCA as solvers in the particle-hole symmetric case. We verified that all of them capture the Mott-Hubbard transition as vastly reported in the literature [30,36]. We calculate the spectral function and presented our results in a contour plot to give a broad picture of the transition occurring in the density of states. We noticed that OCA gives a transition at a higher and more accurate value of U as compared with NCA and EOM. We also showed that EOM gives a bad description of the metallic phase, a result that is also reported in the literature [30]. Obviously this is intimately related to the lack of a proper description of correlations characteristic of the EOM schemes.

The task of benchmarking impurity solvers is far from being finished. The use of fast approximate techniques and algorithms favors the progress in the exploration of complex problems [36]. However, it is always a good practice to compare the results of a given solver with more exact methods and with experimental results in order to validate the chosen approach [36]. In view of the huge variety of scenarios in which strong correlations are present, specifically in the very active field of molecular electronics, where experiments are reporting correlation effects in different materials [19,20], the demands for a combination of accuracy and efficiency tend to increase. As such, studies in this line will continue to be important to achieve a deep understanding relating theory and experiments in the exploration of new complex materials.

Appendix A – EOM Green's functions in the particle-hole symmetric case

Let us recall from Chapter 2 that the EOM1 Green's function is given by

$$G_\sigma(\omega) = \frac{\omega - \varepsilon_\sigma - U(1 - \langle n_{\bar{\sigma}} \rangle) - \Sigma_0(\omega) - \Sigma_3(\omega)}{[\omega - \varepsilon_\sigma - \Sigma_0(\omega)][\omega - \varepsilon_\sigma - U - \Sigma_0(\omega) - \Sigma_3(\omega)] + U\Sigma_1(\omega)} \ , \tag{A.1}$$

where $\Sigma_0(\omega)$ is the embedding self-energy, namely,

$$\Sigma_0(\omega) = \sum_{\mathbf{q}\beta} \frac{|V_{\mathbf{q}\beta}|^2}{\omega - \varepsilon_{\mathbf{q}\beta}} \ , \tag{A.2}$$

while the self-energies $\Sigma_1(\omega)$ and $\Sigma_3(\omega)$ are given by

$$\Sigma_i(\omega) = \sum_{\mathbf{q}\beta} A^{(i)}_{\mathbf{q}\beta} |V_{\mathbf{q}\beta}|^2 \left[\frac{1}{\omega + \varepsilon_{\mathbf{q}\beta} - \varepsilon_{\bar{\sigma}} - \varepsilon_\sigma - U} + \frac{1}{\omega - \varepsilon_{\mathbf{q}\beta} + \varepsilon_{\bar{\sigma}} - \varepsilon_\sigma} \right] \ , \tag{A.3}$$

with $A^{(1)}_{\mathbf{q}\beta} = f(\varepsilon_{\mathbf{q}\beta})$ and $A^{(3)}_{\mathbf{q}\beta} = 1$. In the symmetric case for a non-magnetic solution $\varepsilon_{\bar{\sigma}} = \varepsilon_\sigma$, one has $2\varepsilon_0 + U = 0$. Hence the self-energies of Eq. (A.3) can be simplified to

$$\Sigma_i(\omega) = \sum_{\mathbf{q}\beta} A^{(i)}_{\mathbf{q}\beta} |V_{\mathbf{q}\beta}|^2 \left[\frac{1}{\omega + \varepsilon_{\mathbf{q}\beta}} + \frac{1}{\omega - \varepsilon_{\mathbf{q}\beta}} \right] \ . \tag{A.4}$$

As usual, the summation in momenta can be converted into an integral. This yields

$$\Sigma_0(\omega) = \frac{1}{2\pi} \sum_\beta \int d\varepsilon_\beta \frac{\Gamma^\beta(\varepsilon_\beta)}{\omega - \varepsilon_\beta} \ , \tag{A.5}$$

$$\Sigma_i(\omega) = \frac{1}{2\pi} \sum_\beta \int d\varepsilon_\beta \Gamma^\beta(\varepsilon_\beta) A^{(i)}(\varepsilon_\beta) \left[\frac{1}{\omega + \varepsilon_\beta} + \frac{1}{\omega - \varepsilon_\beta} \right] \ , \tag{A.6}$$

where Γ^β is the partial decay width given by

$$\Gamma^\beta(\varepsilon_\beta) \equiv 2\pi |V_\beta|^2 \rho(\varepsilon_\beta) \ , \tag{A.7}$$

and $\rho(\varepsilon_\beta)$ is the density of states of the lead β

A.1 Proof of the equality $\Sigma_1(\omega) = \Sigma_0(\omega)$

According to the Eq. (A.6) the self-energy $\Sigma_1(\omega)$ can be written as

$$\Sigma_1(\omega) = \frac{1}{2\pi}\sum_{\beta}\int d\varepsilon_\beta \Gamma^\beta(\varepsilon_\beta) f(\varepsilon_\beta)\left[\frac{1}{\omega+\varepsilon_\beta}+\frac{1}{\omega-\varepsilon_\beta}\right]. \tag{A.8}$$

In the first integral we introduce a change of variable $\varepsilon_\beta = -\varepsilon'_\beta$, yielding to

$$\Sigma_1(\omega) = \frac{1}{2\pi}\sum_{\beta}\left[\int d\varepsilon_\beta \frac{\Gamma^\beta(-\varepsilon_\beta) f(-\varepsilon_\beta)}{\omega-\varepsilon_\beta}+\int d\varepsilon_\beta \frac{\Gamma^\beta(\varepsilon_\beta) f(\varepsilon_\beta)}{\omega-\varepsilon_\beta}\right]. \tag{A.9}$$

Using the identity $f(-\varepsilon_\beta) = 1 - f(\varepsilon_\beta)$ and that the coupling strength is an even function of the energy, $\Gamma^\beta(\varepsilon_\beta) = \Gamma^\beta(-\varepsilon_\beta)$, we arrive at

$$\Sigma_1(\omega) = \frac{1}{2\pi}\sum_{\beta}\int d\varepsilon_\beta \frac{\Gamma^\beta(\varepsilon_\beta)}{\omega-\varepsilon_\beta}\,, \tag{A.10}$$

which coincides with Eq. (A.5). Therefore, we conclude that

$$\Sigma_1(\omega) = \Sigma_0(\omega)\,, \tag{A.11}$$

which is temperature independent, as pointed out in Ref. [67].

A.2 Proof of the equality $\Sigma_3(\omega) = 2\Sigma_0(\omega)$

According to Eq. (A.6) the self-energy $\Sigma_3(\omega)$ can be written as

$$\Sigma_3(\omega) = \frac{1}{2\pi}\sum_{\beta}\int d\varepsilon_\beta \Gamma^\beta(\varepsilon_\beta)\left[\frac{1}{\omega+\varepsilon_\beta}+\frac{1}{\omega-\varepsilon_\beta}\right]. \tag{A.12}$$

After perform the change of variable in the first integral we can write

$$\Sigma_3(\omega) = \frac{1}{2\pi}\sum_{\beta}\int d\varepsilon_\beta \left[\frac{\Gamma^\beta(-\varepsilon_\beta)}{\omega-\varepsilon_\beta}+\frac{\Gamma^\beta(\varepsilon_\beta)}{\omega-\varepsilon_\beta}\right]. \tag{A.13}$$

Once again we make the assumption that the coupling strength is even with respect to the energy to obtain

$$\Sigma_3(\omega) = 2\left[\frac{1}{2\pi}\sum_{\beta}\int d\varepsilon_\beta \frac{\Gamma^\beta(\varepsilon_\beta)}{\omega-\varepsilon_\beta}\right], \tag{A.14}$$

or, more explicitly,

$$\Sigma_3(\omega) = 2\Sigma_0(\omega) \ . \tag{A.15}$$

A.3 EOM Green's function at the particle-hole symmetric point

In the particle-hole symmetric case $\varepsilon_0 = -U/2$, $\langle n_\sigma \rangle = 1/2$. Substituting the results of Eqs. (A.11) and (A.15) in Eq. (A.1) we have

$$\begin{aligned}
[G_\sigma(\omega)]^{-1} &= \frac{\omega^2 - \frac{\omega U}{2} - 3\omega\Sigma_0(\omega) + \frac{\omega U}{2} - \frac{U^2}{4} - \frac{3U\Sigma_0(\omega)}{2} - \omega\Sigma_0(\omega) + \frac{U\Sigma_0(\omega)}{2} + 3[\Sigma_0(\omega)]^2 + U\Sigma_0(\omega)}{\omega - 3\Sigma_0(\omega)} \\
&= \frac{\omega^2 - 3\omega\Sigma_0(\omega) - \omega\Sigma_0(\omega) - \frac{U^2}{4} + 3[\Sigma_0(\omega)]^2}{\omega - 3\Sigma_0(\omega)} \\
&= \frac{\omega[\omega - 3\Sigma_0(\omega)] - \Sigma_0(\omega)[\omega - 3\Sigma_0(\omega)] - \frac{U^2}{4}}{\omega - 3\Sigma_0(\omega)} \\
&= \frac{[\omega - \Sigma_0(\omega)][\omega - 3\Sigma_0(\omega)] - \frac{U^2}{4}}{\omega - 3\Sigma_0(\omega)} \ .
\end{aligned} \tag{A.16}$$

After a final rearrangement we have

$$[G_\sigma(\omega)]^{-1} = \omega - \Sigma_0(\omega) - \frac{U^2}{4[\omega - 3\Sigma_0(\omega)]} \ , \tag{A.17}$$

which coincides with the EOM2 Green's function, Eq. (2.49).

It is a straightforward exercise to show that the EOM0, Eq. (2.25), gives

$$[G_\sigma(\omega)]^{-1} = \omega - \Sigma_0(\omega) - \frac{U^2}{4\omega} \ , \tag{A.18}$$

at $\varepsilon_0 = -U/2$, and its explicit two-resonance approximation, Eq. (2.26), reads

$$[G_\sigma(\omega)]^{-1} = \omega - \Sigma_0(\omega) - \frac{U^2}{4[\omega - \Sigma_0(\omega)]} \ . \tag{A.19}$$

Let us analyze Eqs. (A.17), (A.18), and (A.19) in the wide band limit, in which the embedding self-energy is written as

$$\Sigma_0 = -i\frac{\Gamma}{2} \ . \tag{A.20}$$

In this analysis we focus on the weak coupling regime, $\Gamma \ll U$. Substituting Eq. (A.20)

in Eq. (A.17) we have

$$\begin{aligned}[G_\sigma(\omega)]^{-1} &= \omega + i\frac{\Gamma}{2} - \frac{U^2}{4\left[\omega + \frac{3\Gamma}{2}i\right]} \\ &= \omega + i\frac{\Gamma}{2} - \frac{U^2}{4\left[\omega + \frac{3\Gamma}{2}i\right]}\frac{\left[\omega - \frac{3\Gamma}{2}i\right]}{\left[\omega - \frac{3\Gamma}{2}i\right]} \\ &= \omega + i\frac{\Gamma}{2} - \frac{U^2}{4\left[\omega^2 + \frac{9\Gamma^2}{4}\right]}\left[\omega - \frac{3\Gamma}{2}i\right] \end{aligned} \tag{A.21}$$

Let us compute the Green's functions at the single particle resonance, namely, at $\omega = \varepsilon_0 = -U/2$. In this case we have

$$[G_\sigma(\omega)]^{-1} = -\frac{U}{2} + i\frac{\Gamma}{2} - \frac{U^2/4}{\left[\frac{U^2}{4} + \frac{9\Gamma^2}{4}\right]}\left[-\frac{U}{2} - \frac{3\Gamma}{2}i\right] . \tag{A.22}$$

Since $\Gamma \ll U$ we can write

$$[G_\sigma(\omega)]^{-1} = -\frac{U}{2} + i\frac{\Gamma}{2} - \frac{U^2/4}{U^2/4}\left[-\frac{U}{2} - \frac{3\Gamma}{2}i\right] . \tag{A.23}$$

A final algebraic manipulation leads to

$$[G_\sigma(\omega)]^{-1} = 2\Gamma i \ . \tag{A.24}$$

By using the above steps in Eq. (A.18) we obtain

$$[G_\sigma(\omega)]^{-1} = \frac{\Gamma}{2}i \ , \tag{A.25}$$

while for the Eq. (A.19) we obtain

$$[G_\sigma(\omega)]^{-1} = \Gamma i \ , \tag{A.26}$$

which puts in evidence a surprising discrepancy with respect to the exact EOM0 expression, regardless the values of T and Γ, provided $\Gamma \ll U$, as shown in Fig. 42.

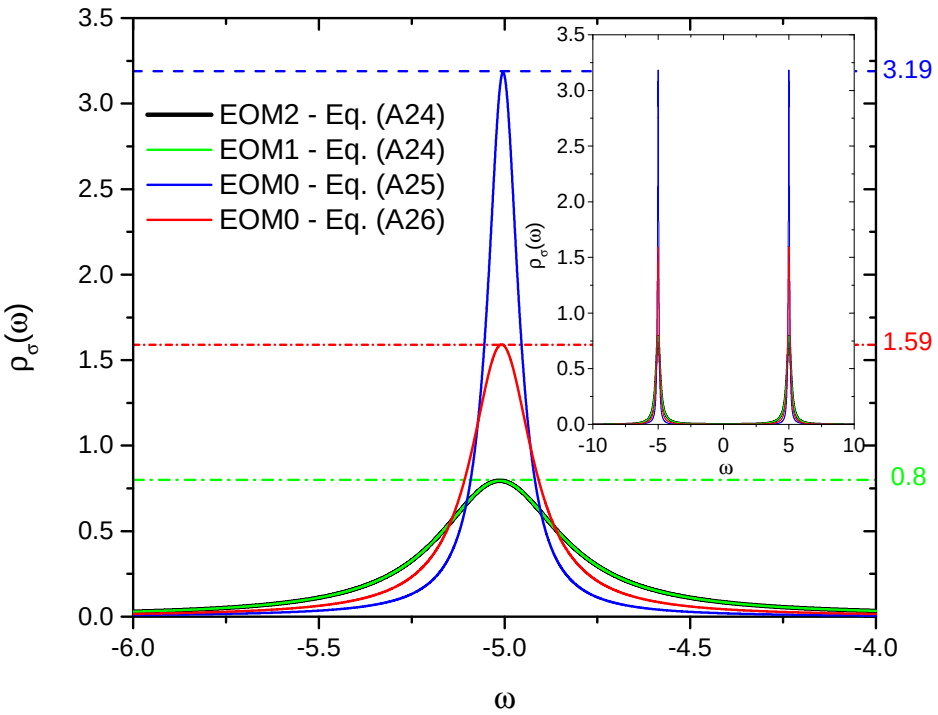

Figure 42: Density of states ρ_σ of the SIAM as a function of the energy ω for $U = 10$ (arbitrary units), $\Gamma = 0.02U$, $\varepsilon_0 = -U/2$, and $T = 0.1U$ obtained using the indicated EOM solvers. The main plot is a zoom near the region $\omega = \varepsilon_0$ and highlights the surprising discrepancy between the different approaches. The inset is a plot in a more extended energy region.

Appendix B – Kramers Kroning relations for non uniform frequency meshes

The NCA and OCA equations presented in the Chapter 2 were numerically implemented in such a way that the imaginary part of both the corresponding Green's functions and self-energies are calculated first and then their real part is obtained using the Kramers-Kronig relations. In order to numerically implement the Kramers-Kronig relations one can use Fourier transform methods [87]. However, in most cases the codes and methods found in the literature must be used with a frequency grid with equally spaced points. Since the pseudo-particle spectral functions often present extremely sharp peaks uniform frequency meshes do not give a good representation of the calculated objects, and a straightforward Fourier transform renders poor results.

In this appendix we present a method to numerically implement the Hilbert transform in a non-uniform frequency mesh. The method has been used in the Haule's implementation of the OCA method and was used by the author of this thesis to implement his own NCA code.

The Kramers-Kronig relation reads [141]

$$\mathrm{Re}[h(\omega)] = -\frac{1}{\pi}\mathcal{P}\int_{-\infty}^{\infty}\frac{\mathrm{Im}[h(\varepsilon)]}{\omega-\varepsilon}d\varepsilon\ , \tag{B.1}$$

where $h(\omega)$ is an arbitrary function and $\mathcal{P}$ stands for the Cauchy principal value. Here $h(\omega)$ stands eiher for Green's function or a self-energy. In order to handle the singular integrand we perform the following subtraction:

$$\mathrm{Re}[h(\omega)] = -\frac{1}{\pi}\mathcal{P}\int_{-\infty}^{\infty}\frac{\mathrm{Im}[h(\varepsilon)]-\mathrm{Im}[h(\omega)]}{\omega-\varepsilon}d\varepsilon - \frac{1}{\pi}\mathcal{P}\int_{-\infty}^{\infty}\frac{\mathrm{Im}[h(\omega)]}{\omega-\varepsilon}d\varepsilon\ . \tag{B.2}$$

In general, the frequency points are defined on a finite grid between a and b in such

a way that the imaginary part of $h(\omega)$ can be neglected at a or b. This allows us to write

$$\begin{aligned}\mathrm{Re}[h(\omega)] &= -\frac{1}{\pi}\mathcal{P}\int_a^b \frac{\mathrm{Im}[h(\varepsilon)]-\mathrm{Im}[h(\omega)]}{\omega-\varepsilon}d\varepsilon + \frac{\mathrm{Im}[h(\omega)]}{\pi}\left[\ln|\omega-b|-\ln|\omega-a|\right] \\ &= -\frac{1}{\pi}\mathcal{P}\int_a^b \frac{\mathrm{Im}[h(\varepsilon)]-\mathrm{Im}[h(\omega)]}{\omega-\varepsilon}d\varepsilon + \frac{\mathrm{Im}[h(\omega)]}{\pi}\ln\left(\frac{b-\omega}{\omega-a}\right). \end{aligned} \tag{B.3}$$

We evaluate the above integral using the trapezoid rule for numerical integrations. As standard, the integral on the r.h.s. of Eq. (B.3) is converted in a summation of trapezoid areas. This has to be done carefully since the integrand is indetermined for $\varepsilon = \omega$. In this case it is necessary to estimate the derivative $\frac{\mathrm{d}}{\mathrm{d}\omega}(\mathrm{Im}[h(\omega)])$. Let us supose that we have a grid of N frequency points ε_i ; $i = 1, \cdots, N$. Using the trapezoid rule one can write

$$\begin{aligned}\mathrm{Re}[h(\omega_i)] \approx -\frac{1}{\pi}\Bigg\{ &\sum_{j\neq i}^{N-1}\left[\frac{\mathrm{Im}[h(\varepsilon_{j+1})]-\mathrm{Im}[h(\omega_i)]}{\omega_i-\varepsilon_{j+1}} + \frac{\mathrm{Im}[h(\varepsilon_j)]-\mathrm{Im}[h(\omega_i)]}{\omega_i-\varepsilon_j}\right]\frac{(\varepsilon_{j+1}-\varepsilon_j)}{2} + \\ &+\frac{1}{2}\left[\frac{\mathrm{Im}[h(\varepsilon_{i+1})]-\mathrm{Im}[h(\varepsilon_i)]}{\varepsilon_{i+1}-\varepsilon_i} + \frac{\mathrm{Im}[h(\varepsilon_i)]-\mathrm{Im}[h(\varepsilon_{i-1})]}{\varepsilon_i-\varepsilon_{i-1}}\right]\frac{(\varepsilon_{i+1}-\varepsilon_i)}{2}\Bigg\} + \\ &+\frac{\mathrm{Im}[h(\omega_i)]}{\pi}\ln\left(\frac{b-\omega_i}{\omega_i-a}\right), \end{aligned} \tag{B.4}$$

in which it was used that

$$\frac{\mathrm{dIm}[h(\omega_i)]}{\mathrm{d}\omega} \approx \frac{1}{2}\left[\frac{\mathrm{Im}[h(\omega_{i+1})]-\mathrm{Im}[h(\omega_i)]}{\omega_{i+1}-\omega_i} + \frac{\mathrm{Im}[h(\omega_i)]-\mathrm{Im}[h(\omega_{i-1})]}{\omega_i-\omega_{i-1}}\right]. \tag{B.5}$$

References

[1] P. W. Anderson. Localized Magnetic States in Metals. *Physical Review*, 124(1):41–53, oct 1961.

[2] A.M. Tsvelick and P.B. Wiegmann. Exact results in the theory of magnetic alloys. *Advances in Physics*, 32(4):453–713, jan 1983.

[3] Leo Kouwenhoven and Leonid Glazman. Revival of the Kondo effect. *Physics World*, 14(1):33–38, 2001.

[4] J. P. Franck, F. D. Manchester, and D. L. Martin. The specific heat of pure copper and of some dilute copper + iron alloys showing a minimum in the electrical resistance at low temperatures. *Proceedings of the Royal Society of London. Series A. Mathematical and Physical Sciences*, 263(1315):494–507, oct 1961.

[5] Jun Kondo. Resistance Minimum in Dilute Magnetic Alloys. *Progress of Theoretical Physics*, 32(1):37–49, 1964.

[6] J. Friedel. Metallic alloys. *Il Nuovo Cimento*, 7(2 Supplement):287–311, 1958.

[7] Alexander Cyril Hewson. *The Kondo Problem to Heavy Fermions*. Cambridge University Press, 2nd edition, 1997.

[8] J. R. Schrieffer and P. A. Wolff. Relation between the Anderson and Kondo Hamiltonians. *Physical Review*, 149(2):491–492, sep 1966.

[9] S Sasaki, De Franceschi S, Jm Elzerman, van der Wiel WG, M Eto, S Tarucha, and Lp Kouwenhoven. Kondo effect in an integer-spin quantum dot. *Nature*, 405(6788):764–7, 2000.

[10] C. M. Varma. Mixed-valence compounds. *Reviews of Modern Physics*, 48(2):219–238, 1976.

[11] Piers Coleman. New approach to the mixed-valence problem. *Physical Review B*, 29(6):3035–3044, 1984.

[12] K. G. Wilson. Solution of the spin-1/2 Kondo Hamiltonian. In B. Lundqvist and S. Lundqvist, editors, *Proceedings of the 24 th Nobel Symposium*, pages 68–75, Uppsala, 1974. New York Academic Press.

[13] Kenneth G. Wilson. The renormalization group: Critical phenomena and the Kondo problem. *Reviews of Modern Physics*, 47(4):773–840, 1975.

[14] Kei Yosida and Kosaku Yamada. Perturbation Expansion for the Anderson Hamiltonian. *Progress of Theoretical Physics Supplement*, 46(46):244–255, 1970.

[15] Kei Yosida and Kosaku Yamada. Perturbation Expansion for the Anderson Hamiltonian. III. *Progress of Theoretical Physics*, 53(5):1286–1301, may 1975.

[16] Kosaku Yamada. Perturbation Expansion for the Anderson Hamiltonian. II. *Progress of Theoretical Physics*, 53(4):970–986, apr 1975.

[17] David Goldhaber-Gordon, Michael S. Montemerlo, J. Christopher Love, Gregory J. Opiteck, and James C. Ellenbogen. Overview of nanoelectronic devices. *Proceedings of the IEEE*, 85(4):521–540, 1997.

[18] Leo Kouwenhoven and Charles Marcus. Quantum dots. *Physics World*, 11(6):35–40, jun 1998.

[19] Wenjie Liang, Matthew P. Shores, Marc Bockrath, Jeffrey R. Long, and Hongkun Park. Kondo resonance in a single-molecule transistor. *Nature*, 417(6890):725–729, jun 2002.

[20] Jiwoong Park, Abhay N. Pasupathy, Jonas I. Goldsmith, Connie Chang, Yuval Yaish, Jason R. Petta, Marie Rinkoski, James P. Sethna, Héctor D. Abruña, Paul L. McEuen, and Daniel C. Ralph. Coulomb blockade and the Kondo effect in single-atom transistors. *Nature*, 417(6890):722–725, jun 2002.

[21] N. Andrei. Diagonalization of the Kondo Hamiltonian. *Physical Review Letters*, 45(5):379–382, aug 1980.

[22] P.B. Wiegmann. Exact solution of s-d exchange model at T = 0. *Journal of Experimental and Theoretical Physics*, 31(7):364, 1980.

[23] P B Wiegmann and A M Tsvelick. Exact solution of the Anderson model: I. *Journal of Physics C: Solid State Physics*, 16(12):2281–2319, apr 1983.

[24] E Ogievetski, A M Tsvelick, and P B Wiegmann. Exact solution of the degenerate Anderson model. *Journal of Physics C: Solid State Physics*, 16(22):L797–L802, aug 1983.

[25] Sebastian Schmitt, Torben Jabben, and Norbert Grewe. Dynamic susceptibilities of the single-impurity Anderson model within an enhanced noncrossing approximation. *Physical Review B - Condensed Matter and Materials Physics*, 80(23):1–14, 2009.

[26] K. Held. Electronic structure calculations using dynamical mean field theory. *Advances in Physics*, 56(6):829–926, 2007.

[27] N. F. Mott. Metal-insulator transition. *Reviews of Modern Physics*, 40(4):677–683, 1968.

[28] N. F. Mott. *Metal-Insulator Transitions*. Taylor & Francis, London, 1990.

[29] Florian Gebhard. *The Mott metal-insulator transition: models and methods*. Springer, 1997.

[30] A Georges, G Kotliar, W Krauth, and M Rozenberg. Dynamical mean-field theory of strongly correlated fermion systems and the limit of infinite dimensions. *Reviews of Modern Physics*, 68(1):13–125, 1996.

[31] Antoine Georges, Gabriel Kotliar, and Qimiao Si. Strongly Correlated Systems in Infinite Dimensions and Their Zero Dimensional Counterparts. *International Journal of Modern Physics B*, 06(05n06):705–730, mar 1992.

[32] Piers Coleman. 1/N expansion for the Kondo lattice. *Physical Review B*, 28(9):5255–5262, 1983.

[33] Elliott H. Lieb and F. Y. Wu. Absence of mott transition in an exact solution of the short-range, one-band model in one dimension. *Physical Review Letters*, 20(25):1445–1448, 1968.

[34] Klaus Capelle. A bird's-eye view of density-functional theory. *Brazilian Journal of Physics*, 36(4a):1318–1343, 2006.

[35] Richard M. Martin. *Electronic structure: basic theory and practical methods*. Cambridge University Press, 2004.

[36] G. Kotliar, S. Y. Savrasov, K. Haule, V. S. Oudovenko, O. Parcollet, and C. A. Marianetti. Electronic structure calculations with dynamical mean-field theory. *Reviews of Modern Physics*, 78(3):865–951, 2006.

[37] W. H. Brito, M. C.O. Aguiar, K. Haule, and G. Kotliar. Metal-Insulator Transition in VO_2: A DFT+DMFT Perspective. *Physical Review Letters*, 117(5):1–6, 2016.

[38] Norbert Grewe, Sebastian Schmitt, Torben Jabben, and Frithjof B. Anders. Conserving approximations in direct perturbation theory: new semianalytical impurity solvers and their application to general lattice problems. *Journal of Physics: Condensed Matter*, 20(36):365217, sep 2008.

[39] M. A. Kastner. The single-electron transistor. *Reviews of Modern Physics*, 64(3):849–858, 1992.

[40] M A Kastner, D. Goldhaber-Gordon, Hadas Shtrikman, D. Mahalu, David Abusch-Magder, and U. Meirav. Kondo effect in a single-electron transistor. *Nature*, 391(6663):156–159, jan 1998.

[41] I.L. Aleiner, P.W. Brouwer, and L.I. Glazman. Quantum effects in Coulomb blockade. *Physics Reports*, 358(5-6):309–440, mar 2002.

[42] P. L. McEuen, E. B. Foxman, U. Meirav, M. A. Kastner, Yigal Meir, Ned S. Wingreen, and S. J. Wind. Transport spectroscopy of a Coulomb island in the quantum Hall regime. *Physical Review Letters*, 66(14):1926–1929, 1991.

[43] E. B. Foxman, P. L. McEuen, U. Meirav, Ned S. Wingreen, Yigal Meir, Paul A. Belk, N. R. Belk, M. A. Kastner, and S. J. Wind. Effects of quantum levels on transport through a Coulomb island. *Physical Review B*, 47(15):10020–10023, 1993.

[44] C. W J Beenakker. Theory of Coulomb-blockade oscillations in the conductance of a quantum dot. *Physical Review B*, 44(4):1646–1656, 1991.

[45] S. Tarucha, K. Ono, T. Fujisawa, W.G. Van der Wiel, and L. P. Kouwenhoven. Interactions, Spins and the Kondo Effect in Quantum-Dot Systems. In Jonathan P. Bird, editor, *Electron Transport in Quantum Dots*, chapter 1. Springer Science+Business Media, LLC, New York, 2003.

[46] Yigal Meir, Ned S. Wingreen, and Patrick A. Lee. Transport through a strongly interacting electron system: Theory of periodic conductance oscillations. *Physical Review Letters*, 66(23):3048–3051, 1991.

[47] Michael Pustilnik and Leonid Glazman. Kondo effect in quantum dots. *Journal of Physics: Condensed Matter*, 16(16):R513–R537, 2004.

[48] S. M. Cronenwett. A Tunable Kondo Effect in Quantum Dots. *Science*, 281(5376):540–544, 1998.

[49] W. G. van der Wiel, S. De Franceschi, T. Fujisawa, J. M. Elzerman, S. Tarucha, and L. P. Kouwenhoven. The Kondo Effect in the Unitary Limit. *Science*, 289(5487):2105–2108, sep 2000.

[50] James R. Heath and Mark A. Ratner. Molecular Electronics. *Physics Today*, 56(5):43–49, may 2003.

[51] David Jacob. Towards a full ab initio theory of strong electronic correlations in nanoscale devices. *Journal of Physics: Condensed Matter*, 27(24):245606, 2015.

[52] Alexandre R Rocha, Víctor M. García-suárez, Steve W Bailey, Colin J Lambert, Jaime Ferrer, and Stefano Sanvito. Towards molecular spintronics. *Nature Materials*, 4(4):335–339, 2005.

[53] D Jacob, K Haule, and G Kotliar. Dynamical mean-field theory for molecular electronics: Electronic structure and transport properties. *Physical Review B*, 82(19):195115, 2010.

[54] Juan Jose Palacios, E Louis, A J Perez-Jimenez, E San Fabian, and J A Verges. An ab initio approach to electrical transport in molecular devices. *Nanotechnology*, 13(3):378–381, 2002.

[55] Supriyo Datta. *Electronic Transport in Mesoscopic Systems*. Cambridge University Press, 1997.

[56] A. R. Rocha, V. M. García-Suárez, S. Bailey, C. Lambert, J. Ferrer, and S. Sanvito. Spin and molecular electronics in atomically generated orbital landscapes. *Physical Review B - Condensed Matter and Materials Physics*, 73(8), 2006.

[57] Mads Brandbyge, José-Luis Mozos, Pablo Ordejón, Jeremy Taylor, and Kurt Stokbro. Density-functional method for nonequilibrium electron transport. *Physical Review B*, 65(16):165401, 2002.

[58] D. Jacob, K. Haule, and G. Kotliar. Kondo Effect and Conductance of Nanocontacts with Magnetic Impurities. *Physical Review Letters*, 103(1):3–6, 2009.

[59] Vyacheslavs Kashcheyevs, Amnon Aharony, and Ora Entin-Wohlman. Applicability of the equations-of-motion technique for quantum dots. *Physical Review B - Condensed Matter and Materials Physics*, 73(12):1–15, 2006.

[60] N. E. Bickers. Review of techniques in the large-N expansion for dilute magnetic alloys. *Reviews of Modern Physics*, 59(4):845–939, 1987.

[61] C. N. Sposetti, L. O. Manuel, and P. Roura-Bas. Qualitative breakdown of the noncrossing approximation for the symmetric one-channel Anderson impurity model at all temperatures. *Physical Review B - Condensed Matter and Materials Physics*, 94(8):1–8, 2016.

[62] Leandro Tosi, Pablo Roura-Bas, Ana María Llois, and Luis O. Manuel. Effects of vertex corrections on diagrammatic approximations applied to the study of transport through a quantum dot. *Physical Review B*, 83(7):073301, 2011.

[63] Luis G. G. V. Dias da Silva, Caio H. Lewenkopf, Edson Vernek, Gerson J. Ferreira, and Sergio E. Ulloa. Conductance and Kondo Interference beyond Proportional Coupling. *Physical Review Letters*, 119(11):116801, sep 2017.

[64] Yigal Meir and Ned S. Wingreen. Landauer formula for the current through an interacting electron region. *Physical Review Letters*, 68(16):2512–2515, 1992.

[65] Ned S. Wingreen and Yigal Meir. Anderson model out of equilibrium: Noncrossing-approximation approach to transport through a quantum dot. *Physical Review B*, 49(16):11040–11052, 1994.

[66] Henrik Bruus and Flensberg Karsten. *Many-body quantum theory in condensed matter physics: an introduction*. Oxford University Press, 2003.

[67] Hartmut Haug and Antti-Pekka Jauho. *Quantum Kinectics in Transport and Optics of Semiconductors*. Springer, 2nd edition, 2008.

[68] Gianluca Stefanucci and Robert Van Leeuwen. *Nonequilibrium many-body theory of quantum systems: a modern introduction*. Cambridge University Press, 2013.

[69] J. Hubbard. Electron Correlations in Narrow Energy Bands. *Proceedings of the Royal Society A: Mathematical, Physical and Engineering Sciences*, 276(1365):238–257, 1963.

[70] J. Hubbard. Electron correlations in narrow energy bands III. An improved solution. *Proceedings of the Royal Society of London. Series A. Mathematical and Physical Sciences*, 281(1386):401–419, sep 1964.

[71] M. Cyrot. The Hubbard hamiltonian. *Physica B*, 91(C):141–150, 1977.

[72] D. N. Zubarev. Double-time Green functions in statistical physics. *Soviet Physics Uspekhi*, 3(3):320–345, mar 1960.

[73] C Lacroix. Density of states for the Anderson model. *Journal of Physics F: Metal Physics*, 11(11):2389–2397, nov 1981.

[74] C. Lacroix. Density of states for the asymmetric Anderson model. *Journal of Applied Physics*, 53(3):2131–2133, 1982.

[75] D.M. Newns and N Read. Mean-field theory of intermediate valence/heavy fermion systems. *Advances in Physics*, 36(6):799–849, jan 1987.

[76] Piers Coleman. Mixed valence as an almost broken symmetry. *Physical Review B*, 35(10):5072–5116, 1987.

[77] N. Read and D. M. Newns. On the solution of the Coqblin-Schreiffer Hamiltonian by the large-N expansion technique. *Journal of Physics C: Solid State Physics*, 16(17):3273–3295, 1983.

[78] Assa Auerbach and K. Levin. Kondo bosons and the Kondo lattice: Microscopic basis for the heavy fermi liquid. *Physical Review Letters*, 57(7):877–880, 1986.

[79] A. J. Millis and P. A. Lee. Large-orbital-degeneracy expansion for the lattice Anderson model. *Physical Review B*, 35(7):3394–3414, 1987.

[80] M. Grilli, B. G. Kotliar, and A. J. Millis. Mean-field theories of cuprate superconductors: A systematic analysis. *Physical Review B*, 42(1):329–341, jul 1990.

[81] M. Grilli, R. Raimondi, C. Castellani, C. Di Castro, and G. Kotliar. Superconductivity, phase separation, and charge-transfer instability in the $U = \infty$ limit of the three-band model of the CuO 2 planes. *Physical Review Letters*, 67(2):259–262, jul 1991.

[82] S E Barnes. New method for the Anderson model. *Journal of Physics F*, 6(7):1375–1383, 1976.

[83] S E Barnes. New method for the Anderson model. II. The U=0 limit. *Journal of Physics F: Metal Physics*, 7(12):2637–2647, dec 1977.

[84] Gabriel Kotliar and Andrei E. Ruckenstein. New functional integral approach to strongly correlated fermi systems: The gutzwiller approximation as a saddle point. *Physical Review Letters*, 57(11):1362–1365, 1986.

[85] Ramón Aguado and David C. Langreth. Kondo effect in coupled quantum dots: A noncrossing approximation study. *Physical Review B - Condensed Matter and Materials Physics*, 67(24), 2003.

[86] K Haule, S Kirchner, J Kroha, and P. Wölfle. Anderson impurity model at finite Coulomb interaction U : Generalized noncrossing approximation. *Physical Review B*, 64(15):155111, sep 2001.

[87] Kristjan Haule, Chuck Hou Yee, and Kyoo Kim. Dynamical mean-field theory within the full-potential methods: Electronic structure of $CeIrIn_5$, $CeCoIn_5$, and $CeRhIn_5$. *Physical Review B - Condensed Matter and Materials Physics*, 81(19):195107, may 2010.

[88] Gerald D. Mahan. *Many-Particle Physics*. Plenum Pr., New York, 1990.

[89] A Abrikosov. Electron scattering on magnetic impurities in metals and anomalous resistivity effects. *Physics. Physique. Fizika*, 2(1):5–20, 1965.

[90] Johann Kroha and Peter Wölfle. Fermi and non-fermi liquid behavior in quantum impurity systems: conserving slave boson theory. *Acta Physica Polonica B*, 29(12):3781–3817, 1998.

[91] T. Costi, J. Kroha, and P. Wölfle. Spectral properties of the Anderson impurity model: Comparison of numerical-renormalization-group and noncrossing-approximation results. *Physical Review B*, 53(4):1850–1865, 1996.

[92] Matthias H Hettler, Johann Kroha, and Selman Hershfield. Nonequilibrium dynamics of the Anderson impurity model. *Phys. Rev. B*, 58(9):5649–5664, 1998.

[93] Th Pruschke and N. Grewe. The Anderson model with finite Coulomb repulsion. *Zeitschrift für Physik B Condensed Matter*, 74(4):439–449, 1989.

[94] Ralf Bulla, Theo A. Costi, and Thomas Pruschke. Numerical renormalization group method for quantum impurity systems. *Reviews of Modern Physics*, 80(2):395–450, 2008.

[95] Robert Peters, Thomas Pruschke, and Frithjof B. Anders. Numerical renormalization group approach to Green's functions for quantum impurity models. *Physical Review B - Condensed Matter and Materials Physics*, 74(24):1–12, 2006.

[96] Andreas Weichselbaum and Jan Von Delft. Sum-rule conserving spectral functions from the numerical renormalization group. *Physical Review Letters*, 99(7):1–4, 2007.

[97] David C. Langreth. Friedel Sum Rule for Anderson's Model of Localized Impurity States. *Physical Review*, 150(2):516–518, oct 1966.

[98] V Vildosola, L V Pourovskii, L O Manuel, and P Roura-Bas. Reliability of the one-crossing approximation in describing the Mott transition. *Journal of Physics Condensed Matter*, 27(48):485602, dec 2015.

[99] P. Roura-Bas. Universal scaling in transport out of equilibrium through a single quantum dot using the noncrossing approximation. *Physical Review B - Condensed Matter and Materials Physics*, 81(15):1–6, 2010.

[100] Yigal Meir, Ned S. Wingreen, and Patrick a. Lee. Low-temperature transport through a quantum dot: The Anderson model out of equilibrium. *Physical Review Letters*, 70(17):2601–2604, apr 1993.

[101] Alba Theumann. Self-Consistent Solution of the Anderson Model. *Physical Review*, 178(3):978–984, feb 1969.

[102] Joel A. Appelbaum and David R. Penn. Localized Correlations in Narrow Conduction Bands. I. *Physical Review*, 188(2):874–887, dec 1969.

[103] Joel A. Appelbaum and David R. Penn. Localized Correlations in Narrow Conduction Bands. II. *Physical Review B*, 3(3):942–953, feb 1971.

[104] Lowell Dworin. Anderson model of localized magnetic moments. I. High-temperature behavior. *Physical Review*, 164(2):818–840, 1967.

[105] Lowell Dworin. Anderson Model of Localized Magnetic Moments. II. "Derivation" of the Integral Equation. *Physical Review*, 164(2):841–856, dec 1967.

[106] Akihide Oguchi. Green's Function Theory for the Anderson Model. *Progress of Theoretical Physics*, 43(2):257–270, feb 1970.

[107] G Kotliar and D Vollhardt. Strongly Correlated Materials: Insights From Dynamical Mean-Field Theory. *Physics Today*, 57(3):53, 2004.

[108] M. Jarrell and Thomas Pruschke. Magnetic and dynamic properties of the Hubbard model in infinite dimensions. *Zeitschrift für Physik B Condensed Matter*, 90(2):187–194, 1993.

[109] Walter Metzner and Dieter Vollhardt. Correlated lattice fermions in d= dimensions. *Physical Review Letters*, 62(3):324–327, 1989.

[110] E. Müller-Hartmann. Correlated fermions on a lattice in high dimensions. *Zeitschrift für Physik B Condensed Matter*, 74(4):507–512, 1989.

[111] E. Müller-Hartmann. Fermions on a lattice in high dimensions. *International Journal of Modern Physics B*, 03(12):2169–2187, dec 1989.

[112] E. Müller-Hartmann. The Hubbard model at high dimensions: some exact results and weak coupling theory. *Zeitschrift für Physik B Condensed Matter*, 76(2):211–217, jun 1989.

[113] U. Brandt and C. Mielsch. Thermodynamics and correlation functions of the Falicov-Kimball model in large dimensions. *Zeitschrift für Physik B Condensed Matter*, 75(3):365–370, sep 1989.

[114] U. Brandt and C. Mielsch. Thermodynamics of the Falicov-Kimball model in large dimensions II - Critical temperature and order parameter. *Zeitschrift für Physik B Condensed Matter*, 79(2):295–299, 1990.

[115] U. Brandt and C. Mielsch. Free energy of the Falicov-Kimball model in large dimensions. *Zeitschrift für Physik B Condensed Matter*, 82(1):37–41, 1991.

[116] Nobuo Furukawa. Transport Properties of the Kondo Lattice Model in the Limit S $= \infty$ and D $= \infty$. *Journal of the Physical Society of Japan*, 63(9):3214–3217, sep 1994.

[117] Antoine Georges and Gabriel Kotliar. Hubbard model in infinite dimensions. *Physical Review B*, 45(12):6479–6483, 1992.

[118] J. W. Negele and H. Orland. *Quantum Many-Particle Systems*. Perseus Book, 1998.

[119] Antoine Georges and Werner Krauth. Physical properties of the half-filled Hubbard model in infinite dimensions. *Physical Review B*, 48(10):7167–7182, 1993.

[120] H. Krishna-murthy, J. Wilkins, and K. Wilson. Renormalization-group approach to the Anderson model of dilute magnetic alloys. I. Static properties for the symmetric case. *Physical Review B*, 21(3):1003–1043, feb 1980.

[121] H. R. Krishna-Murthy, J. W. Wilkins, and K. G. Wilson. Renormalization-group approach to the Anderson model of dilute magnetic alloys. II. Static properties for the asymmetric case. *Physical Review B*, 21(3):1044–1083, 1980.

[122] J. E. Hirsch and R. M. Fye. Monte Carlo Method for Magnetic Impurities in Metals. *Physical Review Letters*, 56(23):2521–2524, 1986.

[123] B. A. Amadon. A self-consistent DFT+DMFT scheme in the projector augmented wave method: Applications to cerium, $Ce_2O_3$and Pu_2O_3 with the Hubbard I solver and comparison to DFT+U. *Journal of Physics Condensed Matter*, 24(7), 2012.

[124] Eleftherios N. Economou. *Green's Functions in Quantum Physics*. Springer, 3rd edition, 2006.

[125] M. C.O. Aguiar. *Efeitos de temperatura e de interação finita em sistemas desordenados correlacionados*. PhD thesis, Universidade Estadual de Campinas, 2003.

[126] G. P. M. Poppe and C. M. J. Wijers. Algorithm 680: evaluation of the complex error function. *ACM Transactions on Mathematical Software*, 16(1):47, 1990.

[127] Thomas Maier, Mark Jarrell, Thomas Pruschke, and Matthias H Hettler. Quantum cluster theories. *Reviews of Modern Physics*, 77(3):1027–1080, oct 2005.

[128] M. Hettler, A. Tahvildar-Zadeh, M. Jarrell, and T. Pruschke. Nonlocal dynamical correlations of strongly interacting electron systems. *Physical Review B - Condensed Matter and Materials Physics*, 58(12):R7475–R7479, 1998.

[129] Andreas Rüegg, Emanuel Gull, Gregory A. Fiete, and Andrew J. Millis. Sum rule violation in self-consistent hybridization expansions. *Physical Review B - Condensed Matter and Materials Physics*, 87(7):1–11, 2013.

[130] V. Vildosola, A. M. Llois, and M. Alouani. Spectral properties and crystal-field splittings in CeM_2Si$_2$ (M=Ru, Rh, or Pd) compounds. *Physical Review B - Condensed Matter and Materials Physics*, 71(18):1–8, 2005.

[131] P. Roura-Bas, V. Vildosola, and A. M. Llois. Evolution of the crystal-field splittings in the compounds CeX (X = P, As, Sb, Bi) and CeY (Y = S , Se, Te) and their alloys Ce$X_{1-x}Y_x$. *Physical Review B*, 75(19):195129, 2007.

[132] Th. Pruschke, D. L. Cox, and M Jarrell. Hubbard model at infinite dimensions: Thermodynamic and transport properties. *Physical Review B*, 47(7):3553–3565, feb 1993.

[133] Andreas Rüegg, Hsiang Hsuan Hung, Emanuel Gull, and Gregory A. Fiete. Comparative DMFT study of the e g -orbital Hubbard model in thin films. *Physical Review B - Condensed Matter and Materials Physics*, 89(8):1–11, 2014.

[134] Quan Yin, Andrey Kutepov, Kristjan Haule, Gabriel Kotliar, Sergey Y. Savrasov, and Warren E. Pickett. Electronic correlation and transport properties of nuclear fuel materials. *Physical Review B - Condensed Matter and Materials Physics*, 84(19):1–7, 2011.

[135] N. Grewe, T. Jabben, and S. Schmitt. Multi-orbital Anderson models and the Kondo effect: A NCA study enhanced by vertex corrections. *European Physical Journal B*, 68(1):23–32, 2009.

[136] J. H. Shim, K. Haule, and G. Kotliar. Fluctuating valence in a correlated solid and the anomalous properties of d-plutonium. *Nature*, 446(7135):513–516, 2007.

[137] J. H. Shim, K. Haule, and G. Kotliar. Modeling the localized-to-itinerant electronic transition in the heavy fermion system CeIrIn$_5$. *Science*, 318(5856):1615–1617, 2007.

[138] V. S. Oudovenko, G. Pálsson, K. Haule, G. Kotliar, and S. Y. Savrasov. Electronic structure calculations of strongly correlated electron systems by the dynamical mean-field method. *Physical Review B - Condensed Matter and Materials Physics*, 73(3):1–21, 2006.

[139] A. Lichtenstein and M. Katsnelson. Ab initio calculations of quasiparticle band structure in correlated systems: LDA++ approach. *Physical Review B - Condensed Matter and Materials Physics*, 57(12):6884–6895, 1998.

[140] A. Svane, V. Kanchana, G. Vaitheeswaran, G. Santi, W. M. Temmerman, Z. Szotek, P. Strange, and L. Petit. Electronic structure of samarium monopnictides and monochalcogenides. *Physical Review B - Condensed Matter and Materials Physics*, 71(4):1–10, 2005.

[141] George B. Arfken and Hans J. Weber. *Mathematical Methods for Physicists*. Elsevier Academic Press, 6th edition, 2005.